A Thesis of Nordic Master in Cold Climate Engineering

Joint Electrical and Acoustic Measurements for Unfrozen Water Content in Frozen Soil

Fan Jia

Trondheim, June 2019

MASTER THESIS: TBA4900

Main Supervisors: Gustav Grimstad, NTNU

Thomas Ingeman-Nielsen, DTU

Co-Supervisors: Chuangxin Lyu, NTNU

Department of Civil and Transport Engineering

Norwegian University of Science and Technology (NTNU)

Department of Civil Engineering

Technical University of Denmark (DTU)

Cold Climate Engineering

A! DTU NTNU

Preface

The work presented here is a part of my joint master degree in Cold Climate Engineering, carried out at the Geotechnical Division of Norwegian University of Science and Technology (NTNU) in the spring semester of 2019. The thesis is worth 30 ECTS, and it is conducted in collaboration with the Technical University of Denmark (DTU). The main supervisor at NTNU was Prof. Gustav Grimstad, with co-supervision of PhD candidate Chuangxin Lyu. DTU supervisor was Prof. Thomas Ingeman-Nielsen at the Department of Civil and Environmental Engineering. The idea of studying the measurement of unfrozen water content was born during the writing of the literature review about frozen soil, which is for the 15 ETCS course *TBA4510 Specialization Project on Frozen Soil* at the autumn semester of 2018. The idea of building a joint measurement system was born during a constructive discussion with PhD candidate Chuangxin Lyu at the beginning of the spring semester of 2019. All the laboratory works have been done in the *Ice Lab* at NTNU, with the great help from Senior Engineer Per Asbjørn Østensen with the Civil Department of NTNU.

Trondheim, 2019-6-21

Fan Jia

Acknowledgment

I would like to thank the following persons for their great help during my master education.

First, I would like to thank my parents and friends for all their love, support and encouragement.

My sincere gratitude to my supervisors Thomas Ingeman-Nielsen, Gustav Grimstad and Chuangxin Lyu for all their advice, support and guidance throughout the writing of this thesis.

I would especially like to thank Per Asbjørn Østensen for all his help in the laboratory. Thanks for the critical electronic components he made, the troubleshooting ideas he provided and the *LabVIEW* coding skills he taught. Without his help, none of the laboratory measurements would have been possible.

F. J.

Summary and Conclusions

The content of unfrozen water determines the mechanical, thermal and hydraulic properties of the frozen ground. This thesis suggests using a joint electrical and acoustic measurement method with a corresponding joint model to estimate the unfrozen water saturation accurately and efficiently. To develop a joint model, a larger joint measurement database should be built up first. Therefore, we developed a joint measurement system which can collect and process the electrical and acoustic data simultaneously, including developing the test apparatus and the *LabVIEW* program. The system has been calibrated by adjusting the test apparatus and optimising data processing. The measurements of dummy samples have been proved to be consistent with previous researches and a purchased precision instrument. With this joint system, we collected a good set of experimental data of the electrical resistivity and the p-wave velocity of two sets of *Halden Silt* samples with different salinity at different temperatures. The measurements have been verified to match the experimental results from previous credible publications and locate within the Hashin-Shtrikman bounds. In the end, by verifying of the inconsistency of unfrozen water saturation estimated by two single electrical and acoustic models, we revealed the motivation of developing a joint electrical and acoustic method for estimating the unfrozen water content more accurately. The joint model is suggested to use the same geometric assumption which controlled by one geometric coefficient. Then, with the joint measurement data, the geometric coefficient and the unfrozen water saturation can be solved simultaneously.

Contents

Chapter 1

Introduction

In this chapter, the background knowledge of frozen soil will be briefly introduced. Besides, the objectives and limitations of this thesis will be mentioned. The structure will also be presented at the end of this chapter to give an overview of this thesis to the readers.

1.1 Background

Frozen ground is the soil and rock with a temperature below $0°C$ (Andersland and Ladanyi, 2004). According to this definition, the definition of frozen soil is the soil with a temperature below $0°C$.

Perennially frozen soil, also known as permafrost, is the soil or rock having a temperature below 0°C during at least two consecutive winters and the intervening summer (Black, 1975). Therefore, permafrost is normally found in the polar regions (e.g. northern Canada, Greenland, Siberia and the Antarctic) and high altitude area (e.g. Qinghai-Tibet Plateau, Khangai-Altai Mountains). Seasonally frozen soil is more widely distributed on our planet. In the winter, the temperature of lots of areas in the world can reach below the freezing point, which allows the formation of frozen soil.

Unfrozen soil has three constituents: air, water and soil. In terms of frozen soil, it is a four-phase system with ice as the additional fourth constituent. Due to the existence of ice, the behaviours of frozen soil are different and more complicated than unfrozen soil. The appearance and dis-

appearance of ice (i.e. freezing and thawing of frozen soil) cause the volume change and water redistribution in the soil, which leads to various geohazards. Frost heave and thaw settlement are the most common geohazards happen in the frozen soil, and they endanger the people who live on it and the infrastructures which are built on it.

Frozen geomaterials are essentially multiphase materials, where water-ice phase transition is a gradual process due to capillarity, osmosis, and adsorption (Watanabe and Mizoguchi, 2002). In contrary, the ice content (or unfrozen water content) significantly influences some of the hydraulic, mechanical and thermal properties of the frozen soil. Figure 1.1 shows how these three properties interact with each other. By coupling the thermo-hydro-mechanical processes, the freezing and thawing process of frozen soil can be explained and modelled. For example, Figure 1.2 shows that the ice lens forms when the pore pressure is higher than the overburden load plus a certain segregation pressure. Meanwhile, the formation of an ice lens needs the supplement of the water from a deeper unfrozen soil layer; and the transportation of water relies on the force of cryogenic suction. Additionally, according to the Clapeyron equation, the cryogenic suction is related to the temperature gradient. Since the phase change of water changes the volume, thermal conduction, hydraulic conduction, etc., unfrozen water content is the essential factor of understanding and solving the frozen soil problems.

For measuring the unfrozen water content, various methods have been applied by many researchers in the previous studies. Dilatometry (Pusch, 1979) and calorimetry (Kolaian and Low, 1963; Anderson and Tice, 1971) methods were used initially to determined the unfrozen water content. The principles of the dilatometry and calorimetry methods are based on the volumetric and heat change during the phase change of water (ice), respectively. Thus, to measure the unfrozen water content (ice content), the frozen soil sample needs to be entirely melted to measure the changes. X-ray (Anderson and Hoekstra, 1965) and NMR (Nuclear Magnetic Resonance, Tice et al., 1982) methods were also used in the measurement of unfrozen water content. However, these two methods require laboratory testing environments and expensive equipment.

The methods mentioned above can be classified as the "direct" methods because the unfrozen

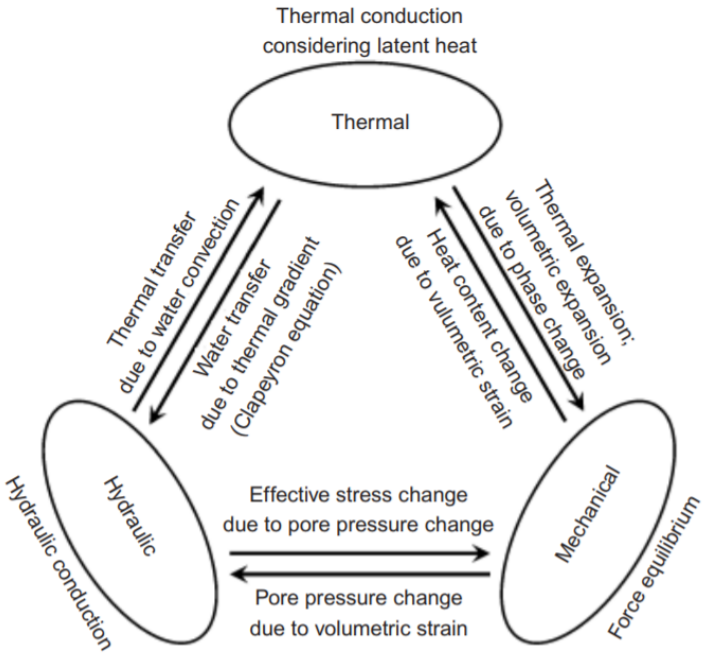

Figure 1.1: Thermo-hydro-mechanical interaction mechanism in freezing soils. (Thomas et al., 2009)

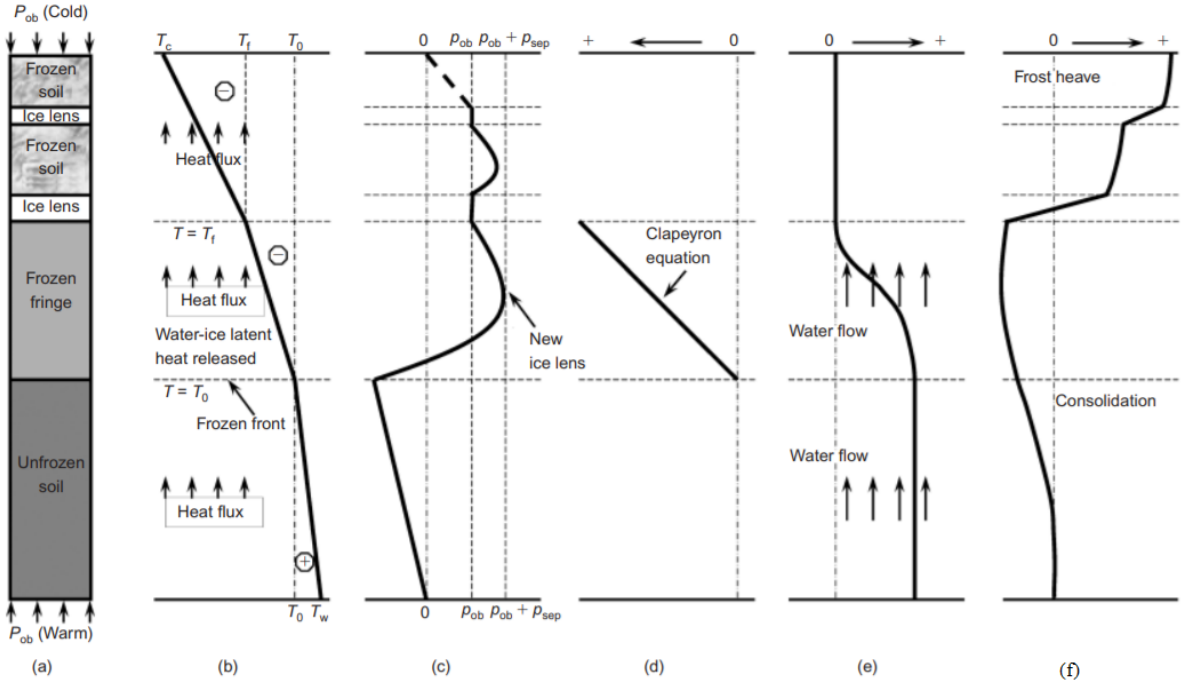

Figure 1.2: Schematic representation of a freezing soil with ice segregation: (a) layers; (b) temperature; (c) pore pressure; (d) cryogenic suction; (e) water velocity; (f) displacement (T_c,T_w, temperature at cold and warm ends, respectively; T_f, temperature at the base of ice lens; T_0, freezing point; p_{ob}, surface overburden load; p_{sep}, separation strength). (Thomas et al., 2009)

water content is determined by directly measuring the corresponding volumetric and thermal properties. There are also some "indirect" methods, which solves the problem by substituting the "indirect measurements" into some hypothetical models. Due to the measurement of these indirect parameters (e.g. electrical conductivity and acoustic velocity) are relatively easier to be measured, these "indirect" methods are cheaper and easier to be conducted comparing to the "direct" methods. However, the accuracy of these methods is lower than the "direct method" and are strongly dependent on the rationality of the chosen models.

For "indirect" measurement methods, the previous researches proposed various models which only contain one variable, S_w, unfrozen water saturation, which is the ratio of the unfrozen water volume and the total water volume. For the electrical resistivity measurement method, Daniels et al. (1976) and King et al. (1988) suggested using *Archie's law* to estimate the unfrozen water content in frozen soil. For the acoustic velocity method, *Weighted equation* (WE) method and *Kuster-Toksoz equations* method have been used by King et al. (1988), Lee et al. (1996). However, Lyu et al. (2019) reported the inconsistency of the estimated unfrozen water content by using single electrical and acoustic models, and the maximum difference is up to 20%. Therefore, the writers concluded that the reason is that unfrozen water content is not the only factor that influences the results of electrical resistivity and acoustic velocity.

Because of the inconsistency found in using the single measurement models, Lyu et al. (2019) suggested a joint method combining the electrical EMT (effective medium theory) and acoustic SCA (self-consistent approximation) model which all involve the same geometrical parameter: aspect ratio. Thus, based on sufficient joint acoustic and electrical measurements, the aspect ratio, α, and water saturation, S_w, can be solved simultaneously. The writers also reported that the estimations of S_w by the joint SCA-EMT method are most likely between the estimates from Archie's law and the WE model by using the joint measurements data of sandstone from Pandit and King (1979). Therefore, the joint electrical and acoustic method can be considered as a promising method to more accurately estimate the unfrozen water content in frozen soil. Furthermore, to develop more rational joint models, a large database of test results should be built up, which requires a large number of electrical and acoustic measurements on the same geomaterial at the same condition.

1.2 Objectives

Since the unfrozen water content plays an essential role for understanding the frozen soil behaviours, a good method to obtain the unfrozen water content accurately and efficiently is highly demanded. To develop a new joint method, the feasibility needs to be discussed and then a large joint measurement database is required to be built up. Therefore, the objectives of this thesis are

1. Build up a test system for joint electrical and acoustic measurement on frozen soil.
2. Conduct laboratory test to provide more joint electrical and acoustic measurement data of frozen silt sample with different salinity.
3. Verify the inconsistency of the unfrozen water content estimated by electrical and acoustic models found by Lyu et al. (2019) and reveal the potential of the joint method for improving the estimation of the unfrozen water content in frozen soil.

1.3 Limitations

The test system was built up by using the materials we can find in the laboratory, except that the piezo pads were purchased. Due to the defective test procedures, some of the parameters had to be calculated with some reasonable assumptions, instead of being measured from the test directly. Furthermore, this thesis only reveals the potential of a joint method. To develop a new joint method, it requires a deeper understanding of numerical modelling, which exceed the capability of the current writer.

1.4 Approach

The test setup was designed based on the literature review of previous experiments on soil. The testing system was calibrated by measuring materials with known properties and comparing with the result from reliable precise instrument. *LabVIEW* was used to control the testing system and process the recorded data. The calculations regarding to bounds and models were done in *MATLAB*. The joint measurements by our self-made system were verified by comparing with the results of similar soil from previous credible publications.

1.5 Structure of the Report

The rest of the report is structured as follows.

Chapter 1: **Introduction**

The first chapter introduces the background information about the importance of unfrozen water content for understanding the behaviours of frozen soil and proposes that the joint electrical and acoustic method is a promising method to obtain the estimated unfrozen water content accurately and efficiently. Also, the objectives, limitations and approach of this thesis are presented here.

Chapter 2: **Unfrozen Water Content in Frozen Soil**

In this chapter, the premelting theory is used to explain the existence of unfrozen water content below the freezing point. Besides, the freezing process of soil and the freezing point depression by salinity are briefly introduced.

Chapter 3: **Measuring Principles**

The basic concepts and terminologies of electrics and acoustics are introduced. This chapter describes the movement of electrical charges and the transmission of acoustic waves with schematics.

Chapter 4: **Laboratory Tests**

The soil analysis of *Halden Silt* and the preparation of the remoulded samples are presented here. This chapter also contains the schematics and photos of the setup. Besides, the dimensions, materials and settings of this setup are thoroughly discussed. Furthermore, the calibration methods and results are presented.

Chapter 5: **Test Results and Discussions**

This chapter presents the results from both electrical and acoustic measurements. Also, the feasibility and the potential of using a joint method to predict the unfrozen water saturation are presented here.

Chapter 6: **Conclusions and Suggested Further Works**

The final chapter consists of the final reflections and discussions about the obtained results. It also briefly summarises the research contribution of this study, outlining recommendation for future works.

Chapter 2

Unfrozen Water Content in Frozen Soil

The ice content is the most critical constituent which differs frozen soil from unfrozen soil. The temperature where the ice starts freezing is called the freezing point. Normally the ice is considered starting freezing when the temperature is under 0°C. However, the freezing point is not a fixed temperature; it can be affected by the microstructure, pressure, and salinity of the soil (Fofonoff and Millard Jr, 1983). Unfrozen water can also exist when the temperature is below the freezing point, Wettlaufer and Worster (2006) explained this phenomenon with the "premelting theory" which will be introduced in this chapter.

The only type of ice presents in soil pores is the ice of type I_h, the rheological behaviour of this kind of ice is so small that brittle failure begins right after elastic deformation (Tsytovich, 1960). Therefore, the elasticity of ice almost does not exist. Since ice has very different properties than water, frozen soil also has different properties than unfrozen soil, i.e. mechanical properties, hydraulic properties and thermal properties.

Assuming the total water content is fixed, once the unfrozen water content is known, the ice content can be calculated. Therefore, finding an efficient way to measure the unfrozen water content is important for the researches of the ice formation in frozen soil.

2.1 Freezing Point and Freezing Process

It is commonly believed that water will start freezing and becomes ice at 0°C. However, according to the research shown in Figure 2.1, the water will go through a stage called "super-cooled".

At this "super-cooled" stage, the water is in a metastable equilibrium state until nucleation centres trigger an abrupt transformation of free water to ice. The nuclei can be either aggregation of water molecules or soil particles. When the crystallization of ice starts, the latent heat will be released from free water, and the temperature will rise to T_f. T_f is the freezing point, and T_{sc} is the turning point where the released latent heat surpasses the heat loss due to the environmental temperature. T_f can be either higher or lower than 0°C.

After the "super-cooled" stage, the free water continues to freeze and release latent heat at the same time, so this process is slow, and the temperature does not drop. When free water is completely frozen, the bound water (the extremely thin layer of water surrounding mineral surfaces) starts freezing. Since the bound water does not contain much latent heat as the free water does, the freezing process continues.

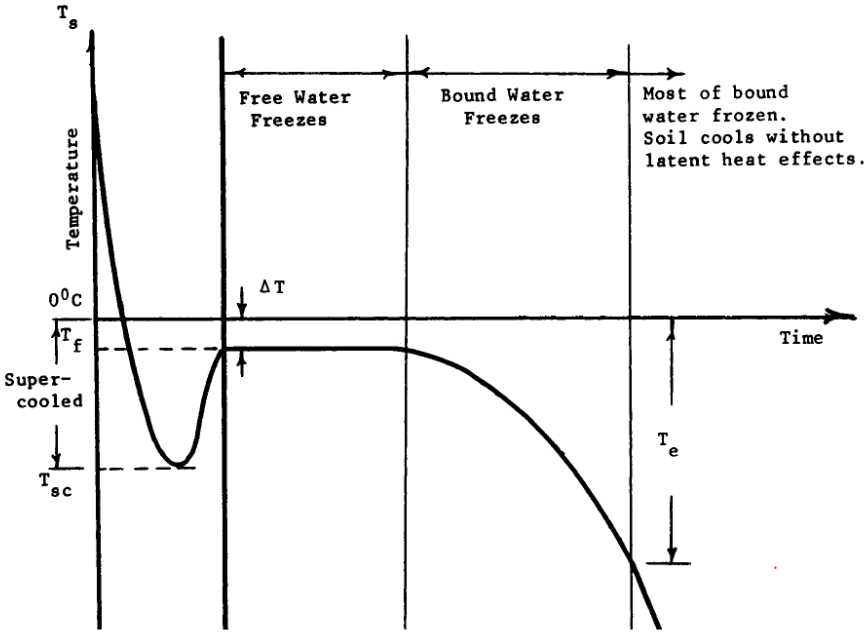

Figure 2.1: Cooling curve for soil water and ice. (Andersland and Ladanyi, 2004)

2.2 Premelting Theory

As mentioned above, water ("super-cooled" water) can stay liquid even below the freezing point. All the free water and most of the bound water (unfrozen water film on the soil particles) is frozen until T_e (about -70°C). This phenomenon can be explained in the microscopic level by the premelting theory.

According to the concept of premelting dynamics proposed by Wettlaufer and Worster (2006), there exist two types of premelting mechanisms that allow water to remain in an unfrozen state at temperatures below the bulk freezing point T_f: interfacial premelting and curvature-induced premelting (see Figure 2.2). The former gives rise to unfrozen film water separating ice from solid particles, whereas the latter generates supercooled pore water in a porous medium according to the Gibbs–Thomson law.

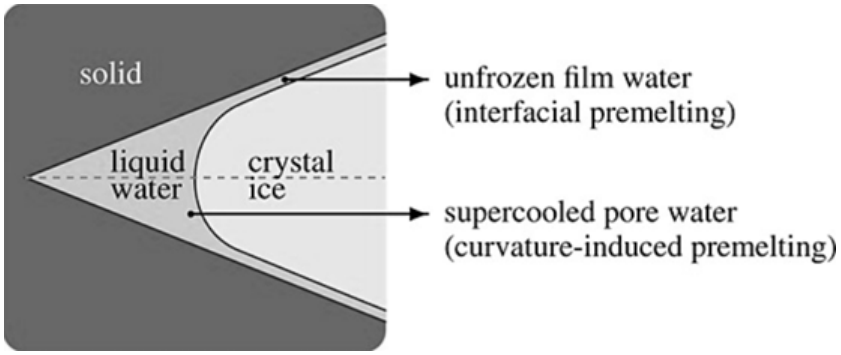

Figure 2.2: Curvature-induced premelting and interfacial premelting during intrusion of ice into a wedge-shaped wet-preferential solid. (Zhou and Meschke (2013))

Unfrozen (premelted) water exists at temperatures below the bulk freezing point for two reasons. Firstly, the equilibrium freezing temperature is depressed at a solid–melt interface that has its centre of curvature in the solid; and secondly, long-range intermolecular forces (such as *Van der Waals* forces or those that arise from interactions among soluble impurities) between different materials and phases can cause melt at free surfaces and interfaces in contact with another material. According to the first reason, the curvature-induced premelted water film forms. It exists between soil particles and tries to hold them together by the surface tension (same principle as capillary suction). According to the second reason, the interfacial premelted water film forms at the interface between crystal ice (C) and soil (S) grains. The soil and ice grains repel each other across the interfacially premelted liquid films as a consequence of the same inter-

molecular forces. Generally speaking, the reason for the existence of this liquid (L) film layer in soils lies in the fact that soils are hydrophilic and prefer contacting unfrozen water rather than ice. In other words, the total surface energy of the S–L and L–C interfaces is lower than the surface energy of an S–C interface. In order to push the liquid water to leave the solid interface and transform into ice, more energy is needed to lose. Therefore, the freezing point is depressed.

As illustrated in the premelting theory, the freezing point depression has a positive relationship with the area of interfaces. Therefore, for soils has a larger specific surface, such as silt and clay, the freezing point is normally below zero. As reported by Andersland and Ladanyi (2004): for cohesionless soils with small specific surface areas, T_f can be close to 0 °C; for fine-grained soils, T_f can be -5°C. It also suggests that, at the same temperature below the freezing point, fine-grained soils have higher unfrozen water content than coarse-grained soils.

2.3 Freezing Point Depression by Salinity

Water within soil pores may contain dissolved salt, which causes the freezing-point depression and will increase the unfrozen water content (Andersland and Ladanyi, 2004).

A review by Ladanyi (1989) also pointed out that in frozen soil, the increased salinity increased the unfrozen water content, which results in the increases of its creep rate and the decreases in the strength. Figure 2.3 illustrates a two-component system of water and salt ($NaCl$). It can be seen that a saturated $NaCl$ solution (23.3%) can remain completely liquid until -21°C (point C). The lowest temperature that a saturated solution can remain completely liquid is called eutectic temperature.

Here is a plain way to understand the freezing point depression. In order for water to freeze, the water molecules have to be slow enough to allow themselves to get close enough and link up into solid. To slow down the molecules, the kinetic energy must be reduced, which can be achieved by losing the thermal energy. Therefore, lowering temperature can make water start freezing. Adding salt in water make the solution system more "active", therefore it has to lose more energy to make the water molecules slow enough. As a result, the required freezing tem-

perature becomes lower.

The crystal lattice for ice is very selective; no substitutes for hydrogen or oxygen atoms are accepted (Pounder, 2013). If the solution is freezing slowly, the pure ice will form, and the impurities will be rejected and concentrated outside the pure ice. Furthermore, the concentrated impurities reduce the cohesion between ice grains. Therefore, controlling the freezing speed could change the properties of the ice, which is formed from the solutions. In an extreme situation, completely freezing a solution leaves only pure ice and pure salt crystals.

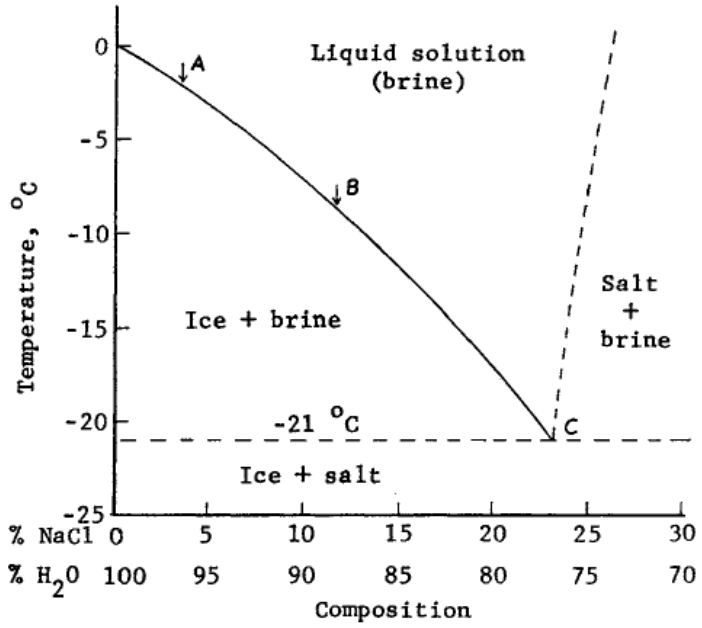

Figure 2.3: Solubility of ice in NaCl brine. (Andersland and Ladanyi, 2004)

Chapter 3

Measuring Principles

In this chapter, basic electrical and acoustic theories related to the laboratory tests will be introduced. Schematics will be used to explain the abstract electrical and acoustic concept more intuitively.

3.1 Electrical Principles

It is defined that there are two types of electrical charges, positive and negative. Objects that carried like types of charge repeal each other, and those that carried opposite types attract to each other. Coulomb's law describes this force of attraction or repulsion as the following equation:

$$F = K\frac{Q_1 Q_2}{r^2} \tag{3.1}$$

Where Q_1 and Q_2 are the electrical charges, r is the distance between the charges and K is a constant. This equation strongly resembles the equation of the law of universal gravitation formulated by Newton. The difference is that gravitation is always an attraction, whereas in electricity it depends on the nature of the charges. Besides, the force between the charges is way higher than the universal gravitation.

Driven by this electrical force, the electrons can flow. The electrical force manifests the electrical field, which is described by the flow lines, as shown in Figure 3.1. The strength of the field is represented by the spatial concentration of the flow lines. The point at an infinite distance is considered having 0 potential, while positive charges have positive potentials and negative

charges have negative potentials. The charges can only flow if there exists a potential difference, and the direction of the flow is always from high potential to low potential. Therefore, in Figure 3.1 (a), the charges flow from the positive to the negative. Besides, the charges flow from the positive to 0 (at an infinite distance) and from 0 to the negative. It also explains why there is no flow line between the two positive charges in Figure 3.1 (b) because there is no potential difference in between.

The electrical current is defined as the flow of charges, so the arrows in the electrical field also

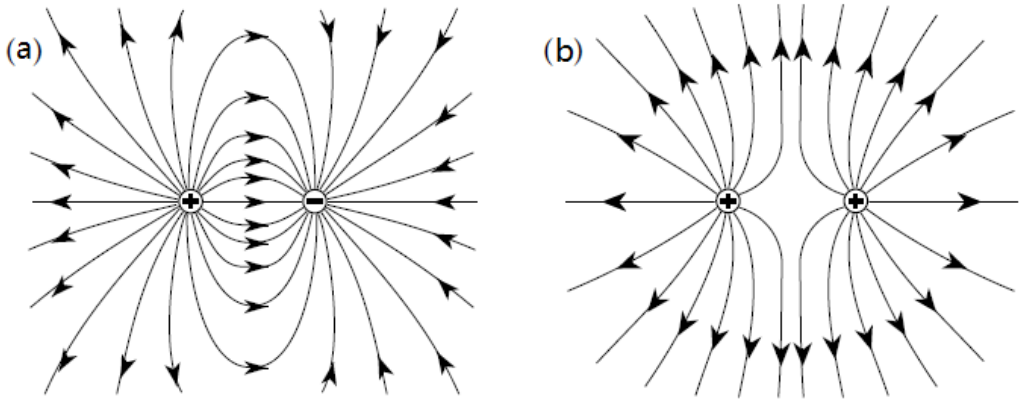

Figure 3.1: Planar cross-sections of electric field lines around point charges: (a) two equal and opposite and (b) two equal positive charges.(Lowrie, 2007)

indicate the direction of flows in Figure 3.1. In modern theory, results when the free electrons in a conductor are moving in a common direction. However, it has to notice that the direction of charge flow and the direction of the flow of electrons is opposite, which is due to that electrons are all negatively charged.

Electrical resistance is a restriction of the flow of electrons. The resistance depends on the types, geometry and temperature of the material that the current running through. The resistance occurs when the electrons collide with atoms; the amount of collision is different from one material to another. The collision transfer the kinetic energy of the running electrons to other kinds of energy. The electrical heater or light bulb are resistors, the energy lost in the collisions appears in the form of heat. Metals like copper or iron are usually used to make wires because metals have loosely bound electrons. They allow the energy transmits between the electrons, so the collision of electrons and atoms can be mostly avoided.

3.1.1 Ohm's Law

The German scientist Georg Simon Ohm established in 1827 that the electric current I in a conducting wire is proportional to the potential difference V across it (Lowrie, 2007). The linear relationship can be written as

$$R = \frac{V}{I} \tag{3.2}$$

Where R is the resistance of the conductor. The unit of resistance is the ohm (Ω). The unit of current is ampère (A), and one ampère corresponds to a flow of about 6,250,000,000,000,000,000 electrons per second past any point of a circuit (Lowrie, 2007). Since the number is the number of electrons of one Coulomb (C), the unit can also be written as C/s. The unit of electrical potential is voltage (V) which can also be presented as J/C (Joules/Coulomb), it represents the energy needed of moving every one Coulomb electrons from one point to another in an electrical field.

The resistance is dependent on the geometry of the conductor. For instance, a long wire has a higher resistance than a short one, and a thin wire has a higher resistance than a thick one. Therefore, resistivity (ρ) is used to describe the electrical property of the material without considering the geometry of the conductor. It determined by the mean free time between collisions (Lowrie, 2007). If the atomic arrangement causes frequent collisions, the resistivity is high, whereas a long mean free time between collisions results in low resistivity. The resistivity can be calculated as:

$$\rho = R\frac{A}{L} \tag{3.3}$$

where A is the area of the cross-section (see Figure 3.2). L is the length of the conductor. The unit of resistivity, ρ, is ohm-meter (Ωm). Substituting Equation 3.3 into Equation 3.2, the resistivity can be presented as:

$$\rho = \frac{VA}{IL} \tag{3.4}$$

3.1.2 Types of Electrical Conduction

Electric current passes through a material by one of three different modes: by electronic, dielectric, or electrolytic conduction. Electronic (or ohmic) conduction occurs in metals and crystals,

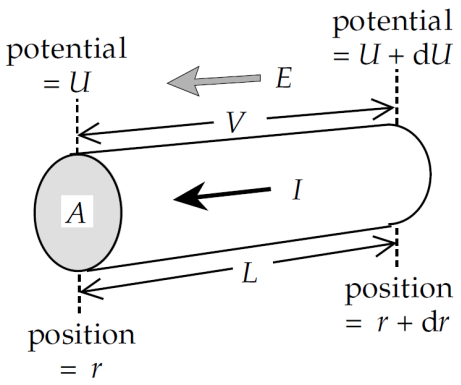

Figure 3.2: Parameters used to define Ohm's law for a straight conductor.(Lowrie, 2007)

dielectric conduction in insulators, and electrolytic conduction in liquids. (Lowrie, 2007)

Electronic conduction is typical of a metal. Metal normally has low resistance, because it has loosely bound electrons which can flow to other atoms, this is called electronic conduction. Therefore, the material which allows this electronic conduction is called a conductor.

Dielectric conduction occurs in insulators, which contain no free electrons. In some materials, such as rubber and glass, the electrons are tightly bound within their atoms. These materials are called insulators, where the electrons cannot pass through. However, when there applies an electrical field at this kind of material, the electrons will be displaced in the direction opposite to that of the field, while the heavy nucleus will be shifted slightly in the direction of the field. The atom or ion acquires an electric polarisation and acts as an electric dipole. The dielectric effect is depending on the relative permittivity of the material. The dielectric effect is unimportant in constant direct current (DC). However, in alternating current (AC) situation, the relative permittivity is frequency dependent. The higher the frequency, the greater is the effect of dielectric conduction. Some geoelectric methods utilise signals in the audio-frequency range, where dielectric conduction is insignificant, but ground-penetrating radar uses frequencies in the MHz to GHz range and depends on dielectric contrasts (Lowrie, 2007).

Electrolytic conduction occurs in aqueous solutions that contain free ions. $NaCl$ solution is a typical electrolyte, where the the molecule of $NaCl$ dissociates into separate Na^+ and Cl^- ions. The ions can be easily mobilised by the electrical field applied. The movement of ions causes a

current to flow. The direction of the current is identical to that of the positive ions and is opposite to the negative ions.

3.2 Acoustic Principles

The concept of frequency is essential in acoustics. For the sound that can be heard by the human's ear, the pitch of the sound reflects its frequency. Wave frequency is the number of waves that pass a fixed point in a given amount of time, or, in other words, how many times the sound source vibrates in a certain period. Otherwise, the magnitude of an acoustic wave is usually expressed in decibels (dB), which are unit based on the assumption that the ear approximately satisfies *Weber-Fechner law* (Michel, 2006). The sound wave characteristics related to the frequency (in air) are given in Figure 3.3.

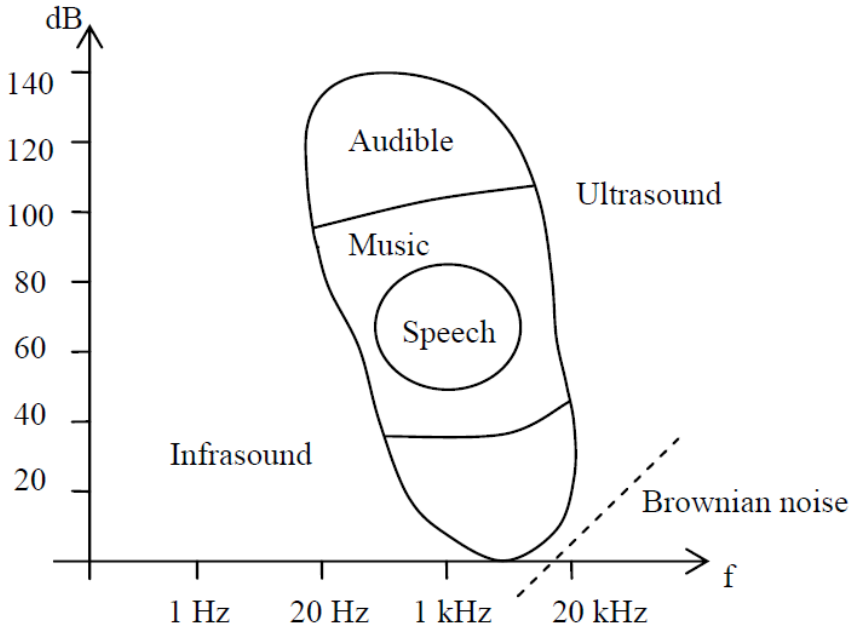

Figure 3.3: The sounds. (Michel, 2006)

3.2.1 Mechanism of Transmission

The mechanism of the transmission of the acoustic wave is based on the existence of "particles" whose position at equilibrium can be modified (Michel, 2006). All displacements related to any types of excitation except for those related to the transmitted quantity are generally ignored (i.e.

the motion associated with Brownian noise in gases). Three fundamental elements are required for the transmission of the acoustic waves: one or several emitters or sources, one receiver and a propagation medium.

There are mainly two types of acoustic waves, longitudinal wave and transverse wave. When the longitudinal wave propagating in a medium, the displacement of the particles in the medium is perpendicular to the direction of propagation. For a transverse wave, the displacement of the particles are parallel to the direction of propagation.

The fundamental mechanisms of wave transmission can be qualitatively simplified as follows.

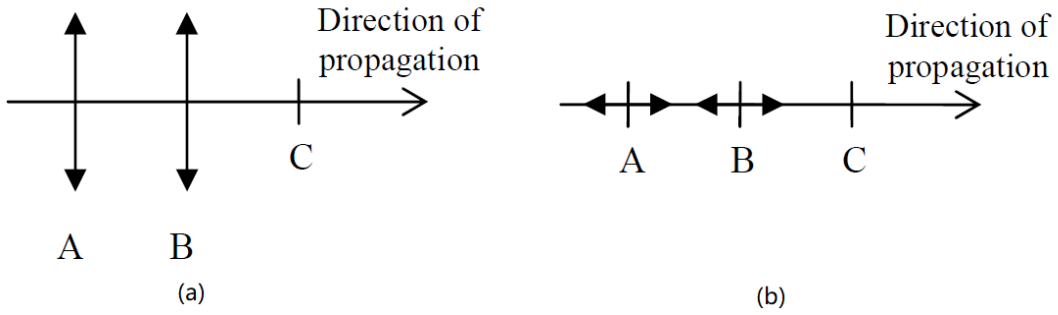

Figure 3.4: Two types of acoustic waves: (a) transverse wave; (b) longitudinal wave. (Michel, 2006)

A particle B, adjacent to a particle A set in a time-dependent motion, is driven, with little delay, via the bonding forces; the particle A is then acting as a source for the particle B, which acts as a source for the adjacent particle C and so on (see Figure 3.4).

The propagation of longitudinal wave can be considered as driven by compressing the particles in a row. The first particle is compressed first, then it rebounds and compresses the particle next to it. Therefore, the longitudinal wave is also called a compressional (or dilatational) wave. Likewise, a transverse wave can be considered the transmission of shear force, so it is also known as the shear wave. Besides, the longitudinal and transverse wave are also called respectively primary wave (p-wave) and secondary wave (s-wave).

3.2.2 Wave Velocity

Since the propagation of P-wave and S-wave are related to compression and shear, the velocity of these two types of waves depends on the mechanical properties of the medium they travel through. According to Lowrie (2007), the P-wave velocity (V_P) and the S-wave velocity (V_S) are expressed as:

$$V_P = \sqrt{\frac{M}{\rho}} = \sqrt{\frac{K + \frac{4}{3}G}{\rho}} \tag{3.5}$$

$$V_S = \sqrt{\frac{G}{\rho}} \tag{3.6}$$

Where M is called the p-wave modulus, also known as the longitudinal modulus or the constrained modulus (it is defined as the ratio of axial stress to axial strain in a uniaxial strain state); G is the shear modulus, and ρ is the density of the medium.

As it can be seen in Equation 3.5, M equals to $K + \frac{4}{3}G$, where K is the bulk modulus, and G is the shear modulus. The s-wave is only related to the shear modulus. Therefore, in a solid medium, the acoustic wave is always composed of p-wave and s-wave; in fluid, the p-wave is dominant, the s-wave depends on the viscosity of the medium.

3.3 Application in Frozen Soil

Table 3.1: Physical properties of common constituents of frozen soil.

Materials	Bulk Modulus [GPa]	Shear Modulus [GPa]	Density $[kg/m^3]$	Resistivity $[\Omega m]$
Quartz	37.0[*1]	44.0[*1]	2650[*1]	$10^{10} \sim 2 \times 10^{14}$
Feldspar	37.5[*1]	15.0[*1]	2620[*1]	Non-conductors
Plagioclase	76.0[*1]	26.0[*1]	2630[*1]	$> 10^4$
Water	2.2[*2]	0.0	1000	$1 \sim 1000$ (Fresh Water)
Ice	8.4[*3]	3.7[*3]	920	$10^5 \sim 10^7$ (Pure Ice)

Notice: Descriptions and ranges, which have come from several sources, are only approximate.
[*1] Source: Carmichael (2017);
[*2] Source: Toksöz et al. (1976);
[*3] Derived from the ultrasonic measurements made by King (1984);

Saturated frozen soil can be considered as a three phases system: minerals, ice and water. Generally, the minerals have way higher bulk and shear modulus than ice and water, as shown

in Figure 3.1. Besides, the elastic modulus of ice and water are also quite different. In terms of the electrical resistivity, the minerals and ice have way larger resistivity than unfrozen water. If the pore fluid has high salinity, the difference will be even more significant.

Since water has very different electrical and acoustic properties than the other two components, it is feasible to distinguish the unfrozen water content in the three-phase system. Since the porosity can be measured by conducting experiments, the proportion of each component can be expressed by assuming an unfrozen water saturation, S_w. Furthermore, the electrical and acoustic parameters of each component can be determined by previous studies. Then the S_w can be solved by using a proper model.

Chapter 4

Laboratory Tests

In this chapter, the soil sample, measurement setup and calibration of the setup will be presented. The soil sample used in this test is *Halden Silt*. This joint measurement consists of two system: electrical measurement system and acoustics measurement system. The electrical measurement system measures the electrical resistance of the sample in a tube-shape sample holder, and the resistivity of the frozen soil will be calculated with the measured dimensions of the sample holder. Meanwhile, the acoustic measurement system measures the travel time of the acoustic waves propagation in the sample, and the velocity will also calculated with the distance of the placement of the acoustic transducer and receiver. The calibration is conducted based on both the precise conductivity instrument and existing literature.

4.1 The Soil Sample

The soil sample is provided by the program *Norwegian Geo-Test Sites (NGTS)* supported by *The Research Council of Norway Infrastructure program*. It has established five national test sites located near Oslo and Trondheim and one on Svalbard. The silt sample used in this test is from Halden, which is located in Southeastern Norway, approximately 120 km south of Oslo (see Figure 4.1). All the results are presented in Øyvind Blaker and L'Heureux (2019), which is accepted by *AIMS Geosciences* but not published yet. According to the depth of where it has been collected, the sample is divided into 4 units as shown in Table 4.1. The sample used in this test is taken from *Hole: SP8-DP3* at the depth $4.75-5.15m$, which belongs to *Soil Unit II*. The grain size distribution is show in Figure 4.2. As described by Øyvind Blaker and L'Heureux (2019), the fines

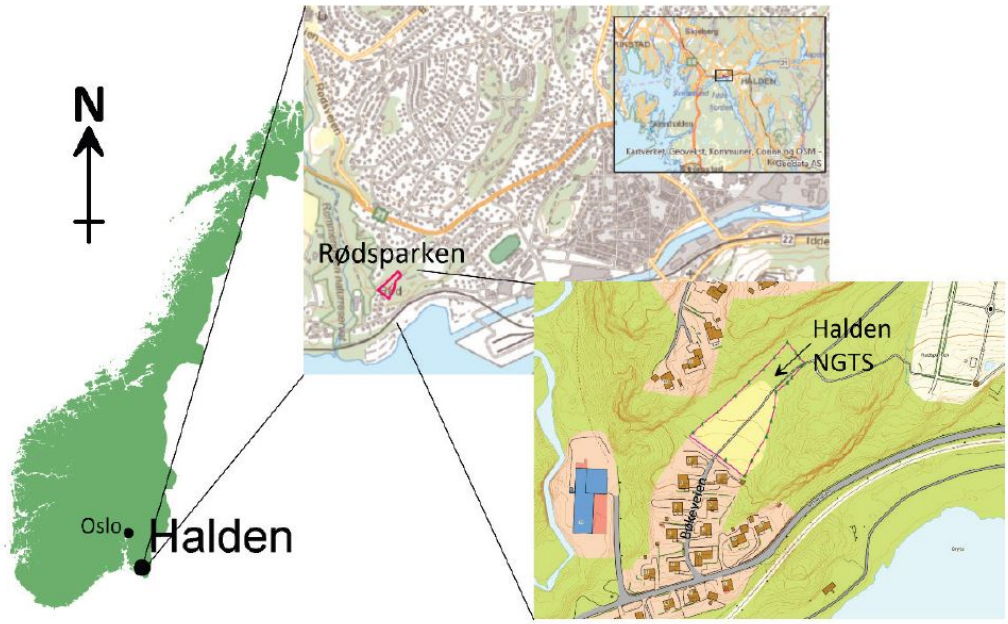

Figure 4.1: Site location in Halden, Norway. (Øyvind Blaker and L'Heureux, 2019)

Table 4.1: Summary of *Halden Silt* of different units. (modified from Øyvind Blaker and L'Heureux, 2019)

Soil Unit	Depth Range [m]	Descriptions
I	0.0 - 4.5	SAND, clayey, silty, fine, loose to medium dense, with organic material, brownish grey.
II	4.5 - 12.1	SILT, sandy, clayey, low to medium strength, homogeneous, mottled, occ. shell fragments, brownish grey.
III	12.1 - 16.0	SILT, sandy, medium to high strength, homogeneous, highly bioturbated, mottled, occ. shell fragments, occ. black organic material, brownish grey.
IV	16.0 - 21.3	CLAY, silty, low to medium strength, slightly laminated, occ. shell fragments, occ. drop stones.

content in *Soil Unit II&III* is generally higher that 80%, and the clay content is fairly constant at around 8%. According to *Unified Soil Classification System (USCS)*, these soils are classified as silty clay with sand to lean clay with sand.

The soil classification triangle is shown in Figure 4.3 (a). However, according to *USDA (United States Department of Agriculture)* the soil samples taken from the Halden area can also be summarized as silt loam as shown in Figure 4.3 (b). The constituents of *Soil Unit II* are shown in Table 4.2.

Table 4.2: Constituents of *Soil Unit II* based on X-ray diffraction analyses.

Unit	Depth [m]	Quartz [%]	Potassium Feldspar [%]	Plagioclase [%]	Muscovite/Illite [%]	Chlorite [%]	Amphibole [%]	Pyrite [%]
II	6.2	41	12	30	8	3	6	trace

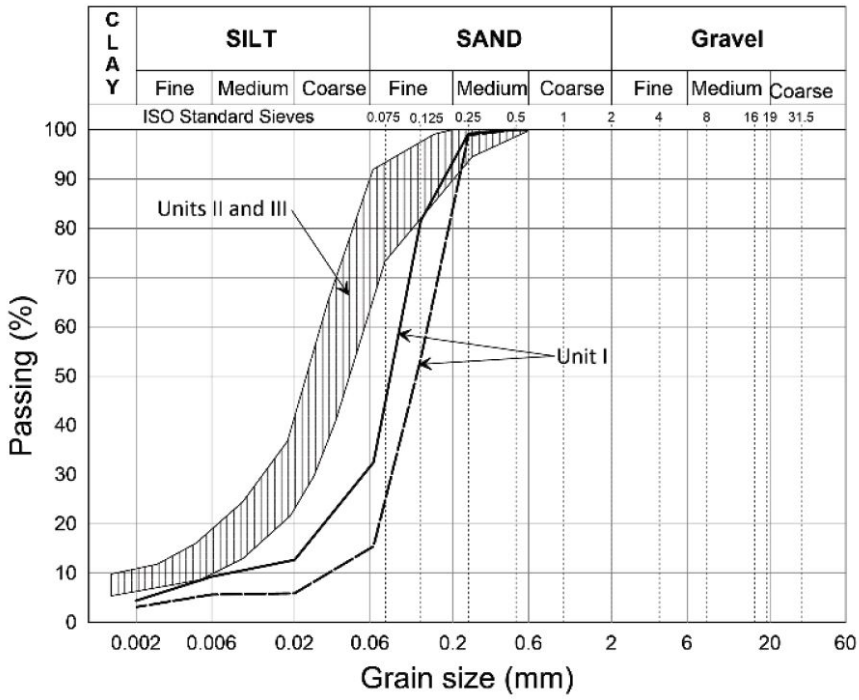

Figure 4.2: Grain size distribution of the silt sample. (Øyvind Blaker and L'Heureux, 2019)

4.2 Test Apparatus

All the equipment used in the tests, except for the computer and the freezer, is shown in Figure 4.4. To conduct the joint measurement tests, a sample holder is essential for holding the sample and placing the acoustic sensors and the electrodes.

4.2.1 Sensors and Data Loggers

The acoustic sensors are two piezo pads (*7BB-20-6L0* manufactured by *Murata*) with the diameter of $14mm$ and thickness of $0.2mm$. The sensors convert the pressure to an electrical charge by using the piezoelectric effect. In order to prevent the interference from the electrical signals from the transmitting piezo pad and the electrical measurement system, the piezo pads are coated with insulation silicone compound. For the electrical measurement, the current electrodes are steel mesh, and the potential electrodes are steel pins. The temperature sensor is made from a *MCP9700A* low-power linear active thermistor manufactured by *Microchip*. The temperature is calculated from the voltage measured by the sensor. $0°C$ corresponds to $499mV$, and every $9.84mV$ change in the voltage corresponds to 1 Celsius degree change in the temper-

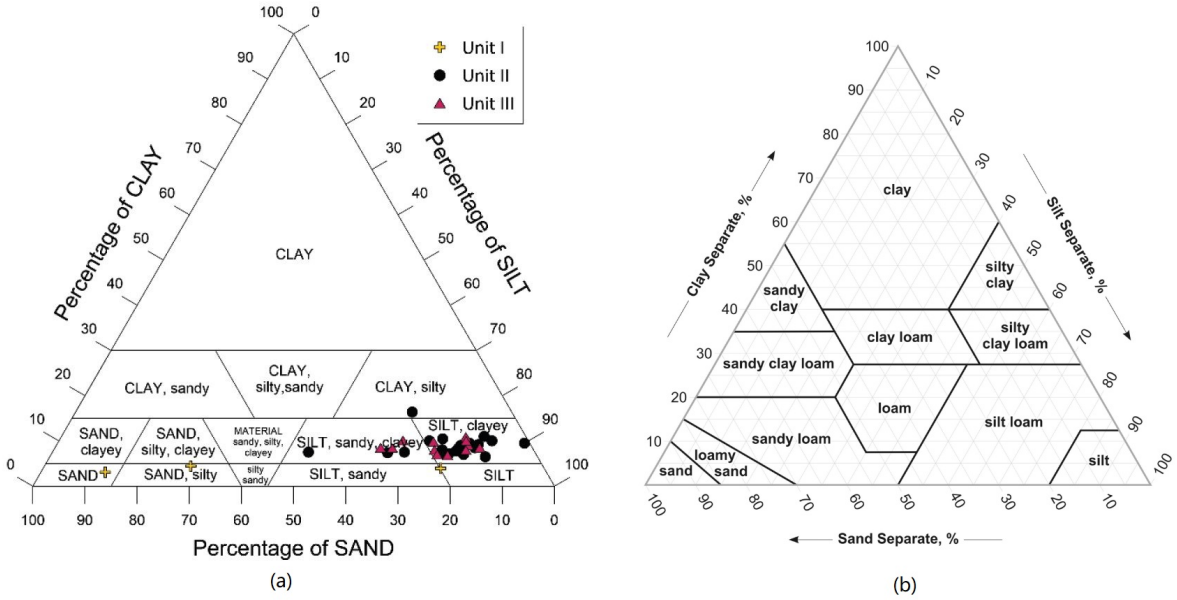

Figure 4.3: (a) Soil classification triangle (Øyvind Blaker and L'Heureux, 2019); (b) Soil classification triangle by *USDA*.

ature.

The sensors and the electrodes are connected to data loggers, and the data loggers record the measurements. The acoustic sensors are connected to an *NI USB-6366* data logger; the electrical measurement system uses an *NI USB-6211* data logger; the temperature sensor is connected to an *NI USB-6210* data logger. All the data loggers are manufactured by *National Instrument*. The measured data are processed in *LabVIEW*.

4.2.2 Sample Holder

In the geophysical field tests, a two-electrodes probe was used for resistivity measurement at the beginning. However, the erratic and unreproducible probe-to-surface contact resistance has been reported by many researchers (Wenner, 1915; McCorkle, 1931; Edlefsen and Anderson, 1941; Kirkham et al., 1950). Wenner (1915) firstly presented a theoretical method of using four electrodes system which attempted to eliminate the contact resistance. McCorkle (1931) improved this method by suggesting using equally-spaced, in-line electrodes. This method is the well-known *Wenner Array*.

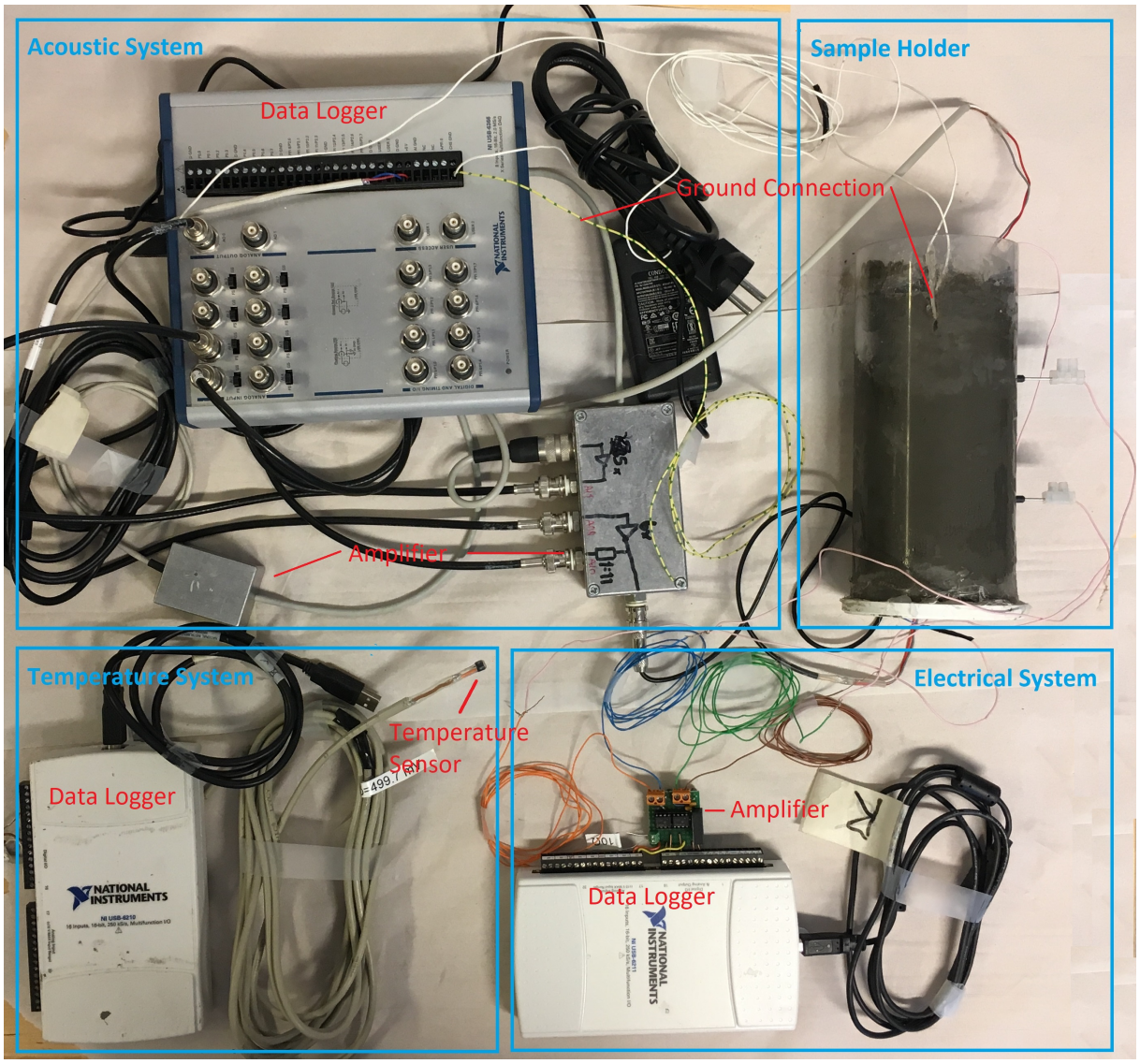

Figure 4.4: Photo of the test apparatus.

Figure 4.5 illustrates the most commonly used array of the four electrodes measurement, *Wenner Array*. In this schematics, A and B are the current electrodes providing the current, M and N are the potential electrodes measuring the potential between these two electrodes. The spacing of these two electrodes is all the same, notes as a. According to Equation 3.4, the apparent resistivity can also be calculated with the following analogy equation, which is assuming the cross-section is a hemisphere (as shown by the equipotential line, and the area of the hemisphere is $2\pi r^2$, where r is the radius).

$$\rho = \left[\frac{2\pi}{(1/AM) - (1/BM) - (1/AN) + (1/BN)} \right] \frac{\Delta V}{I} \tag{4.1}$$

In *Wenner Array* the spacing of $A-M$, $M-N$ and $N-B$ are identical, and for the other arrays

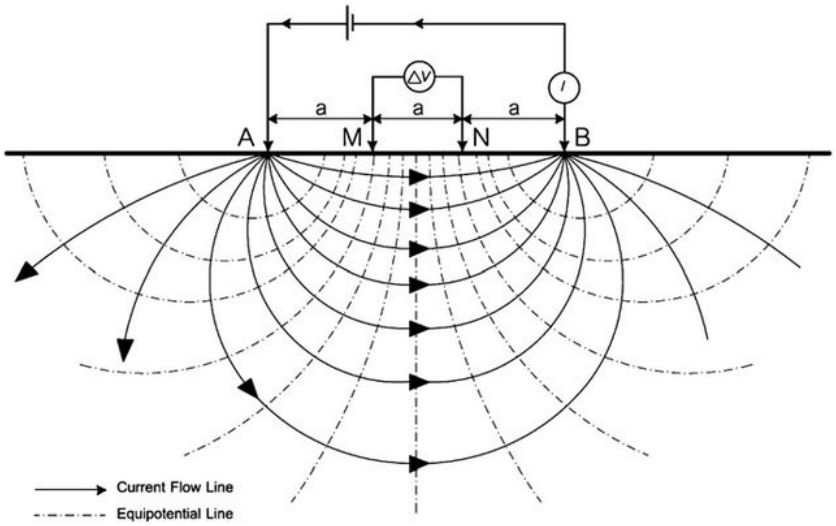

Figure 4.5: The schematics of *Wenner Array* method. (Wiwattanachang and Giao, 2011)

the spacing varies. Nevertheless, the principles of all the methods with different arrays are the same. These electrical measurement methods with different arrays give relatively accurate apparent resistivity for large scale field tests. However, the apparent resistivity is only a qualitative estimation of the electrical parameters of the medium, which assumes the medium were homogeneous (Meheni et al., 1996). Also, for small scale laboratory tests, these mature geophysical methods can not be directly applied because of the geometrical effects. However, the enormous tests with the uses of these in-situ methods verified the feasibility of applying electrical measurement on detecting the properties of geomaterials.

Applying the same concept in laboratory test, the four electrodes setup as shown in Figure 4.6 has been used by many researchers (i.e. Rust et al., 1952, Vanhala and Soininen, 1995, Polder et al., 2000 and Brown et al., 2004,) for rock or soil tests. The current electrodes provides the current, and the potential electrodes measure the difference of the potentials. Since the current flow lines are parallel and the equipotential lines are perpendicular to the flow lines, the resistivity can be calculated by using Equation 3.4.

The sample holder is made of plexiglass, which is a transparent, insulating material. The transparency of the material allows to observe the changes in soil samples before and after freezing; the electrical insulation ensures the accuracy of resistivity measurement. The compositions and

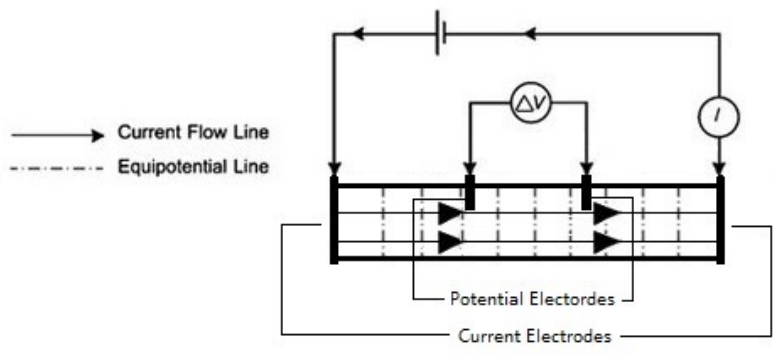

Figure 4.6: The schematics of four electrodes measurement in laboratory test.

the geometry of the sample holder are shown in Figure 4.7. It can be seen that the sample holder is a tube. The bottom end is glued to a plastic plate by a silicon rubber compound. This adhesive is also used at the pin-tube interfaces as a sealant. The potential electrodes are gold plating pins, and the current electrodes are steel meshes. The diameter of the meshes are $0.5mm$, and the spacing between each wire is around $2mm$. The pins are $20mm$ long, and the depth in the tube is $1mm$. Besides, all the electrodes are connected to the data logger through steel wires. The wire connected to the bottom current potential electrode leads to the outside through a small hole on the plastic plate. The upper end is open, which reserves some space for the volume expansion during freezing.

4.2.3 Geometry of the Electrodes

The contact resistance at the current electrodes can be eliminated by using the four electrodes method, but the contact at the potential electrodes still exist. To find out the geometry of the electrodes, three setups have been designed, as shown in Figure 4.8. Aluminium plates, copper meshes and steel pins are used as current and potential electrodes. The results of applying a

Table 4.3: The average of the resistivity measured by three different setups.

Setup	Plate-Pin	Mesh-Pin	All Mesh
Average Resistivity [Ωm]	76.71	78.65	74.72
Difference to the Average ($76.69\Omega m$)	0.00%	2.56%	2.57%

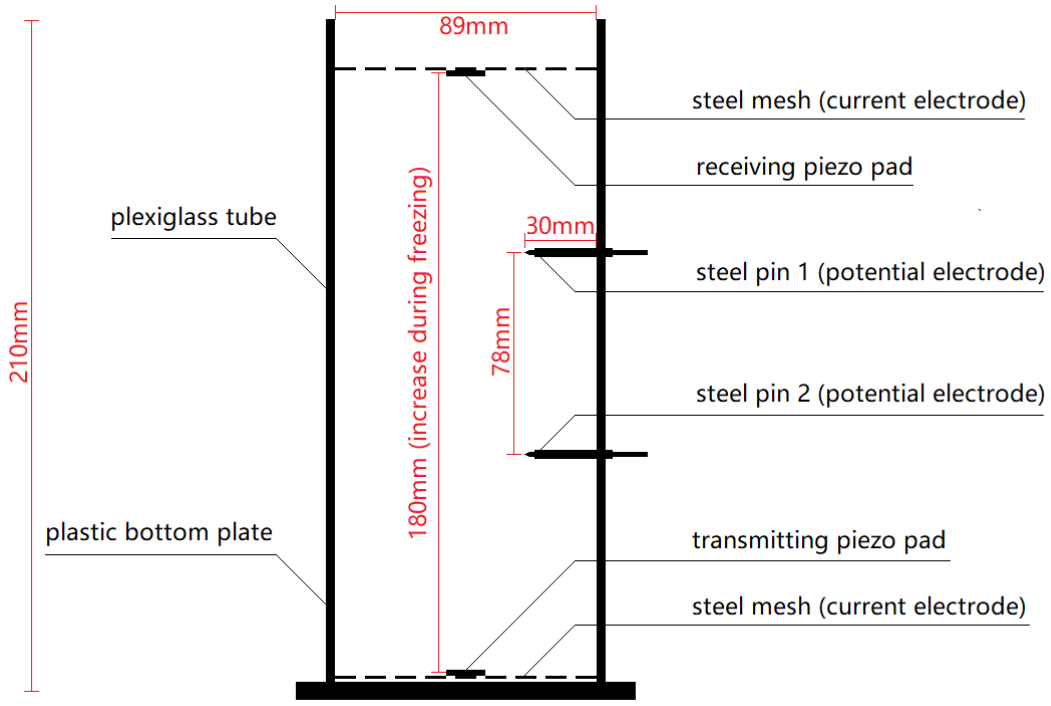

Figure 4.7: The schematics of the sample holder.

$0.5Hz$ alternating square-wave current on the tap water samples are shown in Figure B.4 in Appendix B. "+/−" represents the direction of the alternating current. It can be seen that the setup using copper meshes as both current and potential electrodes gives the most stable, non-polarity-dependent results. Anyhow, the average of the results of all the three setups (also see in Table 4.3) are similar, the difference is within 2.57% compared to the average resistivity of these three setups, which is acceptable. Using meshes as the current potential will change the inner structure of the sample, which will influence the influence of the freezing process. Even though the all-mesh setup gives the most favourable results, a pin is chosen to be the potential electrodes. In terms of the current electrodes, the plate electrodes can be easily stuck in the tube, when it is pushed by the nonuniform expansion of the sample during the freezing process. Therefore, the mesh current electrode and pin potential electrode combination becomes the final choice.

4.2.4 Insertion of the Potential Electrodes

The depth of the pin inserting into the tube has also been considered. Giao et al. (2003) conducted the resistivity test with a $75mm$ diameter tube sample holder, for different penetrations,

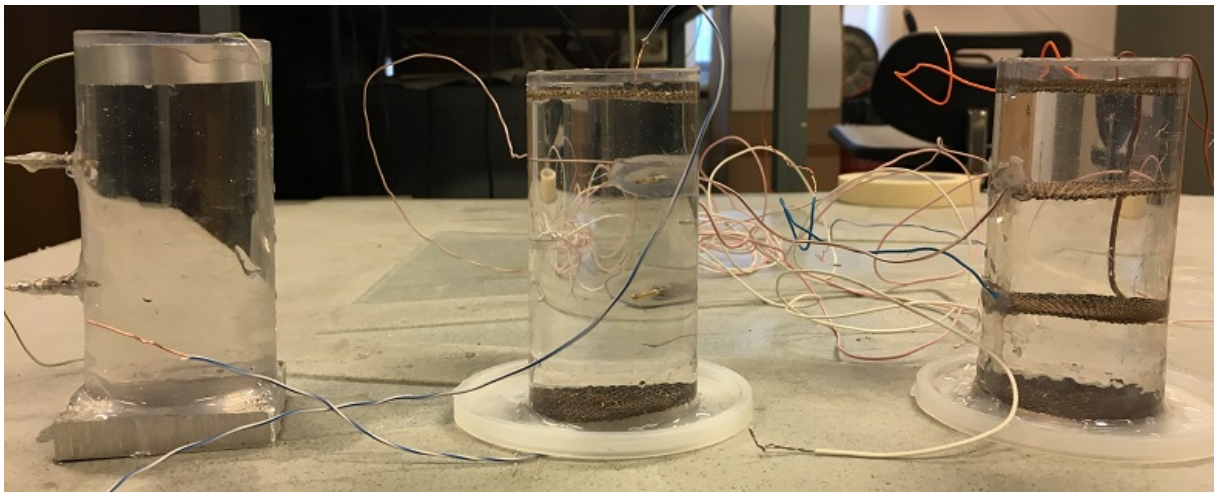

Figure 4.8: Three setups for studying the geometry effect of the electrodes: (left) aluminium plates with steel pins; (middle) copper meshes with steel pins; (right) copper meshes.

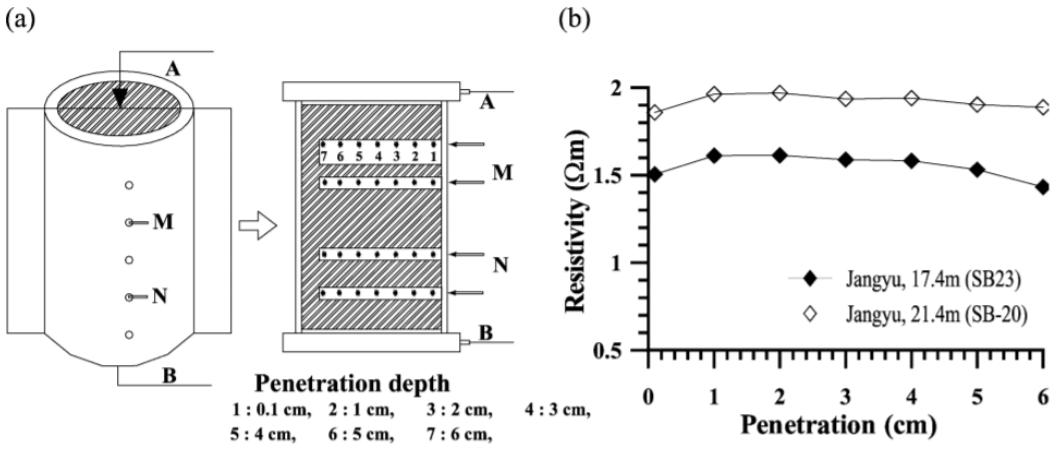

Figure 4.9: Testing with different electrode penetrations: (a) setup; (b) results. (Giao et al., 2003)

i.e., 0.1, 1, 2, 3, 4, 5 and 6 cm, the values of electric resistivity measured were practically the same. (see Figure 4.9) Also, Vanhala and Soininen (1995) reported the effect of the material of electrodes on contact resistance. $Ag-AgCl$ electrodes have been used in many electrical laboratory tests (e.g. Nelson et al., 1982; Vinegar and Waxman, 1984), they showed some advantages in comparison with pure metal electrodes. However, due to the restriction of the time and fund, the electrodes used in this thesis are steel mesh and gold-plating pins, which the laboratory has already. Besides, Vanhala and Soininen (1995) inclined potential electrodes can cause a phase shift to the measurement, but the effect can be ignored when the separation between the electrodes exceeds $5cm$. For the self-made sample holder, the separation is $7cm$, so the effect of inclination is negligible. (see Figure 4.10)

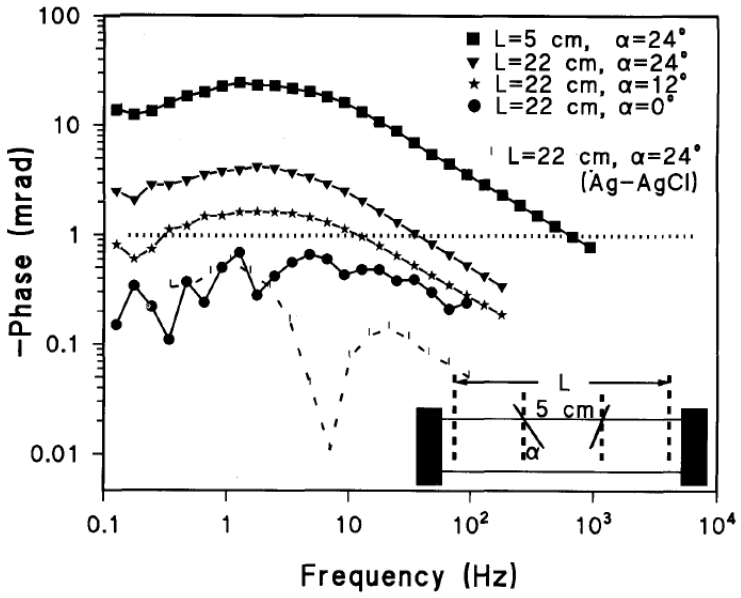

Figure 4.10: The effect of electrode position on the phase spectra for ground water. Inclined metal electrodes produce an erroneous phase Spectrum. (Vanhala and Soininen, 1995)

4.2.5 Separation of the Piezo Pads

The piezo pads are placed at between the mesh current electrodes and the soil sample, at both ends of the sample holder. The length of the sample holder is $21cm$. However, the soil sample is not filled. The height of the soil sample in the sample holder is initially $18cm$, and the volume will expand due to the expansion of ice. Therefore, the final separation between these two piezo pads is around $19cm$.

Since the transmitting piezo pad and the receiving piezo pad are both connected to the same data logger, an electromagnetic noise is recorded right after the signal has been sent as shown in Figure B.7. To connect the data logger to the ground and the sample can reduce this noise, however, the reduced noise still last approximately $25\mu s$. As this noise will significantly influence the determination of the first arrival wave, the soil sample should be long enough to ensure at least $50\mu s$ travel time. According to Nakano et al. (1972), the p-wave velocity of water saturated *Hanover Silt* is around $3900m/s$ at -18°C. Assuming *Harden Silt* has the same p-wave velocity at the same condition, the separation should be at least $19.5cm$. Considering the silt sample used in our tests will be saturated with $NaCl$ solution, which will slow the p-wave velocity, the separation of $19cm$ is feasible.

4.2.6 Ground Connection

As shown in Figure 4.11, there is a huge signal (already exceed the range in the graph) appears almost at the same time with the transmitted wave before the ground connection. Also, the signals after this huge signal are fluctuating at a lower centre line below 0 amplitude, and it also influences the determination of the first arrival wave. This abnormal signal is an electromagnetic noise, and part of it is caused by the data logger. It can be reduced by connecting the ground wire shown in Figure 4.4 and the sample holder to the ground and the connection between the sample holder and the ground contributes the majority of the reduction. After the ground connection, the electromagnetic noise has been significantly reduced, and the range of the location of the first arrival wave has been narrowed.

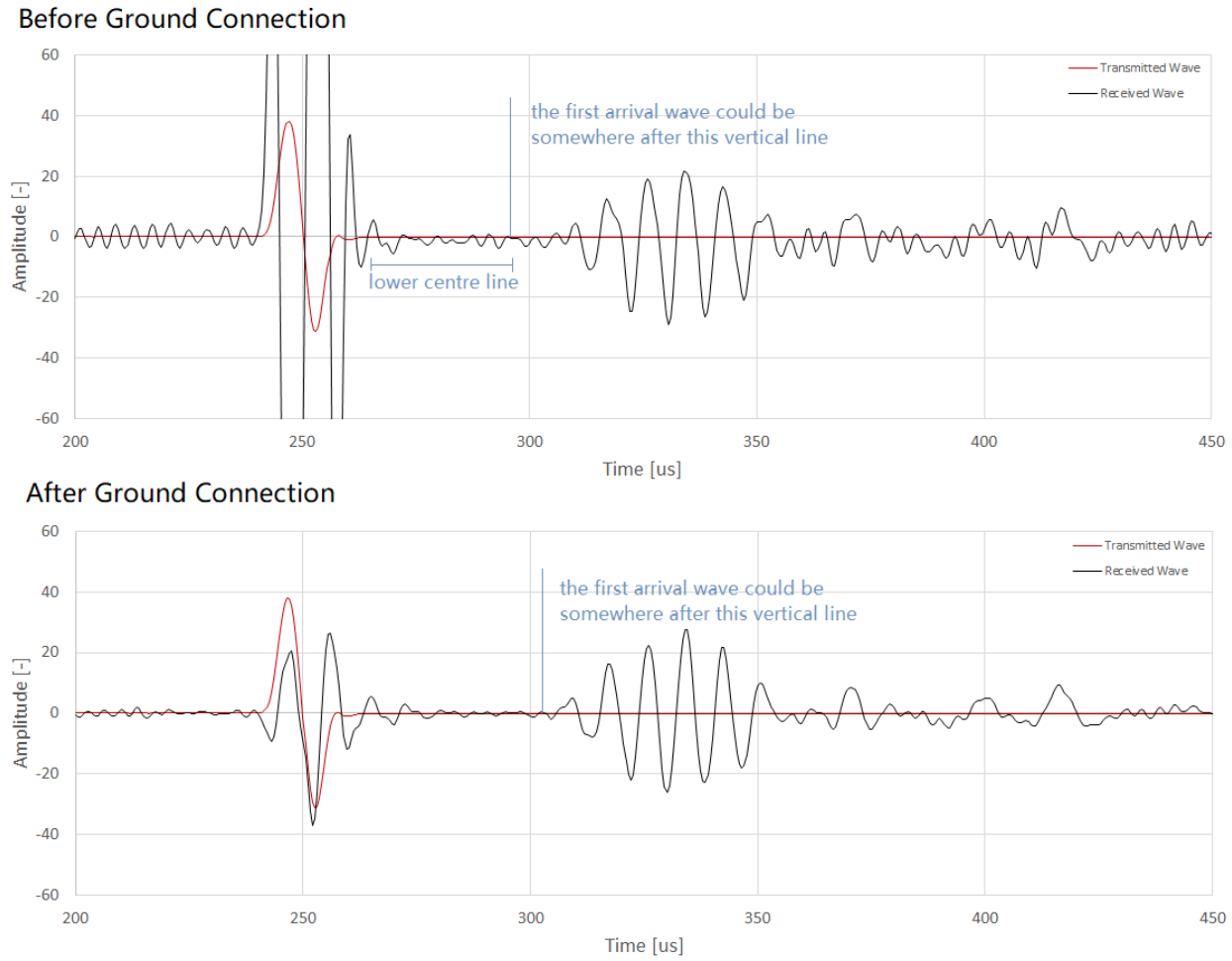

Figure 4.11: The effect of ground connection on the measured wave in frozen silt.

4.2.7 Data Logger for the Electrical Measurement

The electrodes equipped on the sample holder are connected to a data logger by wires. The data logger used in the electrical measurement is *USB 6211* manufactured by *National Instruments* (Figure 4.4), it provides the inputs to and measures the outputs from the system at the same time. As shown in Figure 4.13, the resistivity of permafrost (frozen soil) ranges from several hundred to one hundred thousand $\Omega \cdot m$. In order to have a measurable current, the $+10V$ analogue output is chosen as the input of the test. Besides, a $100X$ amplifier is added to the system to enhance the signal as shown in Figure 4.4.

The simplified measurement circuit is shown in Figure 4.12. The data logger provides elec-

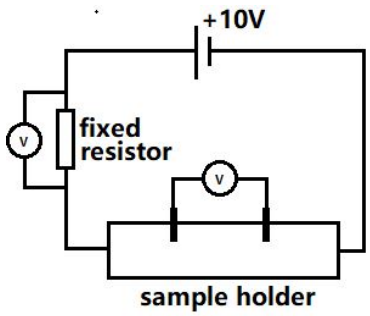

Figure 4.12: The schematics of the measurement circuit.

trical potentials, instead of current. However, the current can be calculated by dividing by the resistance of the fixed resistor. In total, there is only $10V$ potential applied on the system; if the resistance of the sample is too large, only very small potential is applied on the fixed resistor. Since the current is calculated from the potential on the fixed resistor, the environmental noise can easily affect the result of the calculation. As it can be seen in Figure 4.13, the unfrozen clay has the only resistivity under $100\Omega m$, and that of frozen soil can be three orders of magnitude higher. Therefore, the resistor connected to the green module is designed replaceable, in order to adapt the soil samples at unfrozen and unfrozen states.

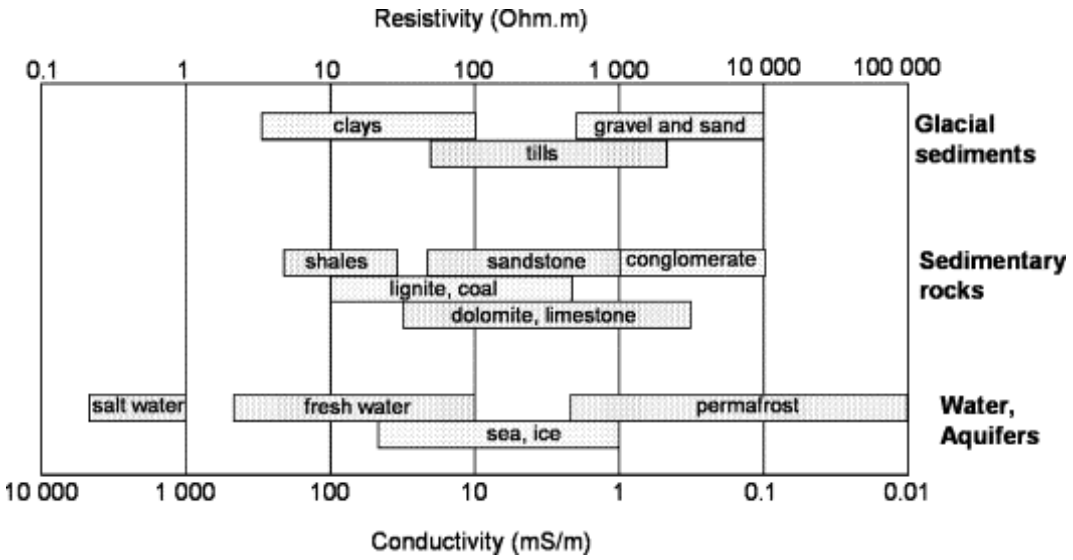

Figure 4.13: Typical ranges of electrical resistivities of earth materials (after modified Palacky 1987).

4.3 Electrical Measurement System

Resistivity measurement is a common geophysical measurement method. It is widely used in agricultural soil monitoring, contaminated soil detecting and either mining or oil&gas exploration. The strong correlation between the electrical properties and the other properties of the geomaterial makes the electrical method particularly promising in geotechnical tests.

The electrical measurements are recorded by the data logger. The recorded data still need to be processed to eliminate the noise and to calculate the electrical resistivity. Otherwise, the system needs to be calibrated to ensure that the data obtained is valid.

4.3.1 Electrical Data Processing

The *LabVIEW* program used to control the data logger and conduct calculation are shown in Figure B.1. The program is composed by the front panel and block diagram. The front panel displays the test results and allows the user to control the program during measurement, and the block diagram is the place to conduct visualization programming. The block diagram consists of two parts: *Current Control* (in upper frame) and *Potential Measurement* (in lower frame).

The *DAQ Assistant (output)* module in the *Current Control* directly control the data logger to generate potential output, the sampling rate is set as $10k\ Hz$. The wave form used in this test

is the sine wave, which is controlled by the *Simulate Signal* module. The two outer controllers allow adjusting the frequency and amplitude in the front panel.

The *DAQ Assistant (input)* module in the *Potential Measurement* controls the measurement recording and data processing. Three channels on the data logger are used for measuring the potential on the fixed resistor, the potentials on pin 1 and pin 2, respectively. The current is calculated by the potential on the fixed resistor, and the potential is the difference of the potentials on pin 1 and pins 2. The resistance can be calculated then according to Ohm's law.

Before the calculation, the measured data need to be processed by the case structures called *Remove DC* and *Filter*. Since the experiment is using AC, the stable current is from the electrochemical reaction in the sample. If there is only AC, the average potential is displayed as a sine wave, which has an average potential of 0. If there is DC, the average potential should be subtracted; this is what has been done in the *Remove DC* case structure. Because of the current can be at the magnitude at 10^{-6}A, the environmental noise in the laboratory (e.g. fluorescent lamp, the vibration of the ventilation, electromagnetic wave from another instrument). Therefore, the *Filter* case structure is used to extract only the data at a similar frequency as the applied AC.

Through some simple arithmetic, the resistance of the sample can be obtained (the average of all the results). Then the resistance is multiplied by a coefficient a to get the resistivity. According to Equation 3.4, the coefficient a can be presented as:

$$a = \frac{A}{L} \tag{4.2}$$

For this tube sample holder with an inner diameter of 89mm (radius r is 45.5mm) and the separation, L, between two pins is 70mm, the coefficient a can be calculated:

$$a = \frac{\pi r^2}{L} = \frac{0.0455^2 \pi}{0.070} = 0.0888 \quad (m) \tag{4.3}$$

So the resistivity can be calculated by using the resistance measured by this system:

$$\rho = 0.0888R \quad (\Omega m) \tag{4.4}$$

4.3.2 Calibration

Before applying this resistivity measurement system on measuring frozen soil samples, some samples (e.g. tap water, $NaCl$ solution) with known resistivity have been tested to calibrate this system.

Under an external electric field, the charges influence electric force and get displaced and aligned to form dipoles; this ends up entire system being polarised. This polarisation phenomenon can weaken the original external electric field, which leads to influence the electrical measurement. Therefore, the alternating current (AC) is applied in this system to reduce the effect of polarisation.

As shown in Figure 4.14, the resistivity has been found dependent on the measuring frequency

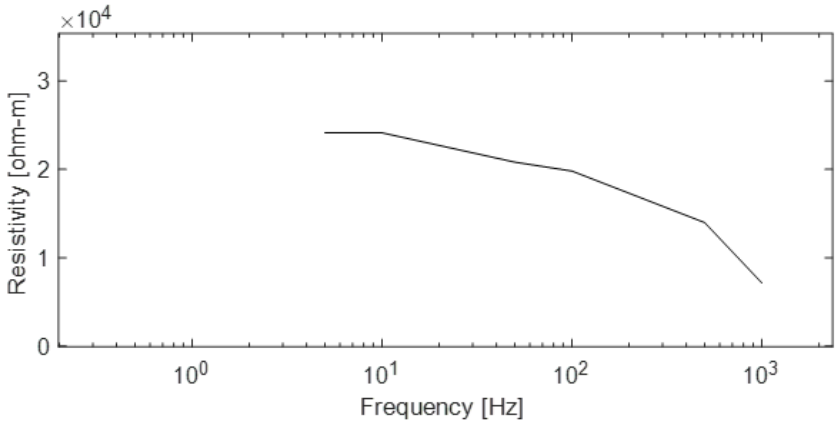

Figure 4.14: The influence of the frequency on the resistivity of *Halden Silt* saturated with tap water at -10.8°C.

in frozen *Halden Silt* saturated with tap water during our trial tests. The resistivity drops significantly with ascending frequency.

As detailed by Visacro and Alipio (2012) and by Alipio and Visacro (2014), the effective conductivity of soil comprises of two components, a constant one, referred to as the conventional low-frequency conductivity, being related with free ions and electrons, and a frequency-dependent one associated with losses due to polarisation processes. Zhou et al. (2015) concluded that the frequency-dependent one corresponds to the imaginary parcel of permittivity, which presents a variation with the frequency of the applied electric field. Visacro and Alipio (2012) also men-

tioned that a significant effect of the frequency dependence of soil parameters for soils with resistivity values higher than $500\Omega m$ and a reduced effect for soils with a resistivity of around $100\Omega m$. To reduce the effect of the losses during the polarisation process, $10Hz$ is chosen as the frequency of the AC of our self-made system. Therefore, the measured resistivity is corresponding to the conventional low-frequency conductivity.

Vanhala and Soininen (1995) reported that the resistivity of tap water was $80\Omega m$ over a large range of frequency. By using *YSI 3200 conductivity instrument* as shown in Figure 4.15, the resistivity of the tap water obtained from NTNU geotechnical laboratory is 76 Ωm at $18.26°C$. The resistivity will slightly change with the changing temperatures, but the variation is negligible. Since the sample holder for *YSI 3200 conductivity instrument* is only designed for liquid, the resistivity of $11460ppm\ NaCl$ solution is also used to calibrate the system. According to the *Schulumberger $NaCl$ Solution Resistivity Chart* as shown in Figure B.5, the resistivity of $11460ppm$ $NaCl$ solution at room temperature (around $20°C$) is about 0.58 Ωm.

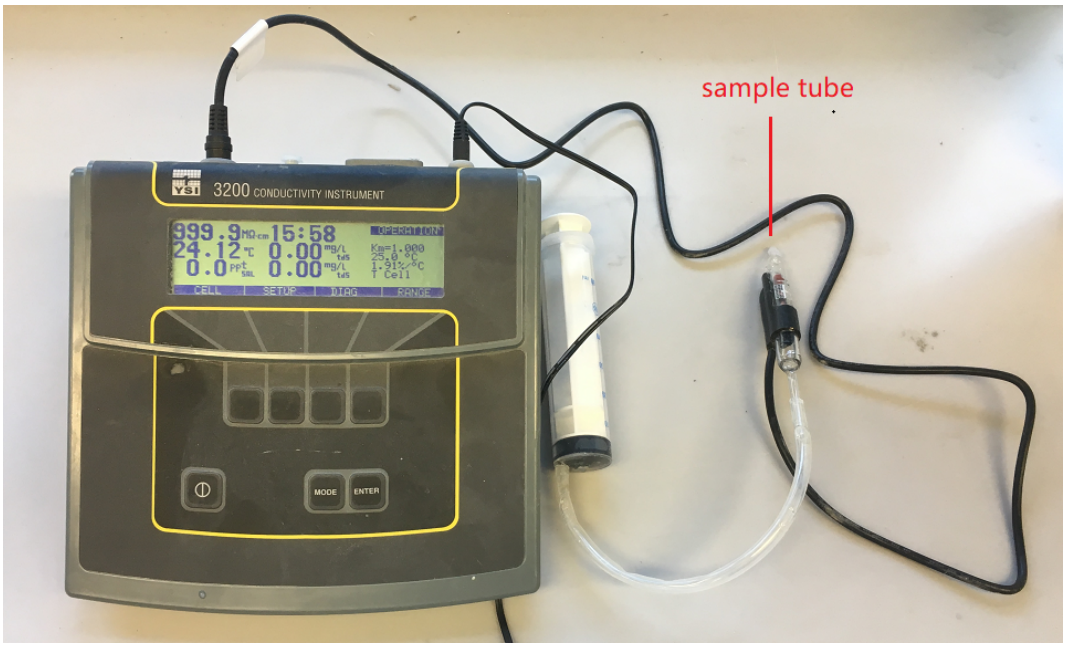

Figure 4.15: Photo of the *YSI 3200 conductivity instrument* and the sample tube.

The test results of tap water and $NaCl$ solution different sources are shown in Table 4.4. It can be seen that the test results of the self-made system are very close to the results of *YSI 3200 conductivity meter*. For $11460ppm\ NaCl$ solution, if considering the resistivity in *Schulum-*

Table 4.4: Resistivity of tap water and $NaCl$ solution from different sources.

	Sources		
Samples	*Schulumberger chart*	YSI 3200	Self-made System
Tap water (Ωm)	-	75	85
11460 ppm $NaCl$ (Ωm)	0.58	0.50	0.54

berger chart as the reference value, the self-made system is even more accurate than the *YSI 3200 conductivity instrument*. So far, the self-made system can be primarily considered qualified for resistivity test. However, both tap water and 11460ppm $NaCl$ solution are liquid and have relatively low resistivity, which are different from frozen soil. Therefore, further verification for the results needs to be made.

The resistivity of frozen *Halden Silt* has not been reported yet, but the resistivity of some other silt has already been measured by some researchers. Figure 4.16(a) shows the results of ground surveys conducted by Hoekstra et al. (1975) in Fairbanks, Alaska, USA. It can be seen that the resistivity of *Fairbanks Silt* is approximately 3000Ωm at -10°C and 900Ωm at -5°C. Zhou et al. (2015) reported the results of the resistivity of five different soils from laboratory tests, as shown in Figure 4.16(b). The test setup used by Zhou et al. (2015) is a four electrodes system as similar to the one used by the current writer. According to Figure 4.16(b), the resistivity of silt loam (red curve) is around 1800 Ωm at -10°C and 1000Ωm at -5°C. For frozen sand soil, the resistivity is over two orders of magnitude higher than frozen silt.

By using the self-made testing instrument, we measured the resistivity of saturated *Halden Silt*. The resistivity was measured at two temperatures -5°C,-10°C, before the measurement the sample had been put in that temperature for more than 24 hours. The temperatures in the freezer were -5.3 and -10.8°C when measuring, and the results and comparison are shown in Table 4.5. The measurements of the self-made system are also plotted in Figure 4.16 as red dots. Considering the following points, the self-made system measurements, which are between the results of silt and sand gravel in the literature, are quite acceptable.

1. The results of Hoekstra et al. (1975) were from a field test, and Zhou et al. (2015) used a square sample holder who may have different geometry effect;

2. Zhou et al. (2015) used 50Hz AC, and the self-made system is using 10Hz which is supposed

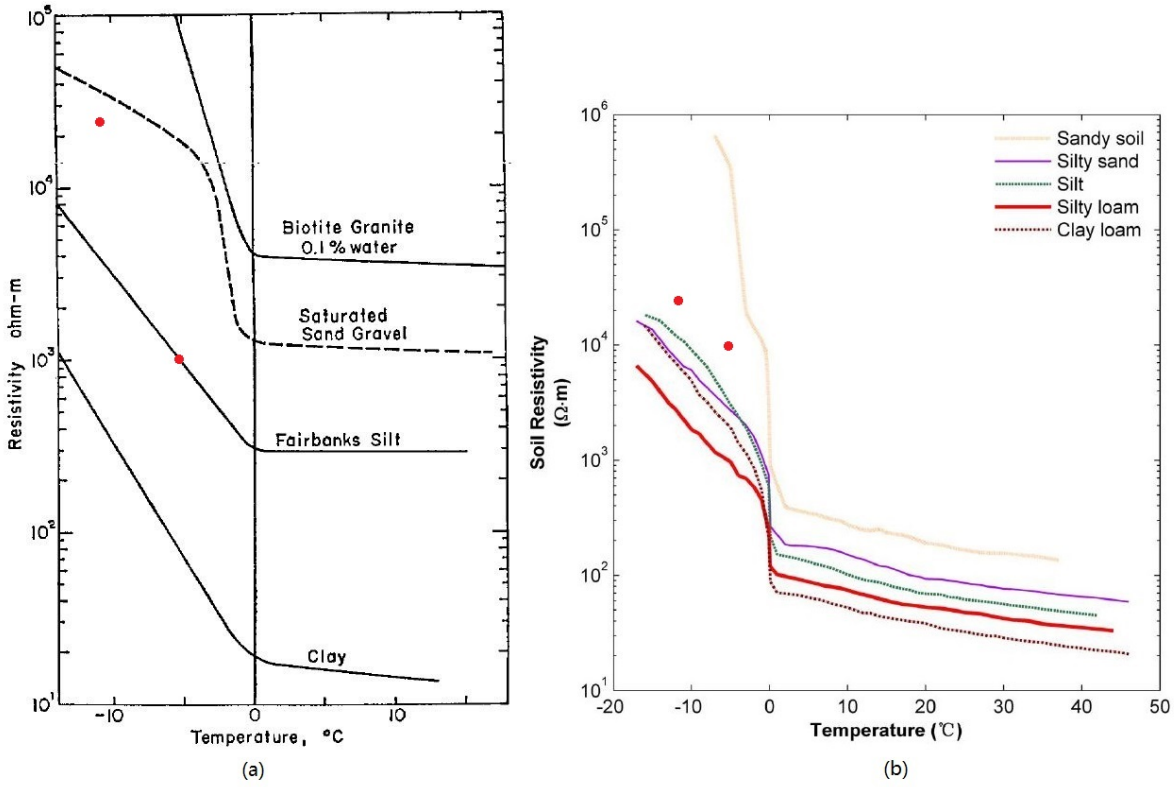

Figure 4.16: (a) The resistivity of several saturated soil types and one rock type as a function of temperature (Hoekstra et al., 1975); (b) Effect of soil temperature on the electrical resistivity of the five soils (Zhou et al., 2015). The resistivity measurements of the self-made system on *Halden Silt* at -5.3°C and -10.8°C are plotted as red dots.

to get higher effective resistivity;

3. The silt samples are different, also, even though the *Halden Silt* we used was in *Unit II*, but it is located at the boundary of *Unit I* and *Unit II*; since *Unit I* is almost sand which has around two orders of magnitude higher resistivity than silt, the resistivity of our *Halden Silt* sample could be higher than the normal silt.

The results of the self-made system match the results of conductivity meter and the literature quite well with tap water and $NaCl$ solution. Also, the results of the frozen silt sample are acceptable comparing to the literature. Therefore, the resistivity measured by the self-made

Table 4.5: Resistivity of silt from different sources at different temperatures.

Temperatures	Sources			
	Fairbanks Silt (Hoekstra et al., 1975)	Silt loam (50Hz) (Zhou et al., 2015)	Sand soil (50Hz) (Zhou et al., 2015)	*Halden Silt* (10Hz) (Self-made System)
-5°C	900	1000	appx. 9×10^5	9715 (-5.3°C)
-10°C	3000	1800	over 10^6	24124(-10.8°C)

system can be considered valid.

4.4 Acoustic Measurement System

A seismic wave is widely used in the geophysics tests. The differences in the properties of the soil are reflected on the measured velocity of the wave propagation. On the other hand, the nondestructive and low-cost acoustic method is more suitable for laboratory soil tests.

The self-made acoustic measurement system needs to be calibrated to eliminate electromagnetic noise. Therefore, some signal processing techniques are used in data processing. The calculated p-wave velocity is verified with the materials with known acoustic properties.

4.4.1 Acoustic Data Processing

The *LabVIEW* program used to control the acoustic system is shown in Figure B.2 and B.3. The small block at the top and the bottom control the signal recording and generating, respectively. The transmitting signal is one single sinus wave at the frequency of $100kHz$. By considering the capacity of the computer and the data logger, the sampling rate is set at $1MHz$.

The sequence block in the middle processes the recorded data. First, the data is filtered by a filter which only allows the signal between 200 to $200kHz$ pass. This range excludes the common noise in the laboratory, such as a fluorescent lamp (50Hz). Then, the signals exceed the trigger level are saved. The continuously recorded data will be cut into smaller pieces, and every piece includes a transmitting signal. The program can locate the zero-crossing of the transmitting signal. Afterwards, the signals will be auto-scaled, which makes it easier to observe.

By using the zero-crossing as the original, the "stacking" method can be applied. As shown in Figure 4.17, by summing multiple measurements, the coherent signal will be enhanced, and the incoherent signal will be offset. If the number of times of stacking was large enough, the incoherent noise could be almost fully eliminated. Here the number of times of stacking is set at 200, which is limited by the capacity of the computer.

Figure 4.18 shows the effect of 200 times stacking on the measured wave. It can be easily ob-

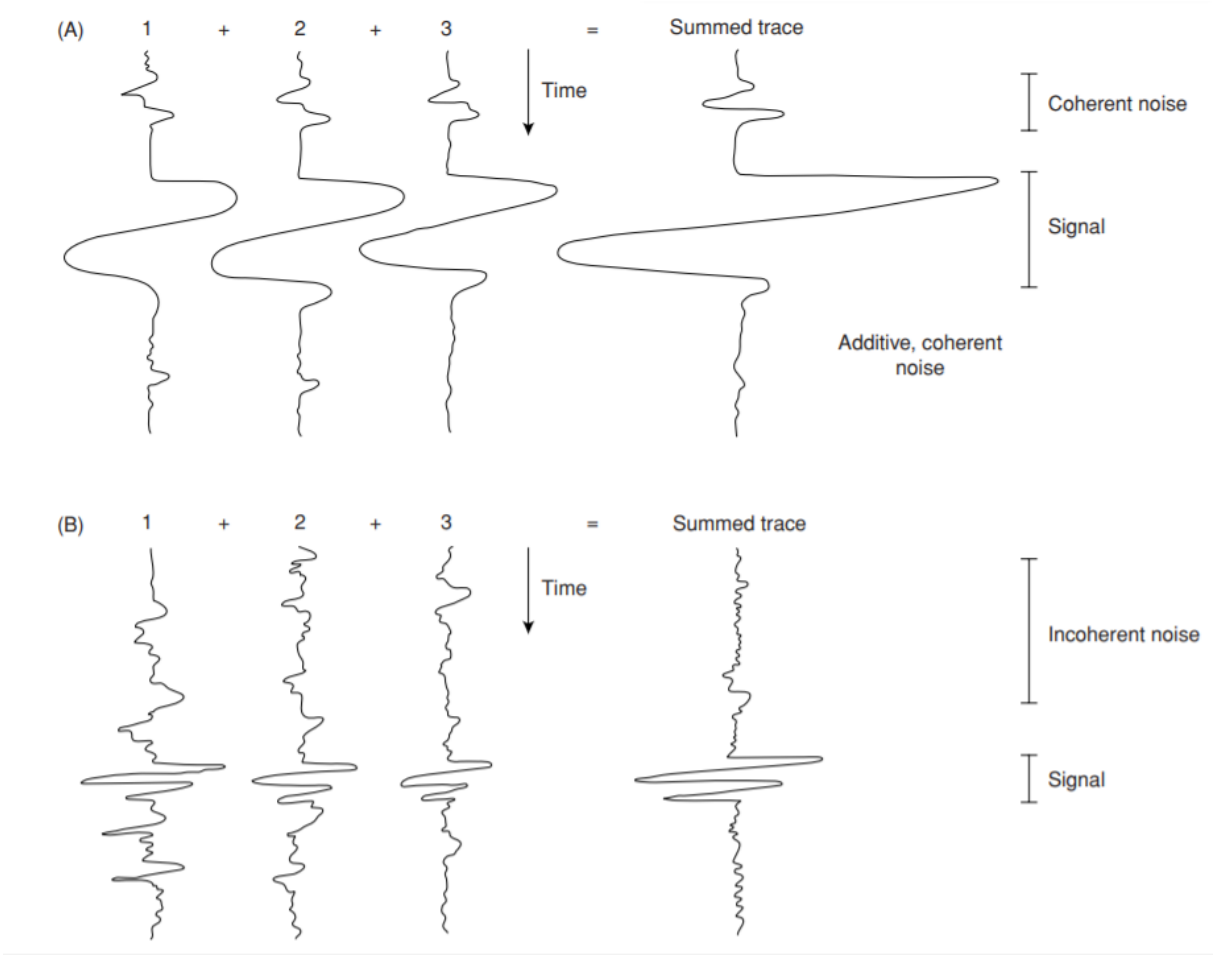

Figure 4.17: The effect of summing three traces with (A) coherent and (B) incoherent noise. (Reynolds, 2011)

served that the incoherent noise before the transmitted wave is eliminated. Meanwhile, the coherent noise from the electromagnetic noise caused by the data logger remains, but the curve becomes more smooth because the incoherent noise is gone. The most important thing is that, by using the stacking method, the first arrival wave can be correctly determined, which gives more accurate travel time of the p-wave. Here is a part of the program is written for auto-calculate the travel time. Since the noise is not fully eliminated, it is hard to locate the first arrival wave by a fixed threshold. Therefore, the first arrival wave is recognized by eye in this thesis; the standard of the determination is explained in the later section.

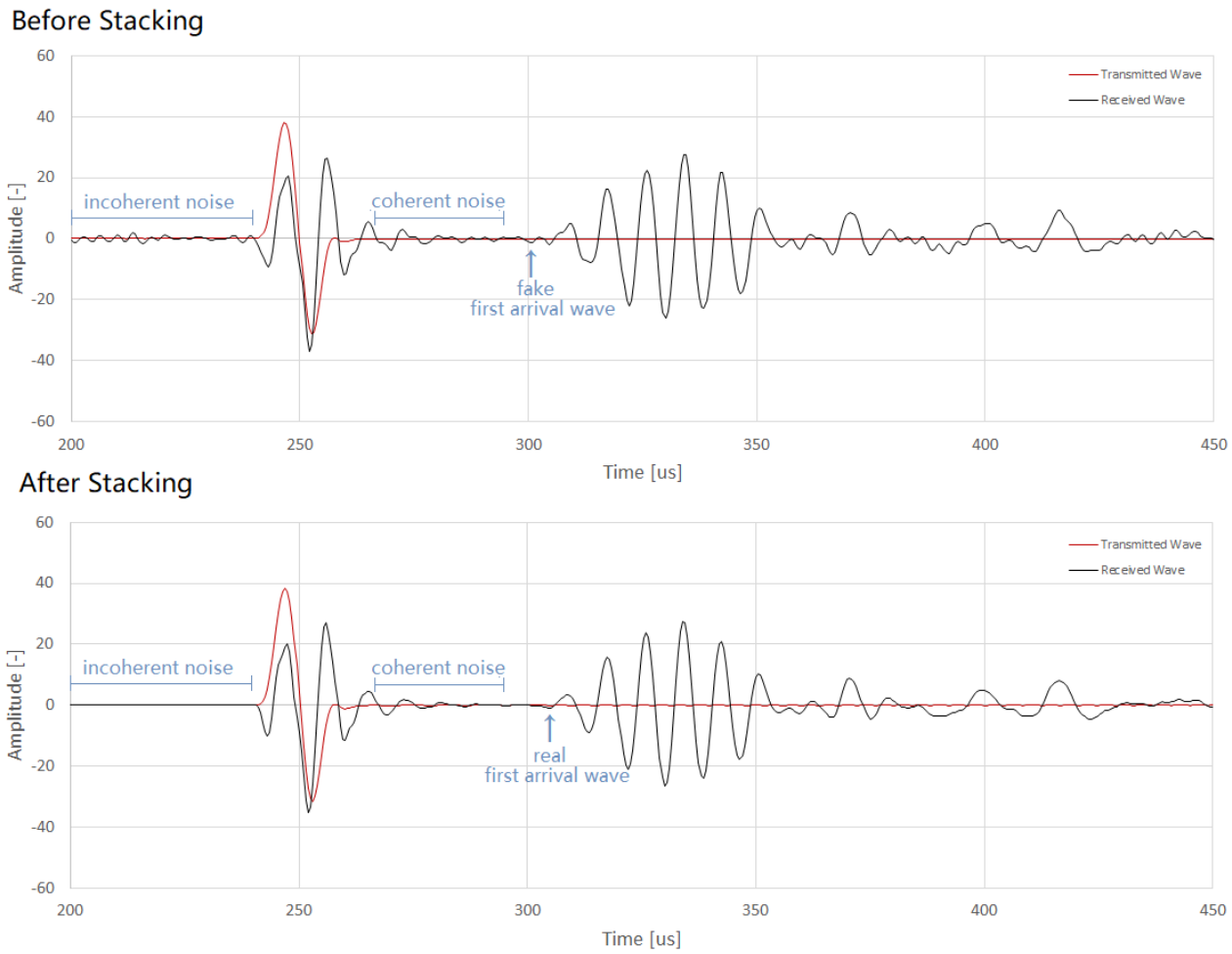

Figure 4.18: The effect of stacking on the measured waves in frozen silt.

4.4.2 Calibration

To calibrate the acoustic measurement system, the velocity of p-wave propagation in aluminium, water and ice were measured and compared with the previous researches.

First, the p-wave velocity was measured in solid. As shown in Figure 4.19, these three rods are made of the same material, *Aluminum 6082 T6*. They have the same diameter of $10cm$ but different length at $15cm$, $20cm$ and $25\ cm$, respectively. The piezo pads were attached to the two ends of the rods with silicone oil (*111 Compound* manufactured by *Dow MOLYKOTE*^{TM}). The tests results are shown in Figure B.7, B.8 and B.11 in Appendix B. The calculation results are shown in Table 4.6

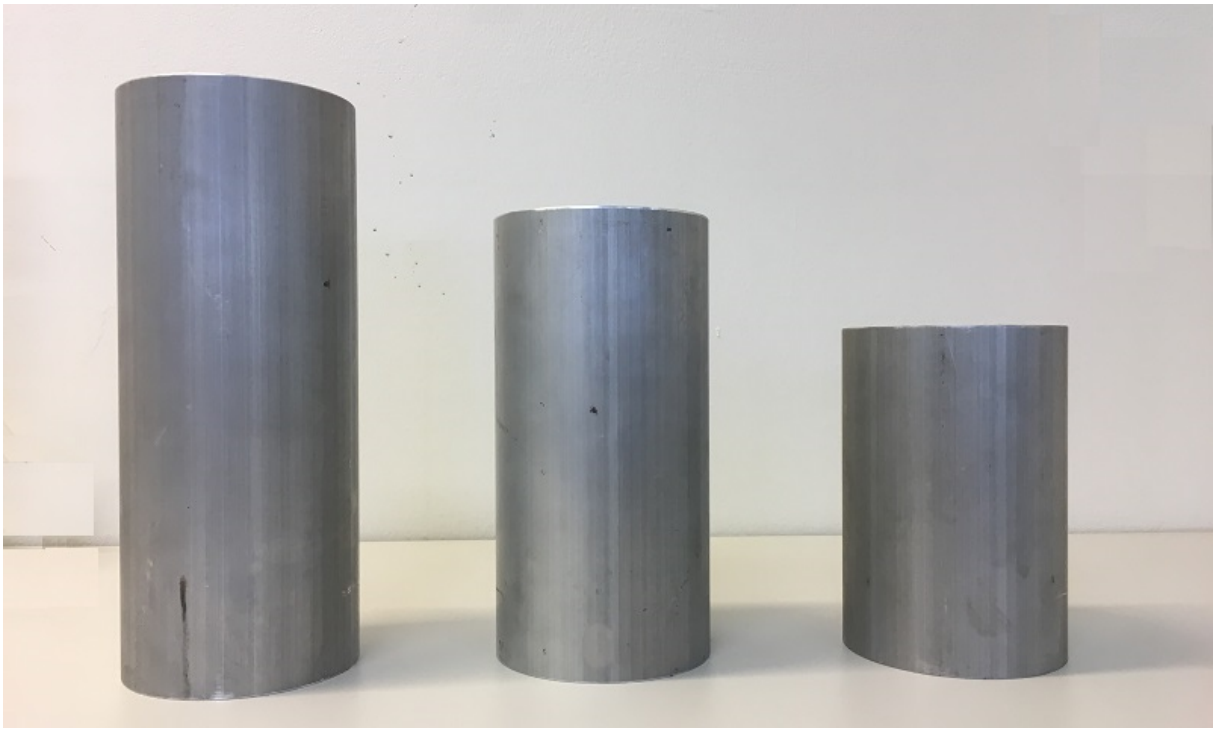

Figure 4.19: The 10cm diameter *Aluminum 6082 T6* rods (from left to right: $15cm$, $20cm$, $25cm$) used for the calibration of acoustic measurement system.

According to *NDT (Nondestructive Testing) Resource Center*, aluminium and its alloys gener-

Table 4.6: The p-wave velocity in aluminum rods.

Length (cm)	15	20	25
Travel Time (μs)	26	34	41
Velocity (m/s)	5769	5882	6098
Difference to the reference ($6207 m/s$)	-7%	-5%	-2%

ally have p-wave velocity range from 6300 to $6500 m/s$. Ginzel and Turnbull (2016) reported the p-wave velocity of *Aluminum 6061* is $6207 m/s$ and it slightly fluctuated with frequency. Comparing to *Aluminum 6082 T6*, which is used in the current calibration tests, the elongation at break of *Aluminum 6061* is slightly smaller. Except for this, these two aluminium alloys have almost the same mechanical properties. Thus, it is believed that *Aluminum 6082 T6* has the same p-wave velocity as *Aluminum 6061*. Therefore, the results shown in Table 4.6 are quite accurate, especially the result of $25cm$. It also can be noticed that the velocity increases with the ascending length and getting close to the reference velocity. This might because of that the electromagnetic noise (as circled by the blue line in Figure B.7) has overlap with the received signal, which might influence the determination of the first arrival. As the length of the rod increas-

ing, these two signals will not interfere with each other, which leads to a more accurate result. The electromagnetic noise is believed from the data logger, and it can be reduced by connecting the data logger to both the ground and the sample. Besides, the silicone oil at the contact area between the piezo pads and the aluminium rods could also weaken both the sent and received signals which makes it harder to determine the first arrival.

The p-wave velocity was also measured in liquid. To measure the acoustic velocity in wa-

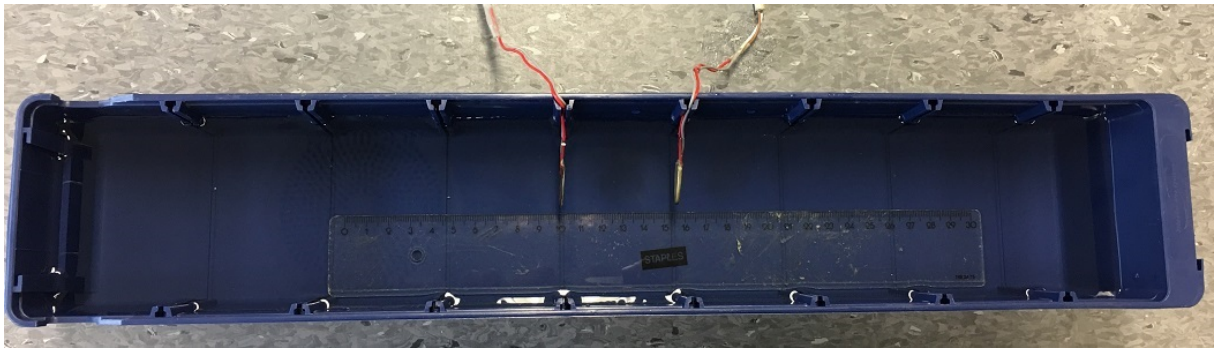

Figure 4.20: The water tank for the calibration of acoustic measurement system.

ter, the piezo pads were placed in a water tank (length 59cm, width 8.5cm, depth 7.5cm) as shown in Figure 4.20. The velocities were measured at different separations (5.3cm, 10.8cm, and 16.3cm). The results are shown in Figure B.9, B.10 and B.6 in Appendix B, respectively. The electromagnetic noise mentioned previously still exist, but they are not displayed in the figures for a aesthetic purpose. As shown in Figure B.9, **the trough before the first peak is chosen as the first arrival**. Thus, the travel time is the time difference between the first arrival and the 0 amplitude of the sent sinus wave (250μs). Therefore, the velocity is calculated and shown in Table 4.7. According to Bilaniuk and Wong (1993), the sound speed in pure water is 1482m/s at 20°C. The differences are all below 5% as shown in Table 4.7, which are very accurate.

The p-wave velocity is also measured in ice with 16cm separations between the two piezo pads.

Table 4.7: The p-wave velocity in water.

Separation (cm)	5.3	10.8	16.3
Travel Time (μs)	34	70	106
Velocity (m/s)	1558	1543	1538
Difference to the reference (1482m/s)	+5%	+4%	+4%

To make the ice sample, the tube sample holder (8.9cm inner diameter and 21cm height) was filled with water and had placed in the freezer at -20°C for 16 hours. According to the result shown in Figure B.12 in Appendix B, the velocity is calculated and it equals to 3809m/s. Vogt et al. (2008) reported the p-wave velocity of bubble-free ice is range from 3840 to 3894m/s at the temperature from 0 to -20°C. Since the ice made in the current calibration test is not bubble-free, the p-wave velocity is supposed to be lower than the reference values. Therefore, 3809m/s is a quite accurate measurement for ice.

Since the p-wave velocities measured in aluminium, water and ice all match the reference values quite well, the measurement of the self-made acoustic system can be considered valid.

4.5 Testing Procedure

To minimize the influence of the inhomogeneity of the intact silt sample, the reconstituted sample is used in the tests. To prepare the reconstituted sample with certain salinity, the silt sample shown in Figure 4.21 is cut into small pieces and put into the steel bowl of the stand mixer. Then, the sample is fully mixed with a certain amount of $NaCl$ solution at a certain concentration. The mixture should be placed on a table for 12 hours until the silt precipitated at the bottom of the container. Then, take the relatively clear upper solution into a funnel with filter paper, then the salinity of the pore fluid can be measured by using *YSI 3200 conductivity instrument* to measure the filtrate. To obtain saturated silt sample, the precipitated silt at the bottom was taken and put into the sample holder. 3kg weight was put on the sample to consolidate it. A sieve was placed at the bottom of the sample holder to allow the water to drain. After 24 hours, the saturated silt sample was ready. Take some consolidated saturated silt sample out and weight it. Then put it into the oven and dry it at 110°C for two days. In the end, weight it again, and the water content can be calculated. Since the silt is saturated, the porosity is also determined.

After the sample is ready, the electrodes and the piezo pads need to be installed to the sample holder. The piezo pad is placed between the soil sample and the potential electrode (steel mesh). The data logger (acoustic), the amplifier (acoustic) and the soil sample should be series connected to minimize the electromagnetic noise. Therefore, the pin at the tip of the ground

Figure 4.21: Photo of the silt sample.

wire is inserted into the soil sample about $3cm$ depth, as shown in Figure 4.4. Then the wires on the sample holder should be connected to the corresponding port on the data logger. The temperature sensor is attached to the outer side of the tube. In the end, the sample holder is placed vertically into the freezer (*WAECO Coolbox T0162 FDH/MT/G* manufactured by *euroengel*, $Length \times Width \times Height = 110 \times 79 \times 65cm$), the temperature can be set in the range from -24°C to +40°C. Weight should be placed on top of the tube, in case of the volume expansion during the freezing break through the adhesive between the sample tube and the bottom plate.

The joint measurement is taken at three different temperature below 0°. First, the freezer is set at -3°C and the measurement is taken after 24 hours. Then, set the temperature at -5°C and measure after 12 hours. Finally, set the temperature at -10°C and measure after 12 hours. The same procedure is repeated on two samples with different salinity.

Chapter 5

Test Results and Discussions

In this chapter, the results obtained by following the test procedure mentioned previously will be discussed. The validation of the measurements of the self-made system will be verified by comparing to measurements in previous researches. Also, the measurements will be verified theoretically by comparing to the *Hashin-Shtrikman (HS) bounds*. The potential of a joint method will be discussed by comparing the estimated unfrozen water saturation from individual electrical and acoustic models.

As shown in Table 4.2, the *Halden Silt* sample is mainly composed by quartz (41%), plagioclase (30%) and feldspar (12%). For simplification the physical properties of the solid phase is using the weighted arithmetic mean of these three main constituents (based on the parameters shown in Figure 3.1). The parameters used for calculations are shown in Table 5.1.

Table 5.1: Physical properties of the three phases of the frozen silt according to the assumption.

Phase	K [GPa]	G [GPa]	ρ $[kg/m^3]$
Solid	51.2	33.3	2638
Water	2.2	0.0	1000
Ice	8.4	3.7	920

5.1 Test Results

Two sets of experiments were conducted with different salinity. The silt samples were mixed with $10g/L$ and $30g/L$ $NaCl$ solution, respectively. However, due to the salinity and the water content of the silt sample, the salinity of the mixture need to be measured. The measurement

method of the pore water salinity is mentioned in Chapter 4. According to the temperature and resistivity measurements of the *YSI3200 conductivity instrument*, the salinity of the pore water at 20°C can be calculated by the equations (Arps et al., 1953) below.

$$\rho_{T_2} = \rho_{T_1} \frac{T_1 + 21.5}{T_2 + 21.5} \tag{5.1}$$

$$\rho = 0.0123 + \frac{3627.5}{C^{0.955}} \tag{5.2}$$

Where ρ is the measured resistivity (Ωm, C is the pore water salinity (ppm), and T is the temperature in °C.

The results are shown in Table 5.2. It can be seen that the pore water salinity is lower than the solution added because of the water content in the silt. The weights of the wet and the dry

Table 5.2: The salinity of the pore water.

Set	Solution Added [ppm]	Resistivity [$\Omega \cdot cm$]	Temperature [°C]	Salinity Calculated (at 20°C) [ppm]
A	10000	64.96	23.39	7868
B	30000	30.94	19.65	19199

reconstituted samples of both sets were measured and recorded before and after drying in the oven. Since the sample is saturated and assuming the silt sample is composed of quartz, the volumetric porosity and density can be calculated using the parameters in Table 5.1. The results are shown in Table 5.3.

Table 5.3: The porosity and density of the silt samples.

Set	Total Weight (wet) [g]	Total Weight (dry) [g]	Container Weight [g]	Volumetric Porosity [%]	Density [kg/m^3]
A	93.2	80.6	45.7	49.36	1861
B	139.0	113.9	50.2	51.55	1824

The joint measurements were conducted at three different temperatures for both sets of tests. The actual temperature in the freezer is different from the set temperature displays on the freezer's screen. The temperatures measured are fluctuating in a quite large range (see Figure B.13 and B.14), due to the temperature sensor was placed outside the sample. However, since the temperature sensor is close to the sample, the average temperature can be considered as the actual temperature in the samples. The results are shown in Figure B.13 and B.14, also,

it has been summarized as shown in Table 5.4. For the electrical test, using 10Ω fixed resistor

Table 5.4: The average of the actual temperatures of each test.

Set Temperature		-2.5°C	-5°C	-10°C
Actual Temperature of Set A	[°C]	-4.5	-7.8	-13.4
Actual Temperature of Set B	[°C]	-3.3	-6.5	-11.9

on the amplifier, level 2 amplitude and $10Hz$ frequency, the resistivity can be read on the front panel of the *LabVIEW* program. For the acoustic test, using $100kHz$ transmitting frequency and $1MHz$ receiving frequency, the transmitted and received signals will be recorded. Filtering the data with $200Hz$ lower cut and $200kHz$ upper cut value and processing the data with 200 times stacking, the travel time can be read from Figure B.15, B.16, B.17, B.18, B.19 and B.20 in Appendix B. The height of the silt sample grows with the decreasing of temperature, therefore, the separation of the piezo pads also changes. The heights were measured at each temperature. The acoustic test results and the calculated p-wave velocity are shown in Table 5.5.

Table 5.5: The average of the actual temperatures of each test.

Set	Temperature [°C]	Separation [cm]	Travel Time [μs]	P-wave Velocity [m/s]
A	-4.5	18.6	89	2090
	-7.8	19.1	57	3351
	-13.4	19.2	50	3840
B	-3.3	18.8	100	1880
	-6.5	19.0	60	3167
	-11.9	19.1	50	3820

The summary of the measured and calculated results of the joint measurements are shown in Table 5.6.

Table 5.6: The summary of the joint measurement results at different temperature with different salinity.

	General Parameter				Joint Measurements	
Set	Saline Resistivity [Ωm]	Porosity [%]	Density [kg/m^3]	Temperature [°C]	Electrical Resistivity [Ωm]	P-wave Velocity [m/s]
A	0.6496	49.36	1861	-4.5	16.64	2090
				-7.8	94.70	3351
				-13.4	268.20	3840
B	0.3094	51.55	1824	-3.3	6.61	1880
				-6.5	19.30	3167
				-11.9	47.68	3820

To verify the measurements of our self-made system, we compare the results with the previous joint measurement, for example, the measurements of *Alaska Silt* by Hoyer et al. (1975).

In Figure 5.1 (a), it can be seen that the frozen silt with lower salinity has larger resistivity than that with higher salinity. This is mainly because that the saline with higher concentration has lower electrical resistivity and the electrical current travels through the interconnected channels filled with saline. Besides, the freezing point depression caused by salinity allows more unfrozen water to exist at the same temperature. In Figure 5.1 (b), the frozen silt with lower salinity has higher p-wave velocity than that with lower salinity at the same temperature below the freezing point. It is because the salinity depresses the freezing point, which results in higher unfrozen water content at the same temperature. The existence of water, instead of ice, causes lower elastic modulus, which leads to lower p-wave velocity.

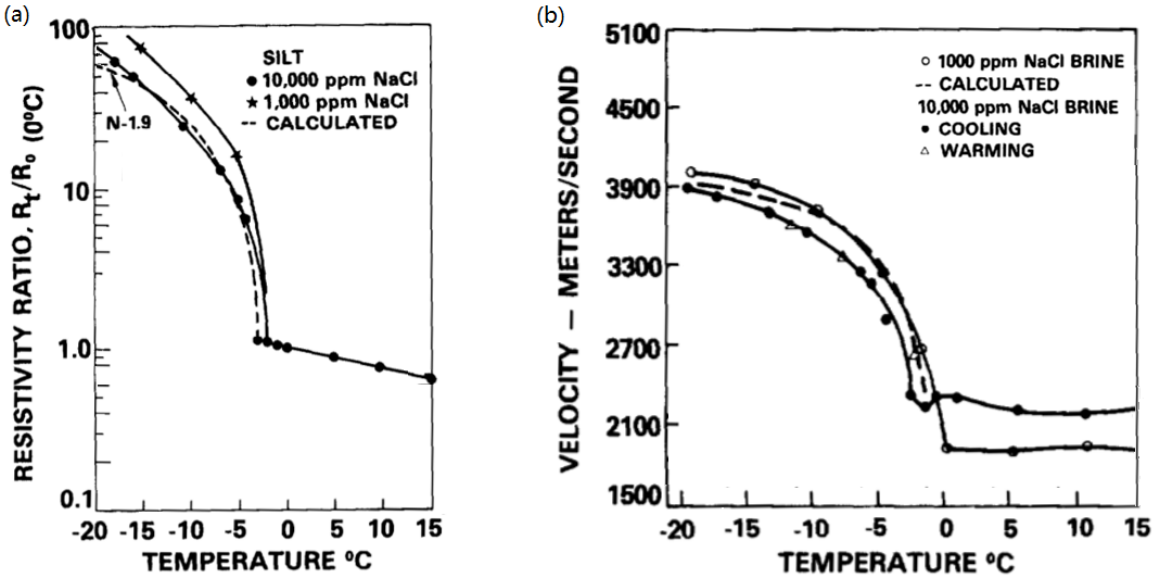

Figure 5.1: The (a) electrical resistivity and (b) p-wave velocity versus the corresponding temperatures according to the measurements of *Alaska Silt*. (Hoyer et al., 1975, reproduced with reversal x-axis)

Plot the joint measurements as a function of temperatures; the results are shown in Figure 5.2. As it can be seen in Figure 5.2, the results of both electrical and acoustic measurements have the similar pattern and the variation with the similar orders of magnitude as that shown in Figure 5.1. As shown in Figure 5.2 (a), the resistivity increases dramatically with the descending temperature. It can also be noticed that the resistivity of *set A* is higher than that of *set B* at similar temperatures. This observation reflects that the pore fluid salinity dominates the total resistiv-

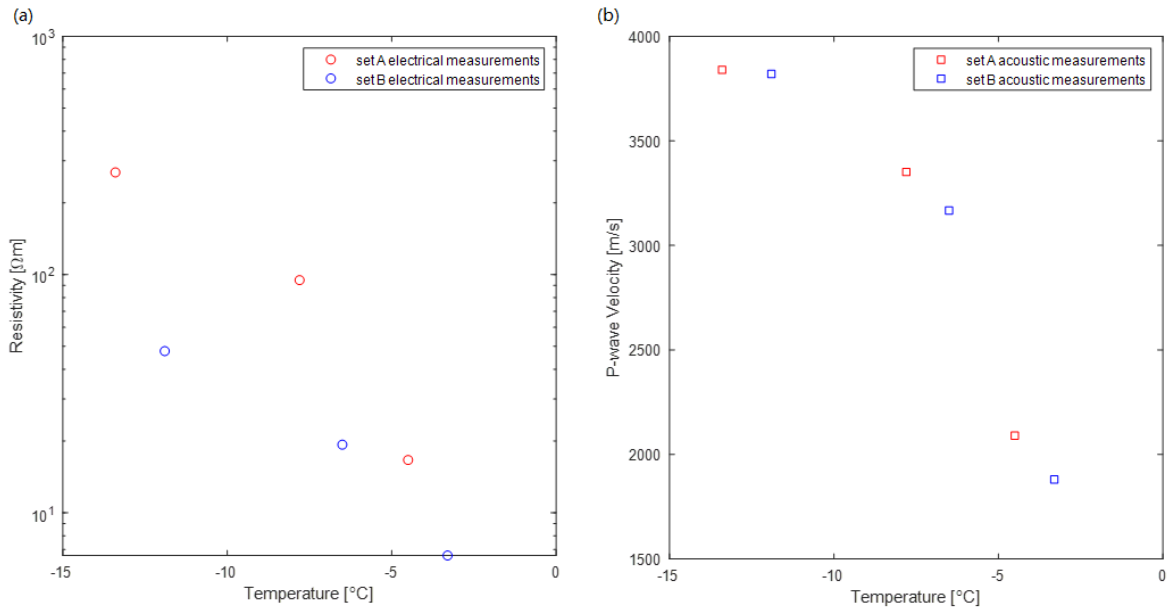

Figure 5.2: The (a) electrical resistivity and (b) p-wave velocity versus the corresponding temperatures according to the measurements of *Halden Silt*.

ity, which also implies that the pore fluid is interconnected in the frozen sample. As shown in Figure 5.2 (b), the p-wave velocity also increases with the descending temperatures. Theoretically, if the two sets of samples are completely identical except for the pore fluid salinity, *set A* is supposed to have a higher p-wave velocity at the same temperature below the freezing point. However, in this case, the temperatures at measuring of the two sets of tests are not identical, and the samples are inhomogeneous even though they are prepared in the same way. Besides, the measurements of different sets are quite close; no further comparison is made here.

Since Hoyer et al. (1975) used the resistivity ratio instead of resistivity to describe the electrical conductivity, the results cannot be directly compared. Therefore, we found another reference (King et al., 1982) which reported the joint measurements of *Mackenzie River GSC3 Silt*. Using the *Shape-preserving Interpolant* function in the *Curve Fitting Tool* in *MATLAB* to fit the measurements of *GSC3 Silt* and the measurements shown in Figure 5.2, the results are plotted in Figure 5.3.

In Figure 5.3, it can be observed more directly that the results of both electrical and acoustic measurements have a similar pattern and the variation with the similar orders of magnitude.

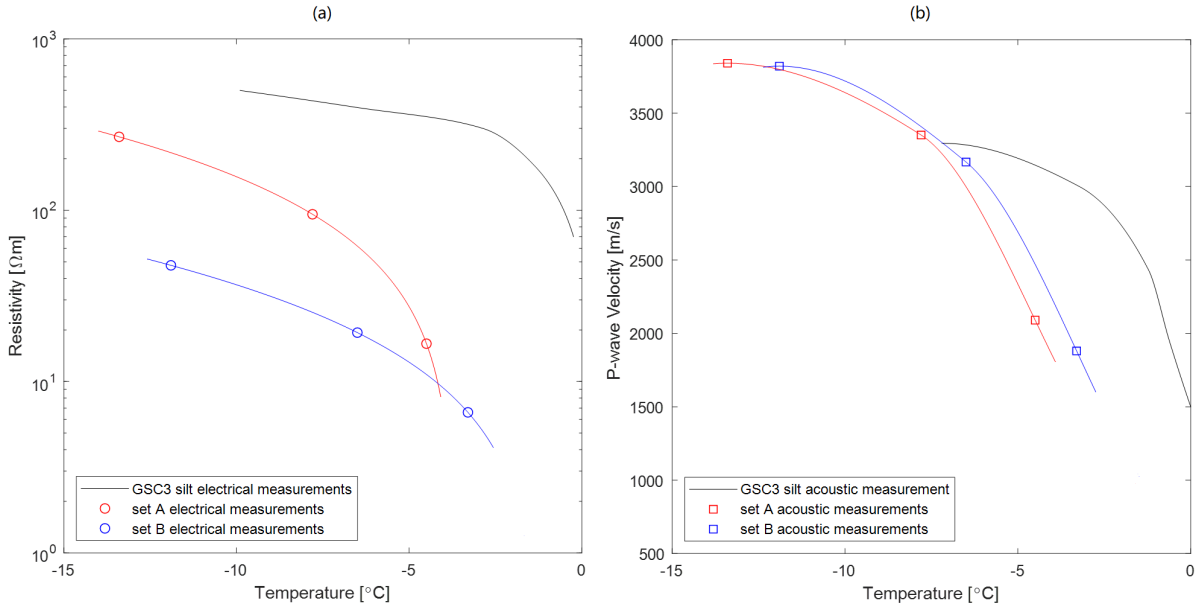

Figure 5.3: The (a) electrical resistivity and (b) p-wave velocity measurements of *Halden Silt* compares to the measurements of *Mackenzie River GSC3 Silt* by King et al. (1982)

Since *GSC3 Silt* is onshore silt with relatively low salinity, the higher resistivity of *GSC3 Silt* shown in Figure 5.3 (a) might be due to the relatively lower pore water salinity. Also, the lower porosity of *GSC3 Silt* (36%) might also cause the higher resistivity. Meanwhile, in Figure 5.3 (b), the higher velocity of *GSC3 Silt* at warmer temperature might be because of the unfrozen water content drops faster for the lower salinity soil during the freezing.

Comparing to more individual electrical measurements (Hoekstra et al., 1975, Zhou et al., 2015) and acoustic measurements (Nakano et al., 1972, Wang et al., 2006 and Christ et al., 2009), the results of *Halden Silt* acquired from our self-made joint measurement system are quite reasonable in terms of its soil classification.

5.2 Theoretical Analysis

For either the effective electrical conductivity or the effective elastic modulus of a mixture of grains and pores, if we want to make a theoretical prediction of it, we generally need to specify:

1. the volume fractions of the various phases;

2. the electrical conductivity or the elastic modulus of the various phases;

3. the geometric details of how the phases are arranged relative to each other.

If we specify only the volume fractions and the properties of the constituents, the best we can do is to predict the upper and lower bounds (Mavko et al., 2009). Additionally, if the assumption of the geometric details has been made in a model, an estimation of the effective properties of the mixture can be made based on this assumption.

5.2.1 Hashin-Shtrikman Bounds

The bounds described in this section apply under the conditions that each constituent is isotropic, linear, and elastic. The calculated upper and lower bounds can be used to generally verify the measurements of the self-made system.

Electrical Bounds

The Hashin-Shtrikman (HS) bounds (Hashin and Shtrikman, 1962) are effective conductivity bounds that give the narrowest possible bounds without defining the geometry between components of a two-phase medium. The assumption is that all the components within the medium are isotropic and homogeneous. The upper (conductive) bound represents the fluid component is completely interconnected, and the solid component is completely isolated, which indicates the maximum conductivity of the composite. The lower (resistive) bound represents the opposite. The expression of the bounds are:

$$\frac{1}{\rho_{HS,conductive}} = \sigma_{HS,conductive} = \sigma_f + (1-\beta)\left(\frac{1}{\sigma_s - \sigma_f} + \frac{\beta}{3\sigma_f}\right)^{-1} \tag{5.3}$$

$$\frac{1}{\rho_{HS,resistive}} = \sigma_{HS,resistive} = \sigma_s + \beta\left(\frac{1}{\sigma_f - \sigma_s} + \frac{1-\beta}{3\sigma_s}\right)^{-1} \tag{5.4}$$

where $\sigma_{HS,conductive}$ and $\rho_{HS,conductive}$ are the upper or conductive HS bound of effective conductivity and resistivity, respectively;

and $\sigma_{HS,resistive}$ and $\rho_{HS,resistive}$ are the lower or resistive HS bound of effective conductivity and resistivity, respectively;

σ_s and ρ_s are the conductivity and resistivity of the solid, respectively;

σ_f and ρ_f are the conductivity and resistivity of the fluid, respectively;

β is the volumetric fraction of the fluid, which can be calculated as:

$$\beta = \phi * S_w \tag{5.5}$$

The saturated frozen soil is a three-phase system. However, considering the resistivity of ice and solid is way higher than the pore saline, the system can be simplified as a two-phase system by assuming the ice and the solid have the same high resistivity. The resistivity of ice and solid are assumed as $100 k\Omega m$ during the calculation.

Acoustic Bounds

Hashin and Shtrikman (1963) calculated bulk and shear modulus in terms of upper and lower bounds. Also, it assumes that both the medium and each of the constituents are isotropic and elastic. The physical interpretation of the HS method for a two-phase material is shown in Figure 5.4. The effective medium is comprised of a space filled with spheres. Each sphere is comprised of a core of component one with a shell of component two. The volume fraction of each component in every sphere is identical with the total volume fraction of that component in the medium. If the material with the higher modulus forms the shell of the sphere, the effective modulus will be that of the upper bound. The lower bound is produced when, the stiffer material forms the core of the sphere.

For multiple-phase materials, the HS method is presenting as the following equations without further assumptions of the geometric relationships between each component. The bulk modulus is given by:

$$K_{lower} = K_s + \frac{A_s}{1 + \alpha_s A_s} \tag{5.6}$$

$$K_{upper} = K_n + \frac{A_n}{1 + \alpha_n A_n} \tag{5.7}$$

Where,

$$\alpha_s = -\frac{3}{3K_s + 4G_s} \tag{5.8}$$

$$\alpha_n = -\frac{3}{3K_n + 4G_n} \tag{5.9}$$

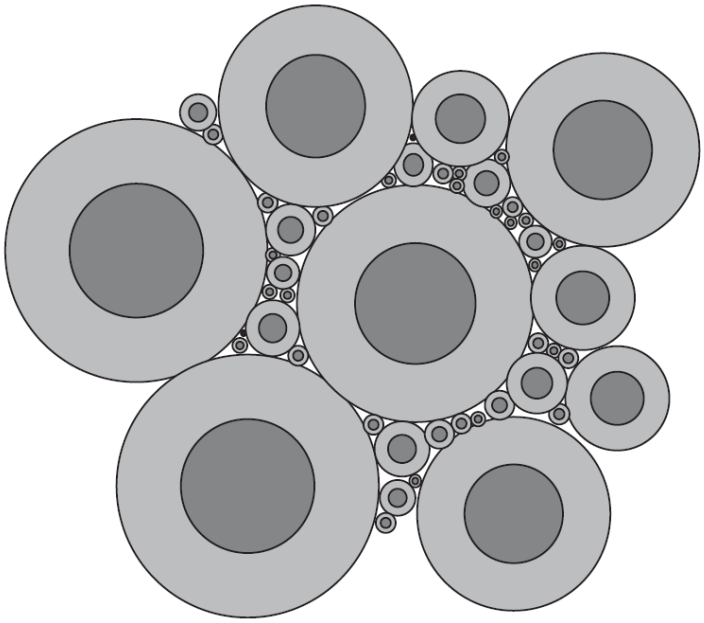

Figure 5.4: Physical interpretation of the Hashin–Shtrikman bounds for the bulk modulus of a two-phase material. (Mavko et al., 2009)

$$A_s = \sum_{r=2}^{r=n} \frac{v_r}{\frac{1}{K_r - K_s} - \alpha_s} \tag{5.10}$$

$$A_n = \sum_{r=1}^{r=n-1} \frac{v_r}{\frac{1}{K_r - K_n} - \alpha_n} \tag{5.11}$$

Where the subscript s, n and r denote the smallest modulus, largest modulus and the modulus of the r-th component, respectively.

For vanishingly small G_0, shear modulus is given by:

$$\frac{1}{G_{lower}} = \sum_{r=1}^{r=n} = \frac{v_r}{G_r} \tag{5.12}$$

$$G_{upper} = \sum_{r=1}^{r=n} = G_r v_r \tag{5.13}$$

Where v_r is the volumetric content of the r-th component. For the saturated frozen soil consisting of unfrozen pore fluid, ice and soil, the volumetric content of each component can be presented as:

$$v_f = \phi S_w; \qquad v_i = \phi(1 - S_w); \qquad v_s = 1 - \phi \tag{5.14}$$

Where the subscripts f, i and s denote unfrozen pore fluid, ice and soil, respectively.

5.2.2 Individual Models

By assuming different certain geometric structures, the individual electrical and acoustic models can be used to estimate the unfrozen water.

Electrical Model

Archie's law is suggested by many researchers (Daniels et al., 1976, King et al., 1988) for estimating the unfrozen water content. If the unfrozen water saturation, S_w, (the fraction of water remaining unfrozen at subzero temperatures) is less than 1.00, the expression of Archie's law is presented as below (Keller, 1971).

$$\rho_\alpha = a(\rho_w)_\alpha \phi^{-m} S_w^{-n}; \qquad \alpha = i, f \tag{5.15}$$

where ρ_α is the resistivity of soil, and i and f represent the unfrozen and frozen state, respectively; ρ_w is the water resistivity in the pore space; a, m and n are empirical constants; ϕ is the porosity.

Daniels et al. (1976) made an assumption to use Archie's law in porous medium: the fraction of water remaining unfrozen at subzero temperatures equals to the ratio of the resistivity of the solution before and after freezing.

$$(\rho_w)_f = S_w \cdot (\rho_w)_i \tag{5.16}$$

Substituting Equation 5.16 into Equation 5.15,

$$\frac{\rho_f}{\rho_i} = S_w^{1-n} \tag{5.17}$$

According to Pandit and King (1979)'s experiments on sedimentary rocks ,

$$n = 0.9 log(\frac{\rho_f}{\rho_i}) + 2.3 \tag{5.18}$$

Thus, it can be easily observed that S_w is a function only related to $\frac{\rho_f}{\rho_i}$. As long as the value of $\frac{\rho_f}{\rho_i}$ is determined, the unfrozen water content can be estimated by the Archie's law. Here $a = 1$,

m = 1.5, 1.75, 2 and n = 2.5, 3.3, 5.8 for sand, silt and clay according to the previous studies (Jackson et al., 1978, Edwards et al., 1988 and King et al., 1988).

Acoustic Model

For a two-phase material comprising a continuous matrix permeated with spherical inclusions, the Kuster-Toksoz (KT) equations for the effective bulk modulus K^* and effective shear modulus G^* can be applied.

$$\frac{K^*}{K_m} = \frac{1 + [4G_m(K_i - K_m)/(3K_i + 4G_m)K_m]\,c}{1 - [3(K_i - K_m)/(3K_i + 4G_m)]c} \tag{5.19}$$

$$\frac{G^*}{G_m} = \frac{6G_i(K_m + 2G_m) + (9K_m + 8G_m)[(1-c)G_m + cG_i]}{G_m(9K_m + 8G_m) + 6(K_m + 2G_m)[(1-c)G_i + cG_m]} \tag{5.20}$$

where the subscripts m and i refer to matrix and inclusion; c is the fraction of the inclusions.

King et al. (1988) assumed that unconsolidated permafrost could be approximated by an assemblage of spherical quartz grains embedded in a matrix composed of spherical inclusions of water in ice. Thus, these equations were applied to the three-phase permafrost model by first computing the effective elastic moduli of the ice-water mixture. Considering ice playing the role of the matrix and water the inclusion. c can be replaced by S_w. Then, consider the ice-water mixture as the matrix and quartz sand as the inclusion, c equals to $(1-\phi)$. Finally, the effective elastic moduli of the frozen soil can be estimated.

Since K and G only have one variable S_w and the p-wave velocity has already be measured, the unknown S_w can be back-calculated by using Equation 3.5. The physical properties of the three phases in the KT model is shown in Table 5.1.

5.2.3 Calculations and Results

Using the HS bounds related equations, the bounds of electrical resistivity and p-wave velocity can be written as a function of unfrozen water saturation S_w. Therefore, the upper and lower bounds can be calculated by assuming S_w = 0 (completely frozen) and S_w = 1 (completely unfrozen). Meanwhile, by using the single electrical (Archie's law) and acoustic models (KT equations) which assuming certain geometric relationships between each component, the S_w corresponding to the measured electrical resistivity or acoustic velocity can be estimated.

The bounds and the calculated S_w estimations are shown in Figure 5.5. As shown in Figure 5.5,

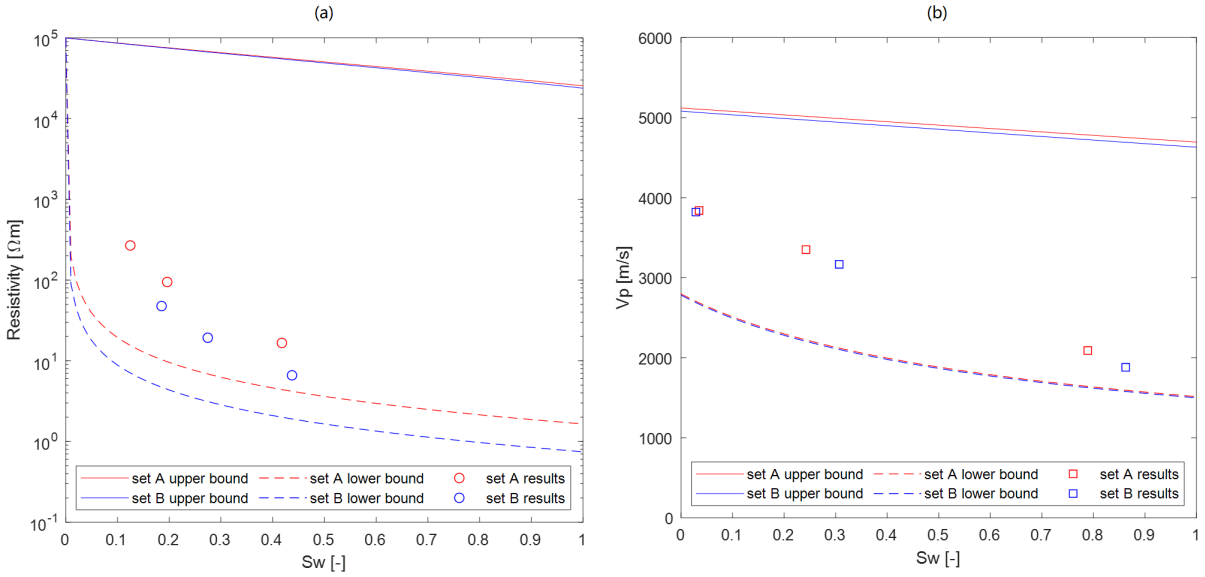

Figure 5.5: The HS bounds and S_w estimations of the (a) electrical resistivity and (b) p-wave velocity for the two sets of tests.

the bounds of the two sets of tests have an only slight difference. The difference of the lower bounds of the electrical resistivity looks larger than the other bounds. It is because that the lower bounds electrical resistivity are mostly related to the resistivity of the pore fluid, and the pore fluid resistivity of *set A* is as twice as *set B*. Also, it is because that Figure 5.5 (a) is using a logarithm y-axis. Apart from the unfrozen water saturation, the electrical upper bounds are only determined by (1) the porosity, (2)the resistivity of ice and solid; the acoustic bounds are only determined by (1) the porosity, (2) the elastic modulus a of each component and (3) the density of each component. Since these parameters of *set A* and *set B* are the same or very close, these HS bounds are almost the same.

For the electrical HS bounds shown in Figure 5.5 (a), the upper bound represents that the pore fluid is completely isolated and the lower bound indicates that the pore fluid is completely interconnected. In other words, the upper bound assumes a series system and the lower bound assumes a parallel system. For a series system, the minimum upper bound is determined by the porosity and the resistivity of the solid, the contribution of S_w to the increase of resistivity shows a linear relationship. Since the porosity in both sets are close to 0.50 and assuming ice and solid have the same resistivity, the upper bound doubles with descending S_w, which only

shows a small change in a logarithm axis. For a parallel system, the current always tend to find the path with the lowest resistivity, which makes the interconnected saline channels becomes the best choice. Therefore, the unfrozen water saturation is critical to the resistivity of the mixture. When S_w is approaching to 0, it represents that all the pore fluid is converting to ice and the saline channels are "closing". When all the channels are closed, the pore fluid will become isolated just as what the upper bound represents. Therefore, the lower bound increases dramatically at low S_w and meet up with the upper bound at the same point at $S_w = 0$.

For the acoustic HS bounds shown in Figure 5.5 (b), the upper bound represents that quartz is as the shell of the sphere, and upper bound represents that fluid is as the shell. For the upper bounds, since the S_w only influence the elastic modulus of the inner core surrounded by a stiff shell, the formation of ice has only limited effect on the total effective modulus. For the lower bounds, the elastic modulus of the outer shell (fluid) varies a lot with the changes of S_w, which leads to a significant effect on the total effective modulus. When the material is frozen, the sphere gains a relatively stiff ice shell. Due to ice has smaller modulus than quartz, the lower bounds at $S_w = 0$ is still lower than the upper bounds.

The measurements and their corresponding S_w estimations are also plotted in Figure 5.5. Even though the estimations are made by certain assumptions of the geometry in the mixtures, Figure 5.5 (a) and (b) still illustrate that the measurements of electrical resistivity and the p-wave velocity of the frozen *Halden Silt* fit the HS bounds very well. However, it can be observed that the S_w estimations from the electrical model are between 0 and 0.5, while the estimations from the acoustic model are between 0 and 0.9. For comparing the estimation from different models, the estimated S_w and the temperatures at the measurements are plotted in Figure 5.6.

As shown in Figure 5.6, the estimated S_w from electrical and acoustic models can be observed apparent inconsistency for the same samples at the same temperature. At lower temperatures (below -6°C), the differences between electrical and acoustic S_w estimations are very small (the largest difference is less than 0.2). For the estimation based on the measurements recorded above -6°C, the differences are larger than 0.4. Due to lacking a measurement showing the real unfrozen water saturation, it is hard to determine which model is more accurate.

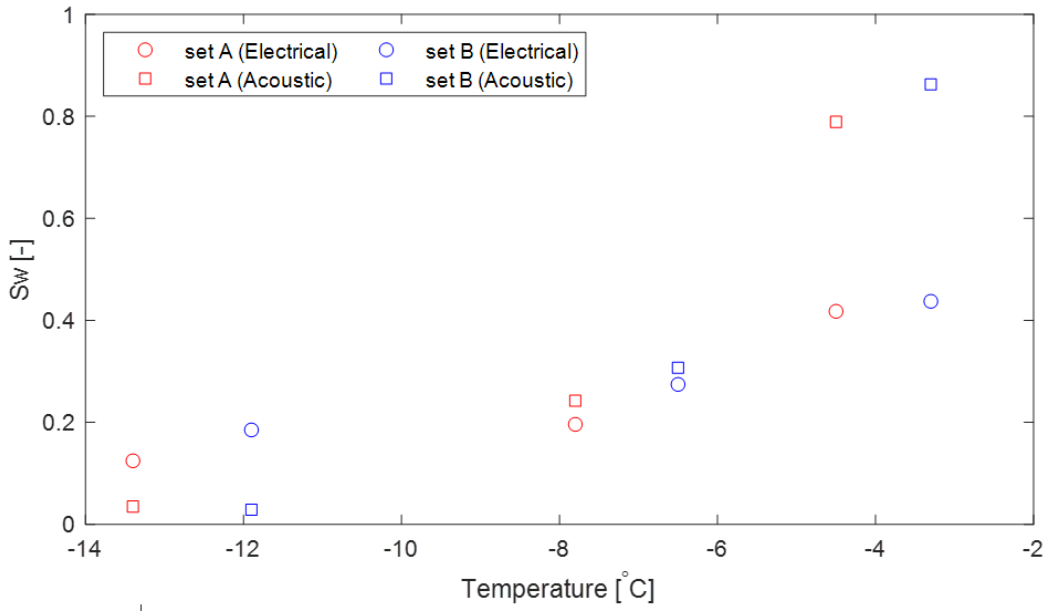

Figure 5.6: The temperatures at the measurements versus the S_w estimations from electrical and acoustic models of the two sets of tests.

5.2.4 Motivattion for A Joint Method

As described previously, the joint measurements are in line with the theoretical HS bounds, even though the S_w is estimated from models with predetermined geometric relationships. It indicates that the assumptions we made for modelling the frozen soil are reasonable. Otherwise, the estimations of S_w will not be within the range of from 0 to 1. On the other hand, it shows that it is feasible to model the frozen soil with reasonable assumptions.

The bounds of electrical resistivity are made without assuming any geometric conditions, and the bounds of p-wave velocity are determined by using a simple spherical model without any further geometric assumptions. By specifying the geometric relationships between each component, the bounds can be narrowed. If using a geometric coefficient to describe the inner geometry of the material, the upper and lower bounds can be controlled by two variables: the unfrozen water saturation and the geometric coefficient. Meanwhile, if the electrical and acoustic models are assuming similar or ideally the same geometric relationships between each component which is described by the same geometric coefficient, the joint measurement results will allow the geometric coefficient and the unfrozen water saturation to be solved simultaneously.

The introduction of the geometric coefficient gives more flexibility for modelling the frozen soil, due to the geometric relationships are not necessarily to be predetermined. The simultaneous solution is also expected to provide more reasonable geometric details, which is likely to lead to a more accurate estimation of S_w. Lyu et al. (2019) have combined an acoustic SCA model with an electrical EMT model to solve aspect ratio α and unfrozen water saturation S_w together in sandstone, and the S_w estimates from the joint SCA-EMT method are most likely between estimates from single electrical (Archie's law) and acoustic (Weight equations) model. It indicates that the electrical method might overestimate the S_w and the acoustic method might underestimate it. Even though the joint model proposed in the paper was derived from different theories, it still shows the potential of the joint electrical and acoustic method for a more accurate estimation of unfrozen water saturation.

Chapter 6

Conclusions and Suggestions for Further Work

The main achievements made during this course of work are listed as blow.

1. Development of a joint measurement system which can collect and process the electrical and acoustic data simultaneously, including the test apparatus and the *LabVIEW* program.
2. Calibration of the joint measurement system by adjusting the setup and optimizing the data processing. The measurements of dummy samples have been proved to be consistent with previous researches and a purchased precision instrument.
3. Collection of good experimental data of the electrical resistivity and the p-wave velocity of two sets of *Halden Silt* samples with different salinity at different temperatures. The measurements have been verified to match the experimental results from previous credible publications and locate within the Hashin-Shtrikman bounds.
4. Verification of the inconsistency of unfrozen water saturation estimated by electrical (Archie's law) and acoustic (KT) models.

According to the accomplished work mentioned above, it reveals that a joint method can potentially improve the accuracy of the unfrozen water saturation estimation. This thesis suggests a joint electrical and acoustic method should using the same geometric assumption which controlled by one geometric coefficient. Then, with the joint measurement data, the geometric coefficient and the unfrozen water saturation can be solved simultaneously.

For the development of the joint method, more sets of experiments should be conducted. The data acquired from these experiments can be used for training the new models. A reference unfrozen water content measured by the nuclear magnetic resonance method (NMR) should be quite useful for verifying the unfrozen water saturation estimations, which is suggested to do in the future. Also, with the reference unfrozen water content, we can study the fitness of different models at different conditions. For example, maybe the acoustic model fit the lower temperature better than the electrical model.

Anyway, accurate experimental data ensures the accuracy of the models. Here are some suggestions for improving the current experiment.

1. Find a cold room or a freezer which can control the temperature more precisely, or conduct the multiple sets of tests simultaneously. Then the measurements can be recorded at the same temperatures.
2. Measure the temperature inside the sample holder.
3. Continuous measurement and extend the range of the variation of temperature. Thus the electrical and acoustic measurements versus temperatures can be plotted directly, instead of using fitting curves.
4. Increase the dimension (especially the length) of the sample tube and increase the transmitted signals. Thus more clear raw data can be obtained.
5. Improve the procedure of sample preparation. This can make different samples have the closest properties, especially the porosity and water saturation.
6. Measure the density and porosity. The density and porosity in this thesis are calculated by assuming the solid phase of the silt sample is only quartz.
7. Replace the electrodes with more suitable materials.

The same test setup can also be slightly modified for further studies. For example, we designed another sample holder for studying water transportation during freezing and thawing. However, it has not been implemented due to a lack of time and equipment. In this setup, ten potential

electrodes, ten temperature sensors and ten pairs of piezo pads are placed along with the sample holder. The unfrozen water content at each position could be estimated by a new joint method, then the vertical water transportation can be revealed.

Appendix A

Acronyms

AC Alternating Current

DC Direct Current

EMT Effective Medium Theory

HS bounds Hashin-Shtrikman bounds

KT model Kuster-Toksoz equations (model)

NMR Nuclear Magnetic Resonance

SCA Self-Consistent Approximation

UWS Unfrozen Water Saturation

Appendix B

Figures

B.1 *LabVIEW* Program

B.2 Calibration

B.3 Test Results

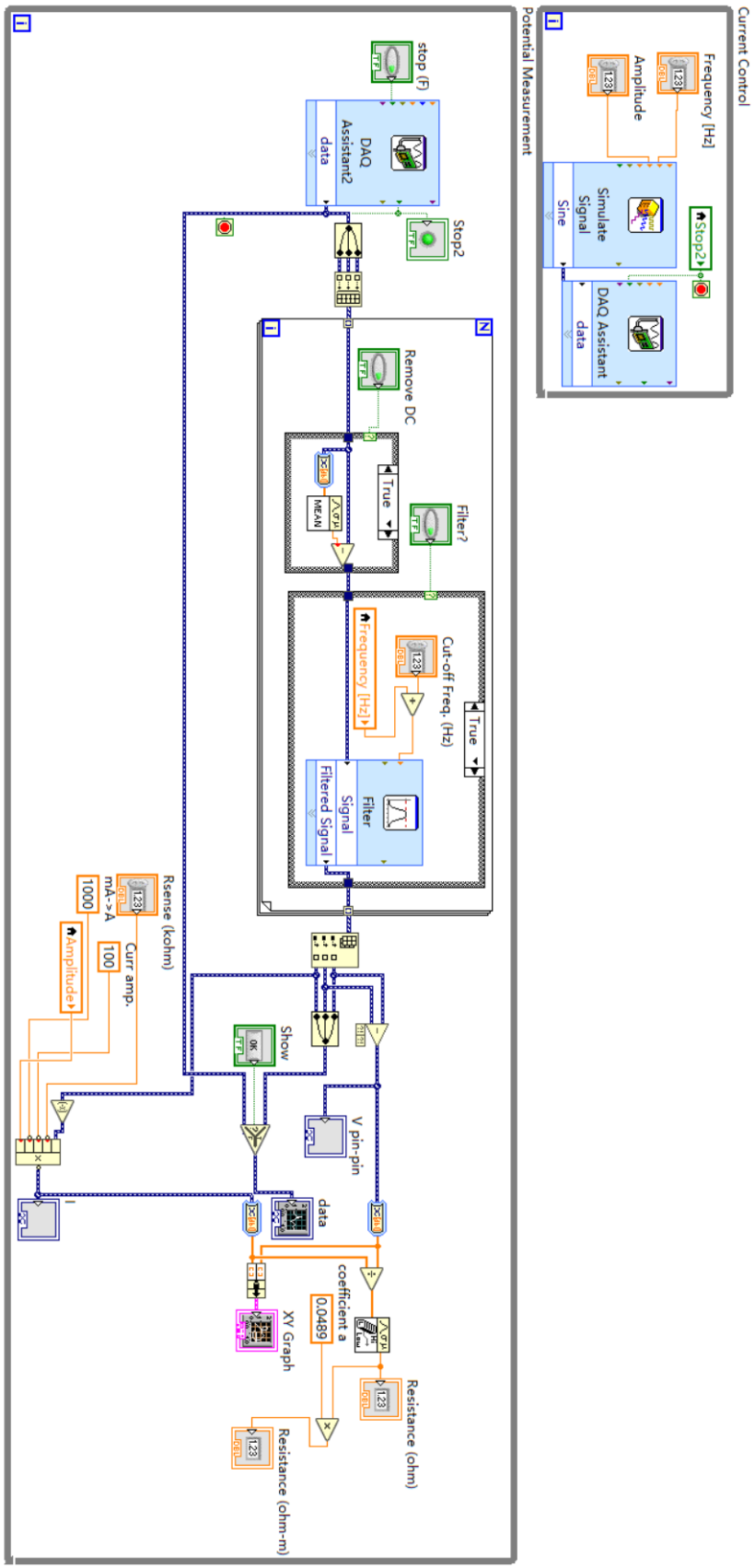

Figure B.1: Block diagram of the electrical *LabVIEW* program.

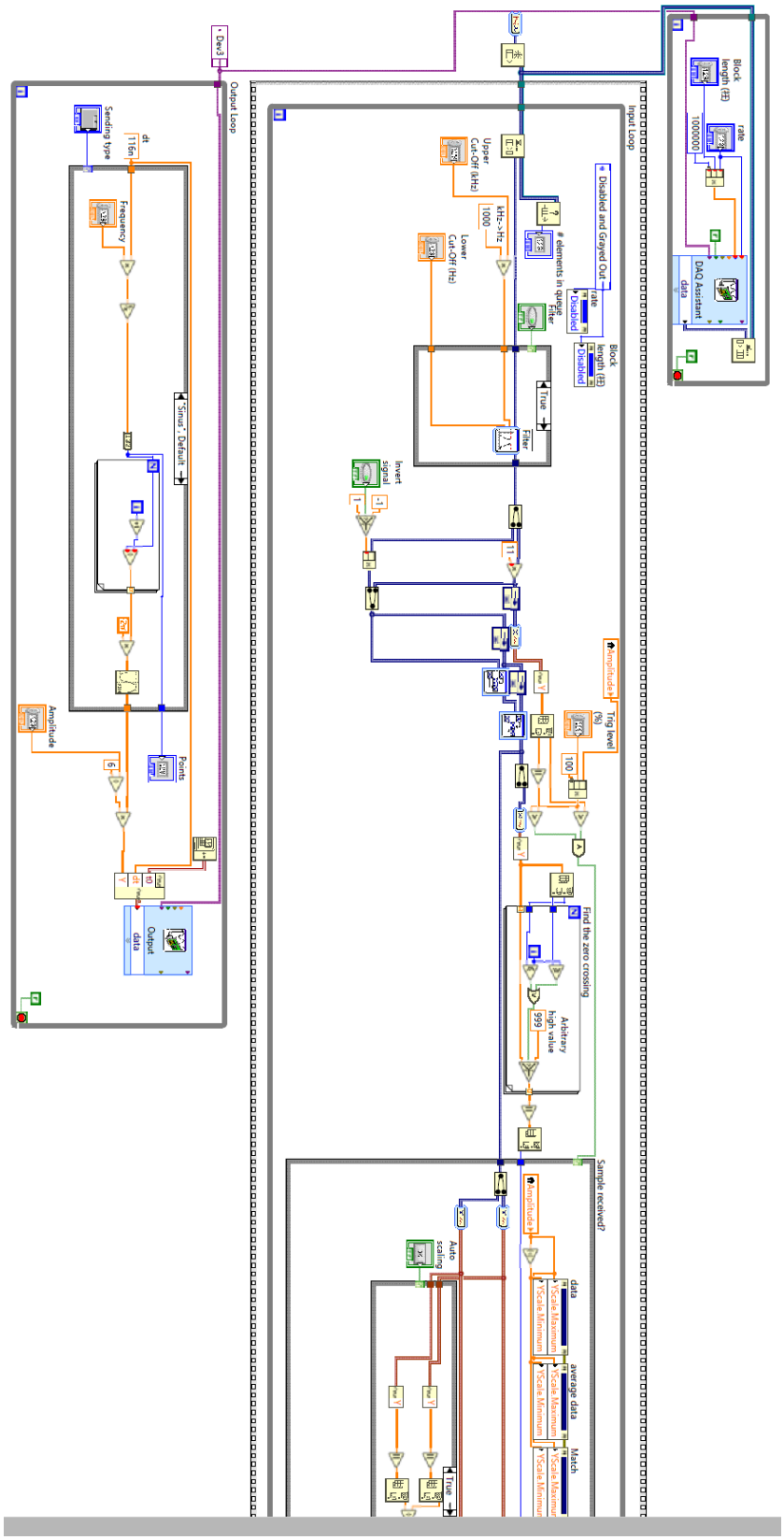

Figure B.2: Block diagram of the acoustic *LabVIEW* program (a).

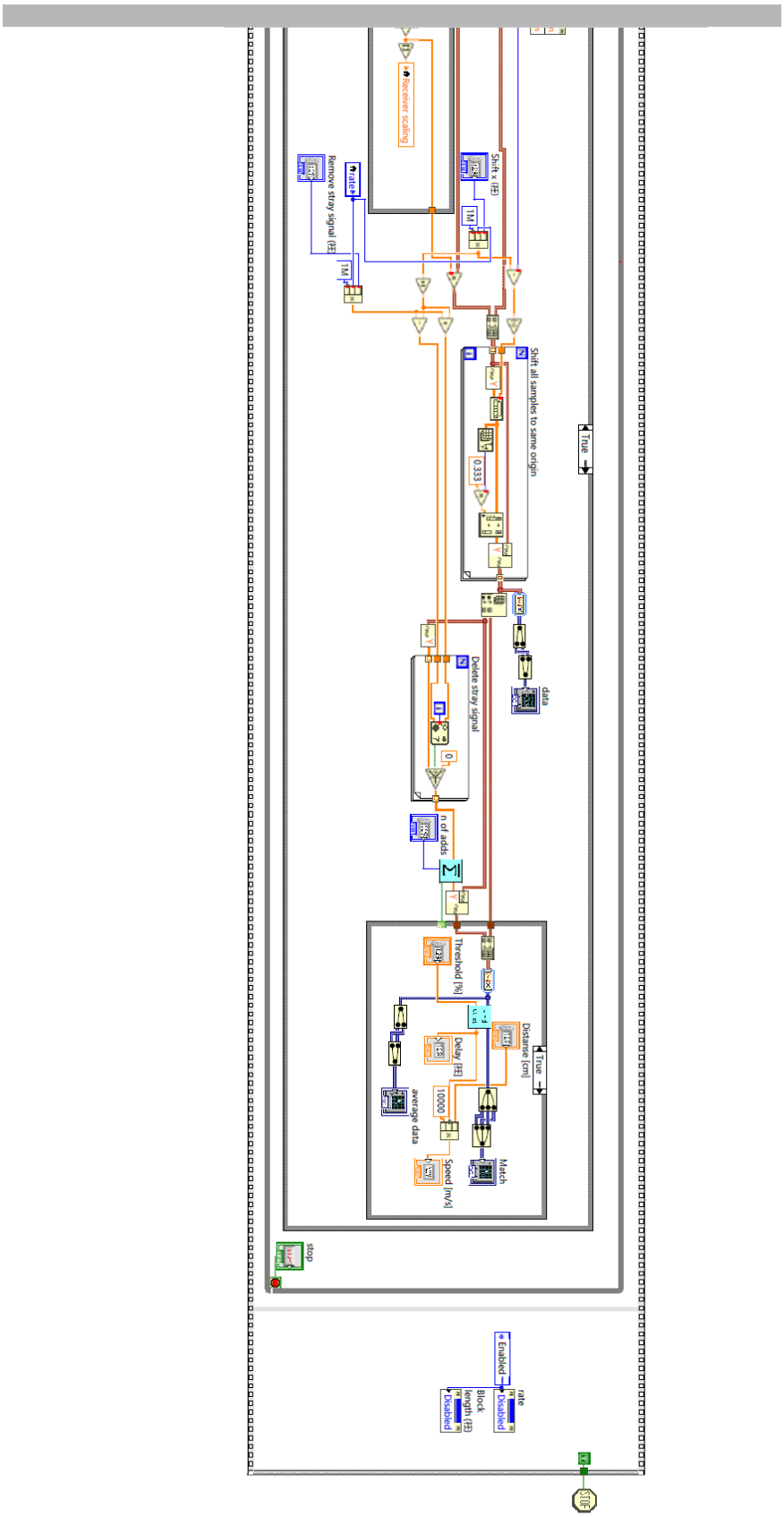

Figure B.3: Block diagram of the acoustic *LabVIEW* program (b).

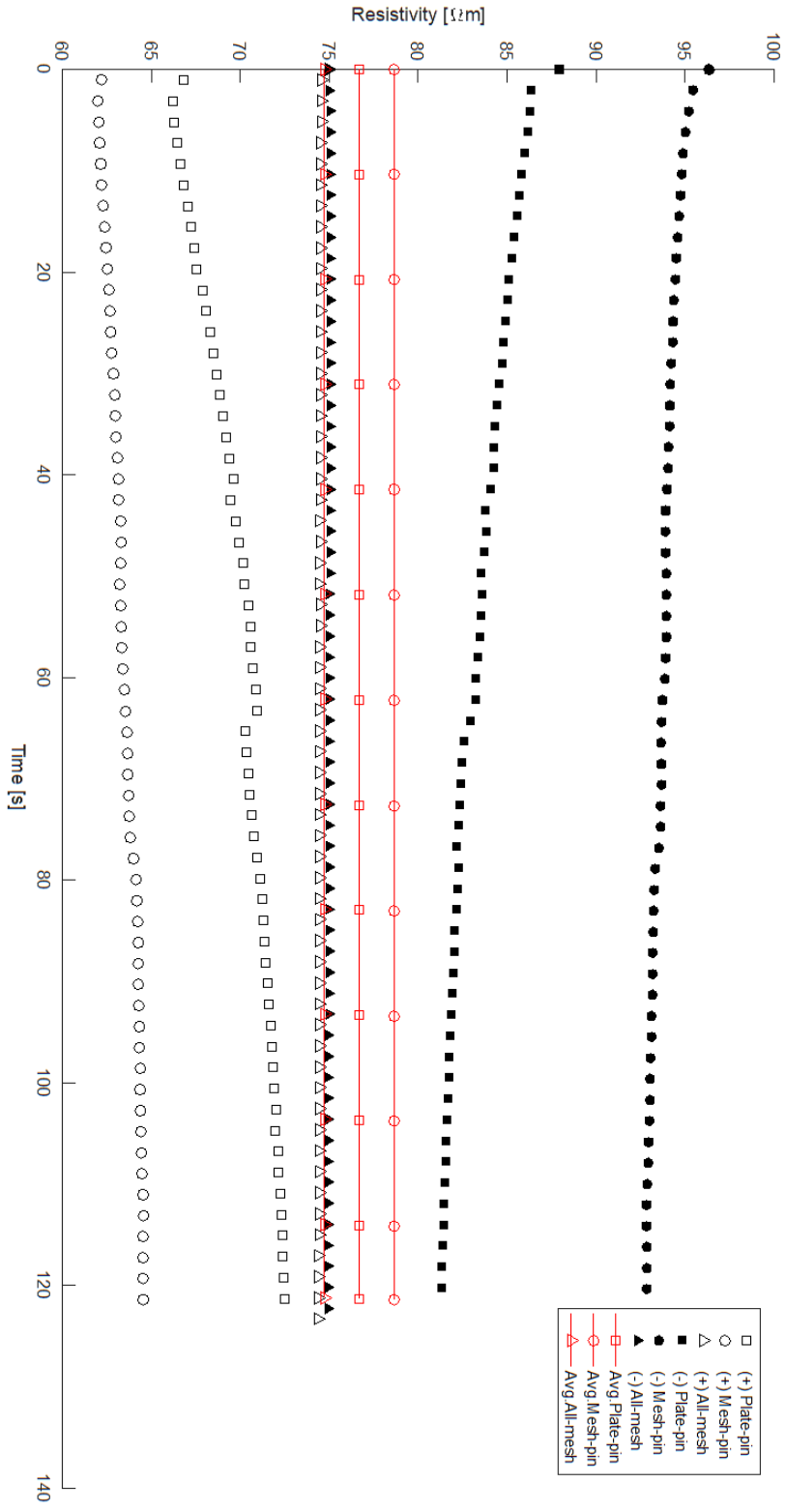

Figure B.4: The measured resistivity of the three setups.

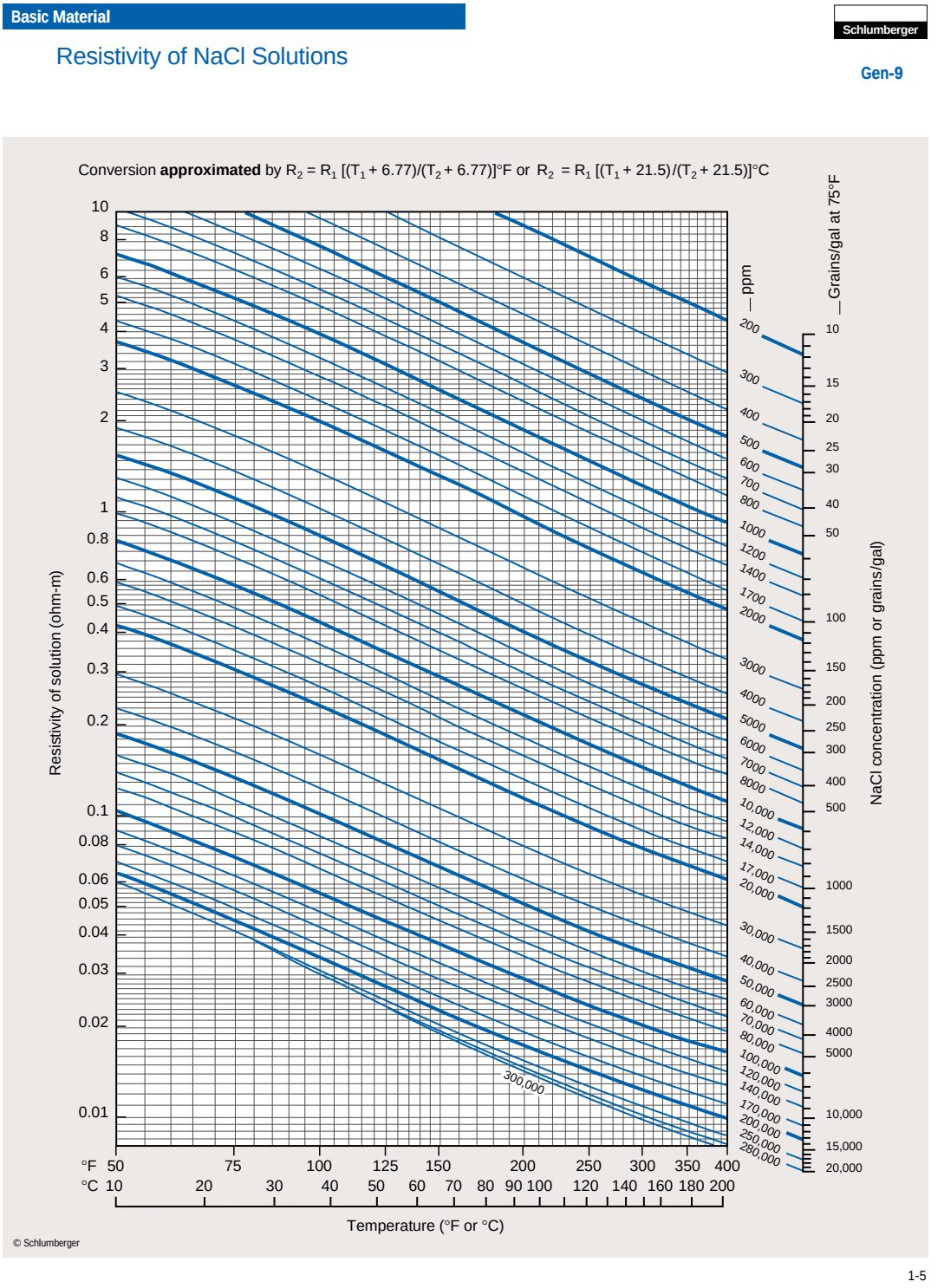

Figure B.5: Resistivity of *NaCl* Solutions by *Schulumberger*.

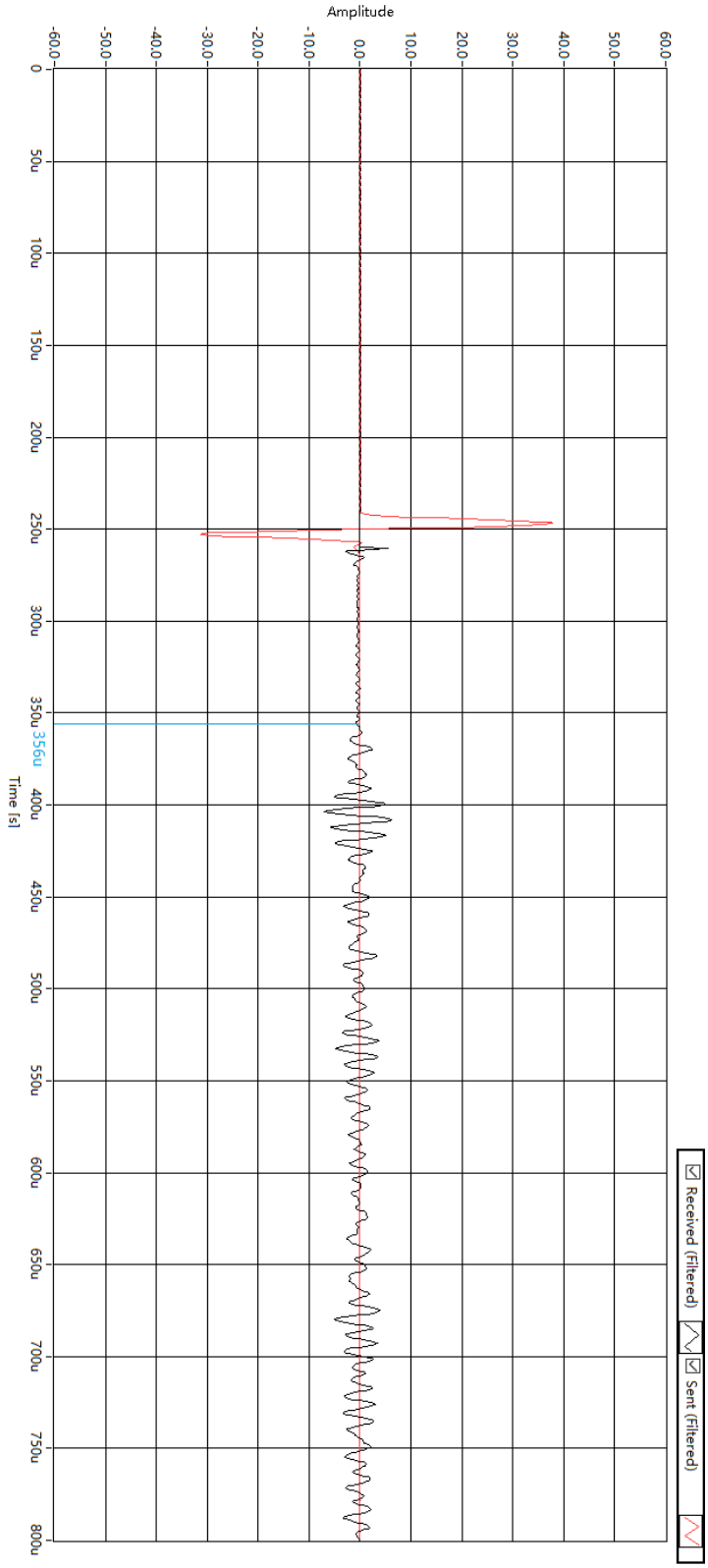

Figure B.6: Acoustic wave velocity in water tank with 16.3cm separations between the two piezo pads.

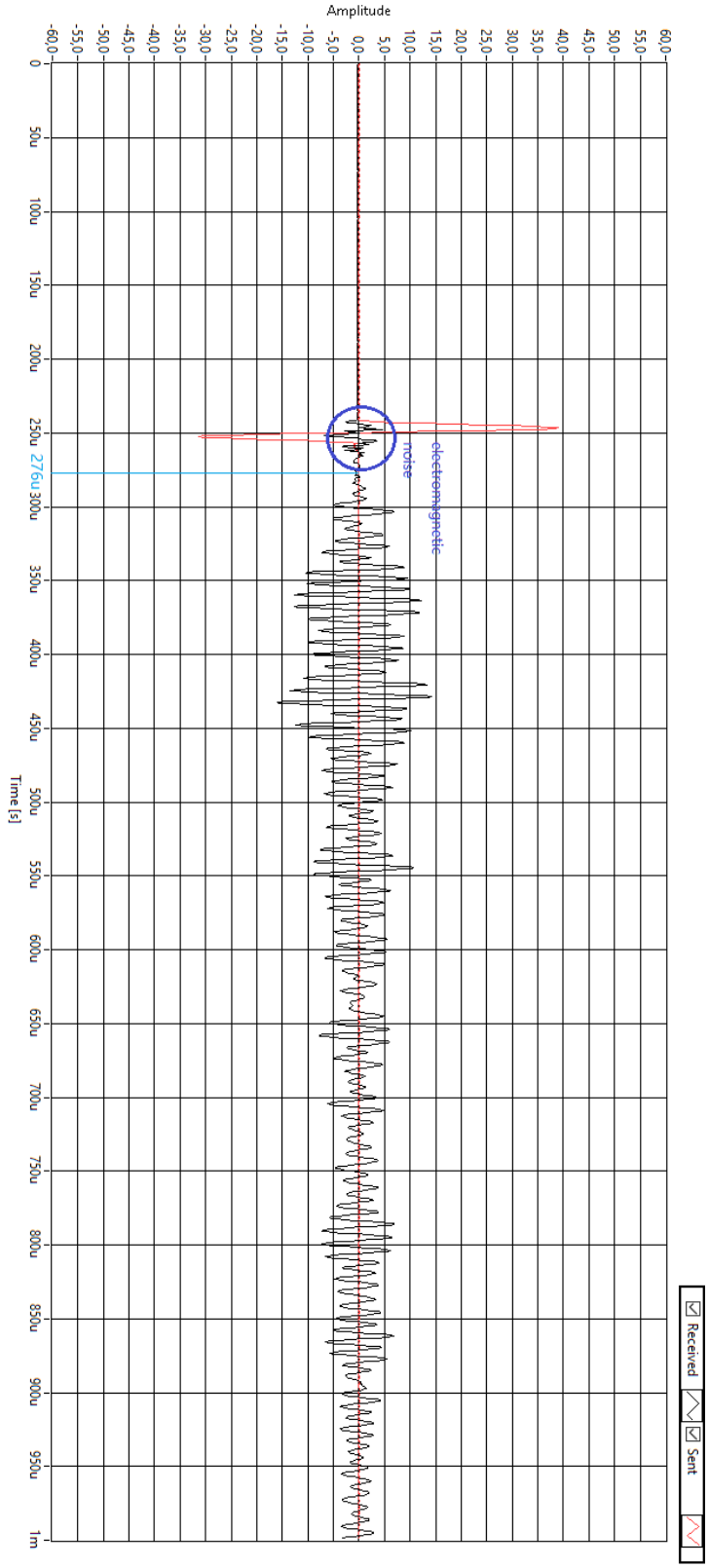

Figure B.7: Acoustic wave velocity in aluminum rod with the length of 15cm.

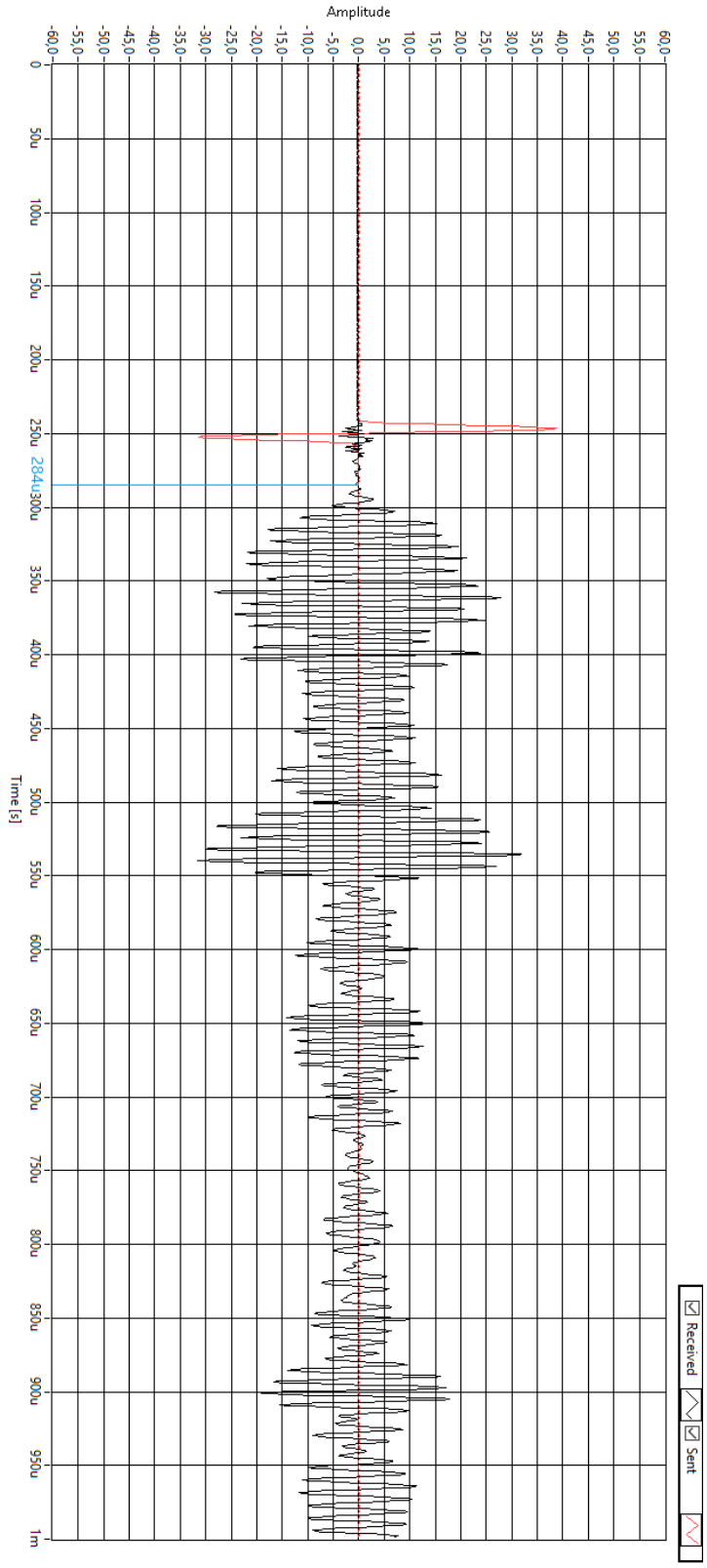

Figure B.8: Acoustic wave velocity in aluminum rod with the length of 20cm.

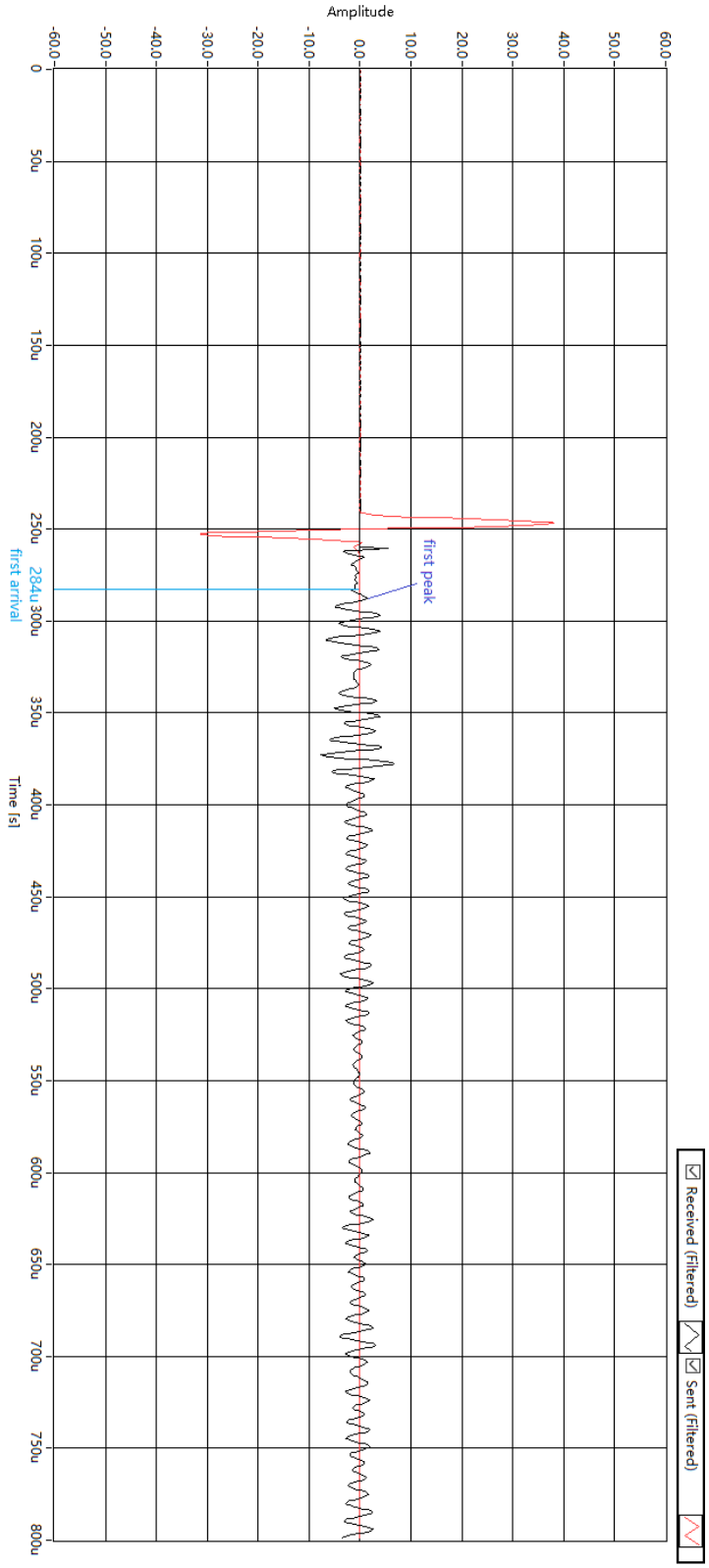

Figure B.9: Acoustic wave velocity in water tank with 5.3cm separations between the two piezo pads.

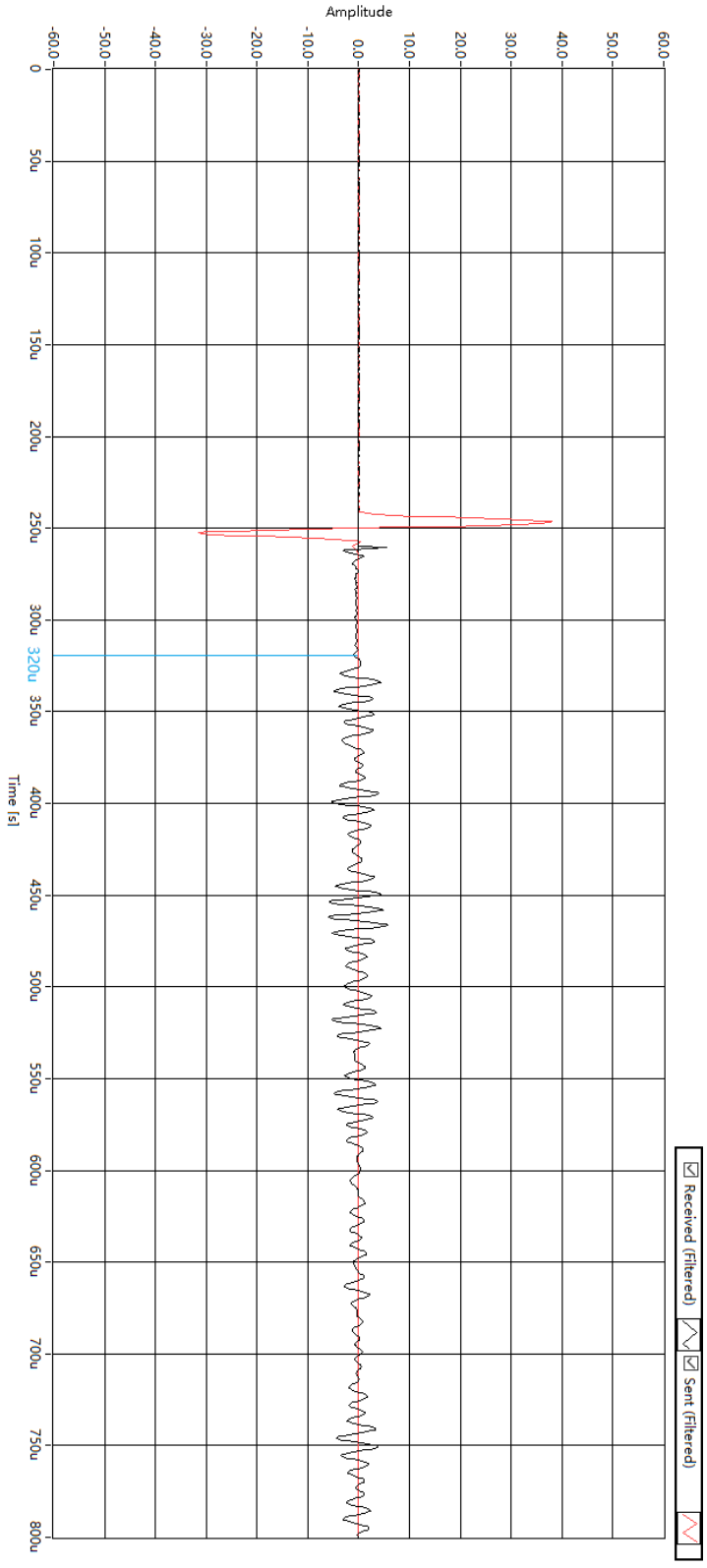

Figure B.10: Acoustic wave velocity in water tank with 10.8cm separations between the two piezo pads.

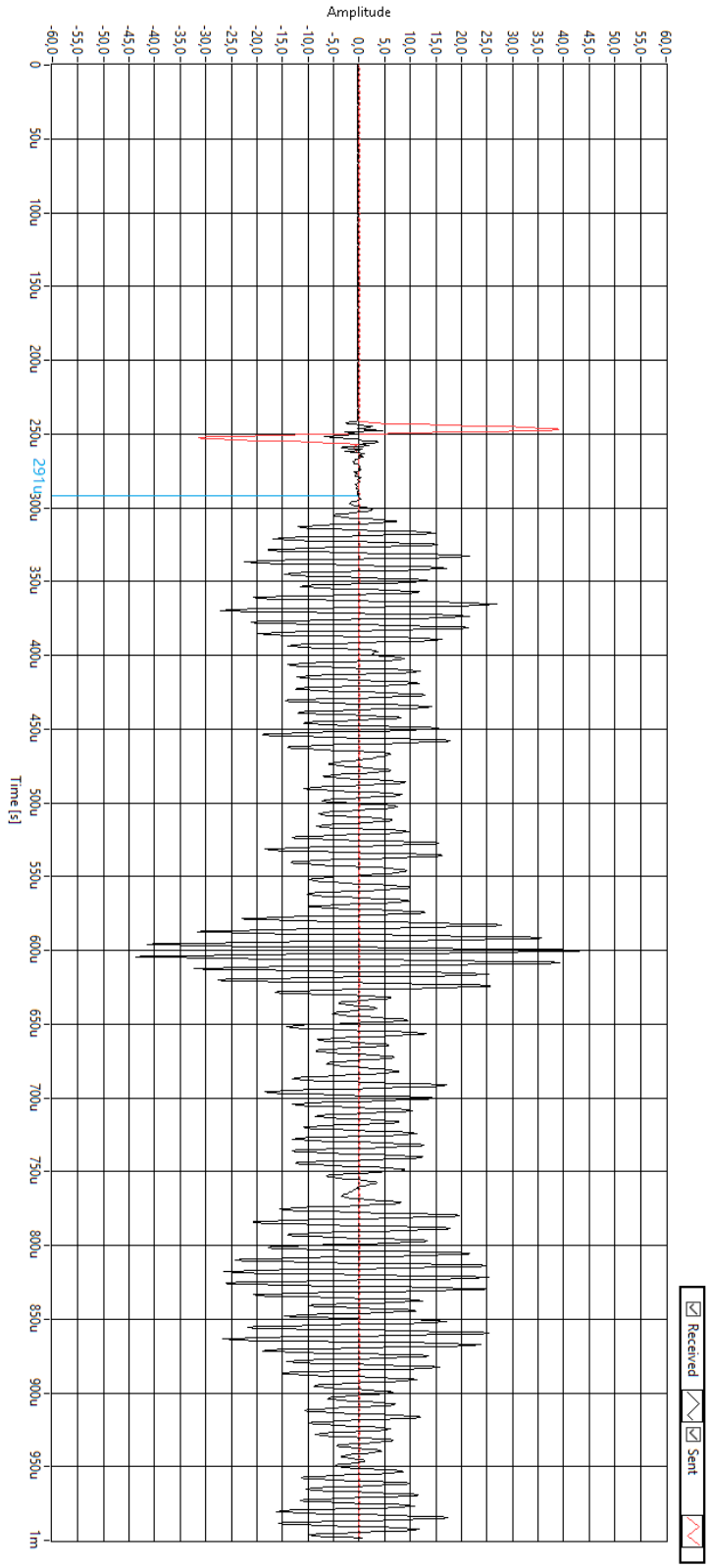

Figure B.11: Acoustic wave velocity in aluminum rod with the length of 25cm.

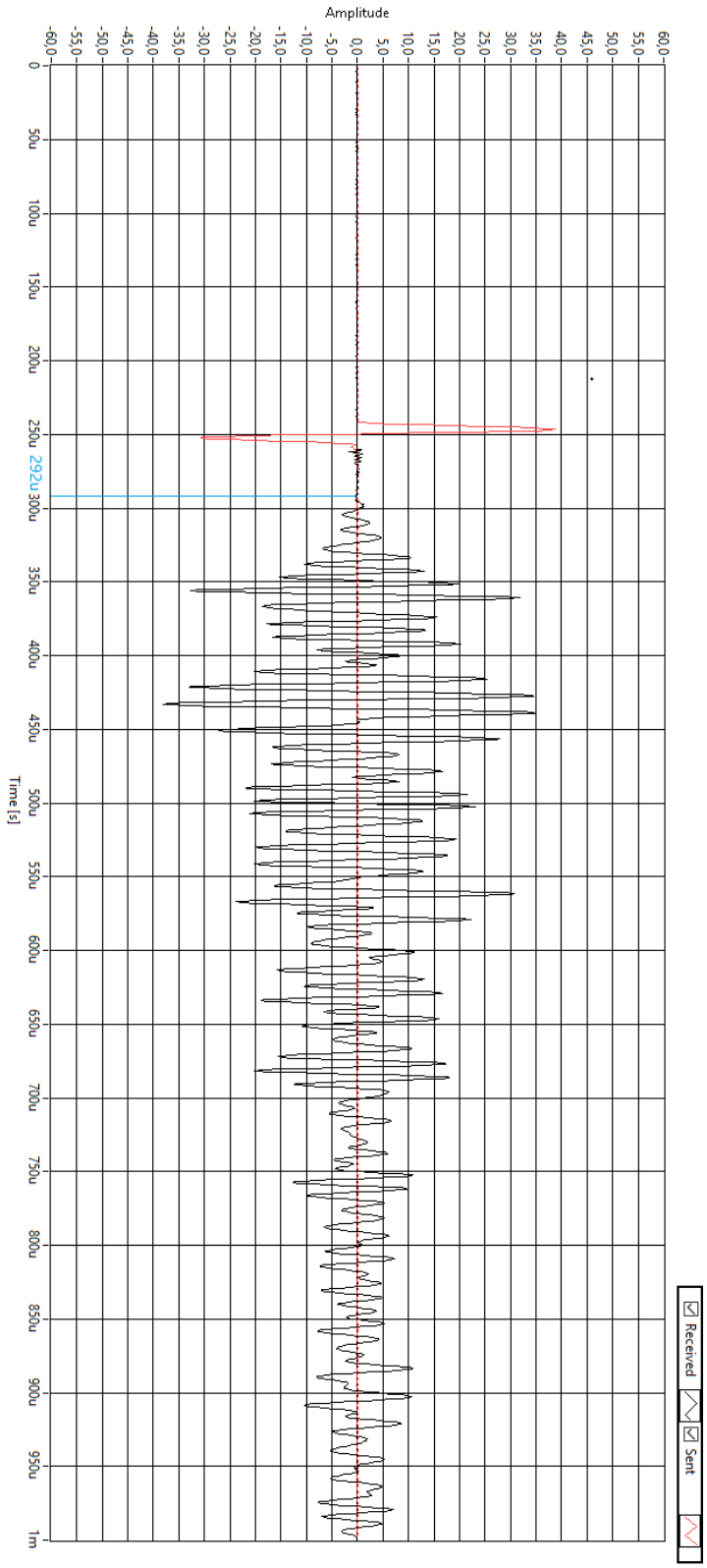

Figure B.12: Acoustic wave velocity in ice with 16cm separations between the two piezo pads.

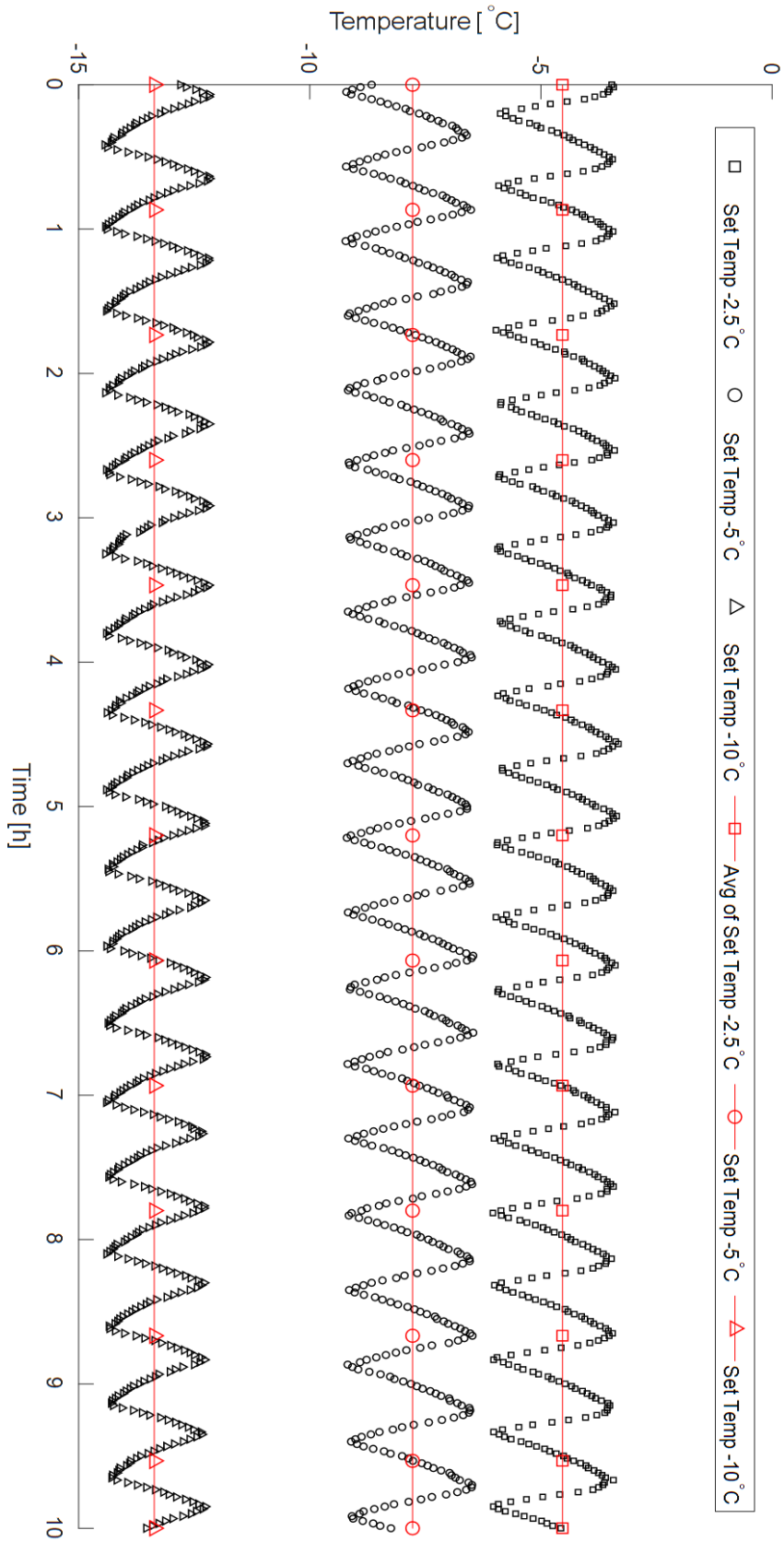

Figure B.13: The average of actual temperatures measured during last 10 hours (stable) of the tests in *Set A*.

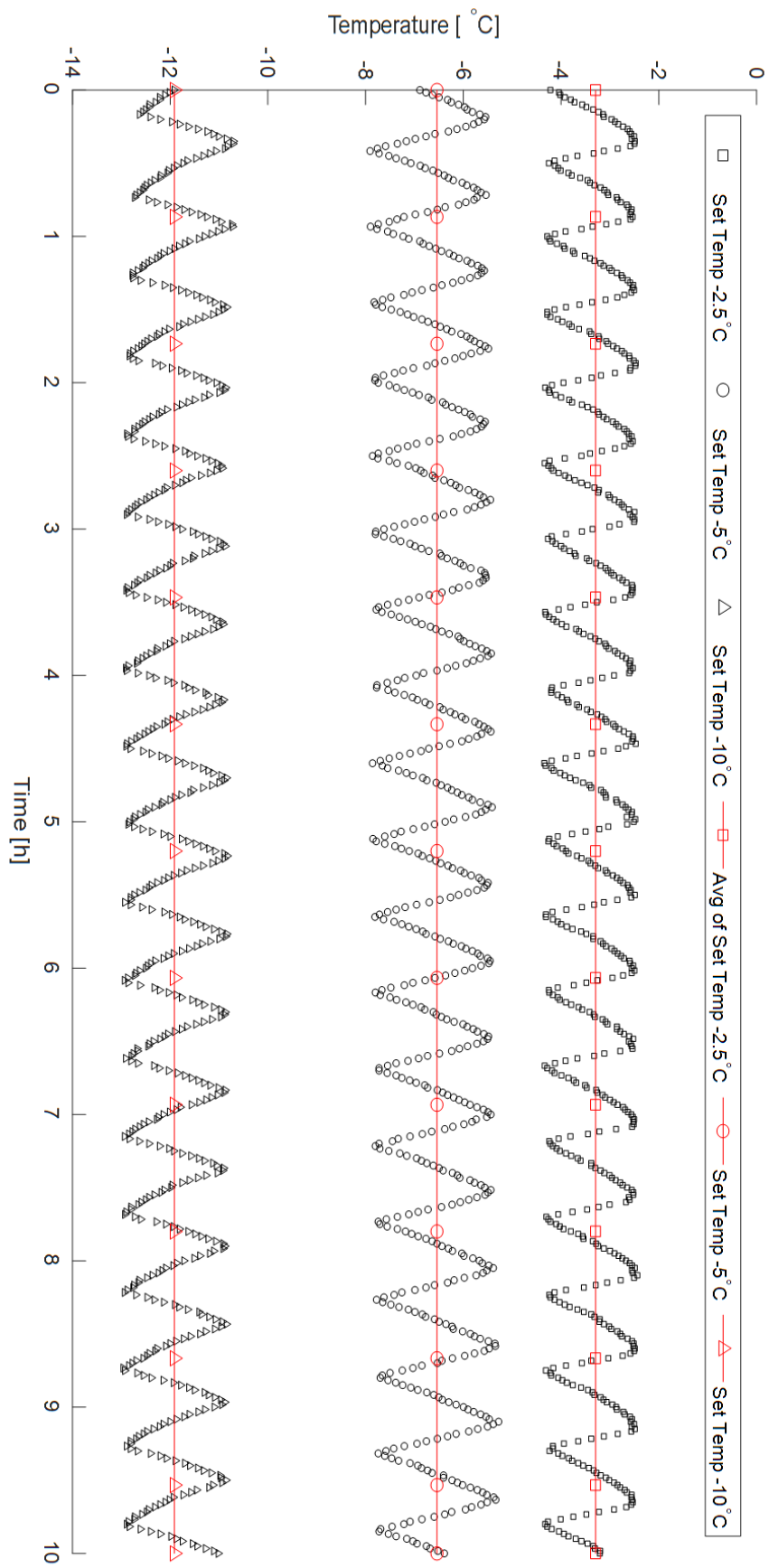

Figure B.14: The average of actual temperatures measured during last 10 hours (stable) of the tests in *Set B*.

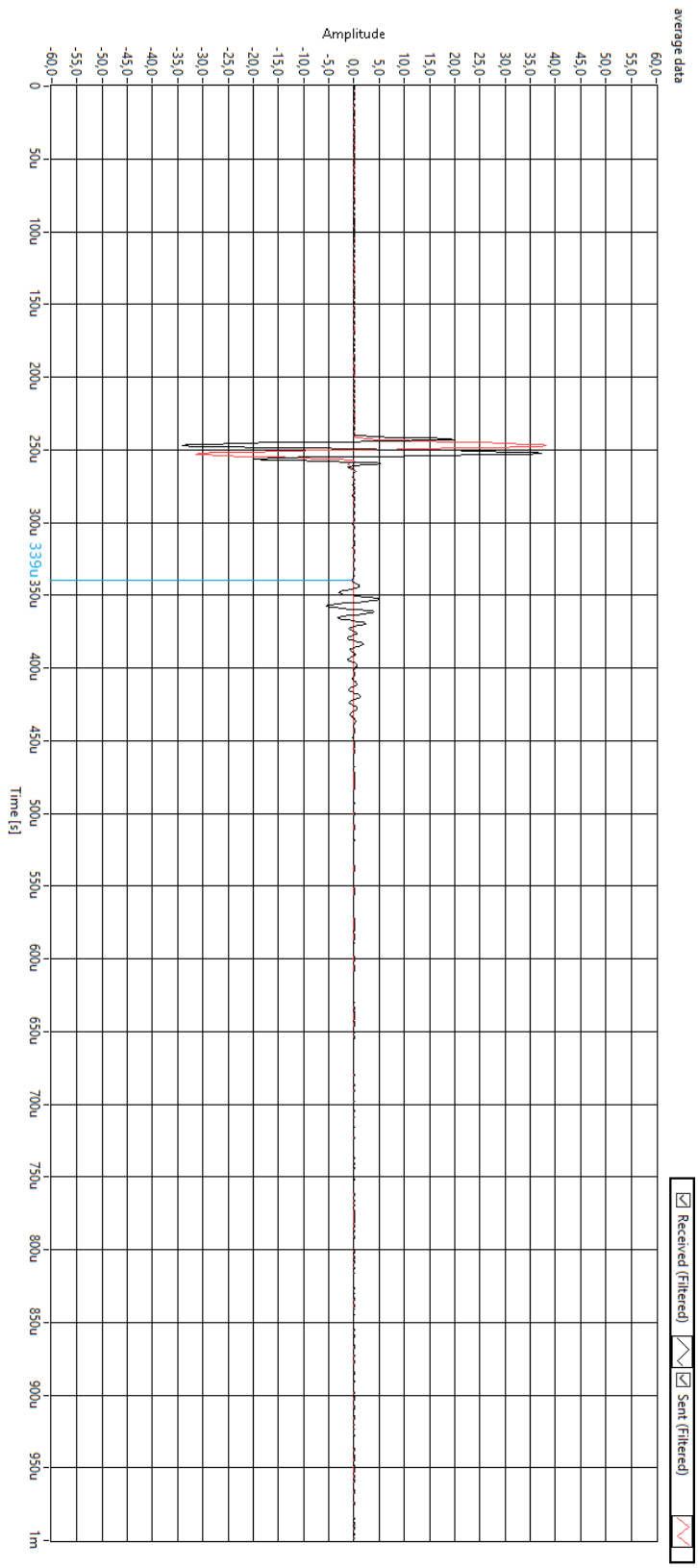

Figure B.15: The acoustic results of *Set A* at -4.5°*C*, with 200 times stacking.

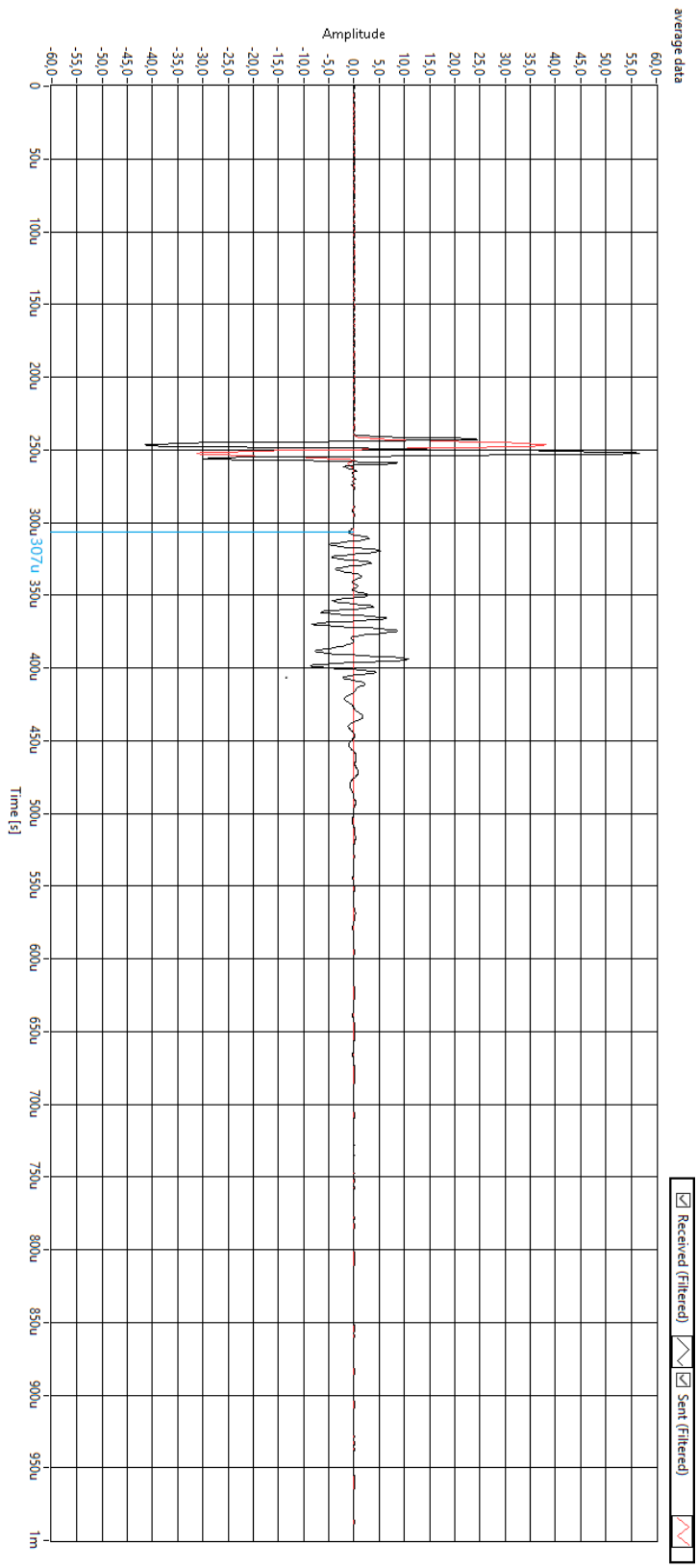

Figure B.16: The acoustic results of *Set A* at -7.8°*C*, with 200 times stacking.

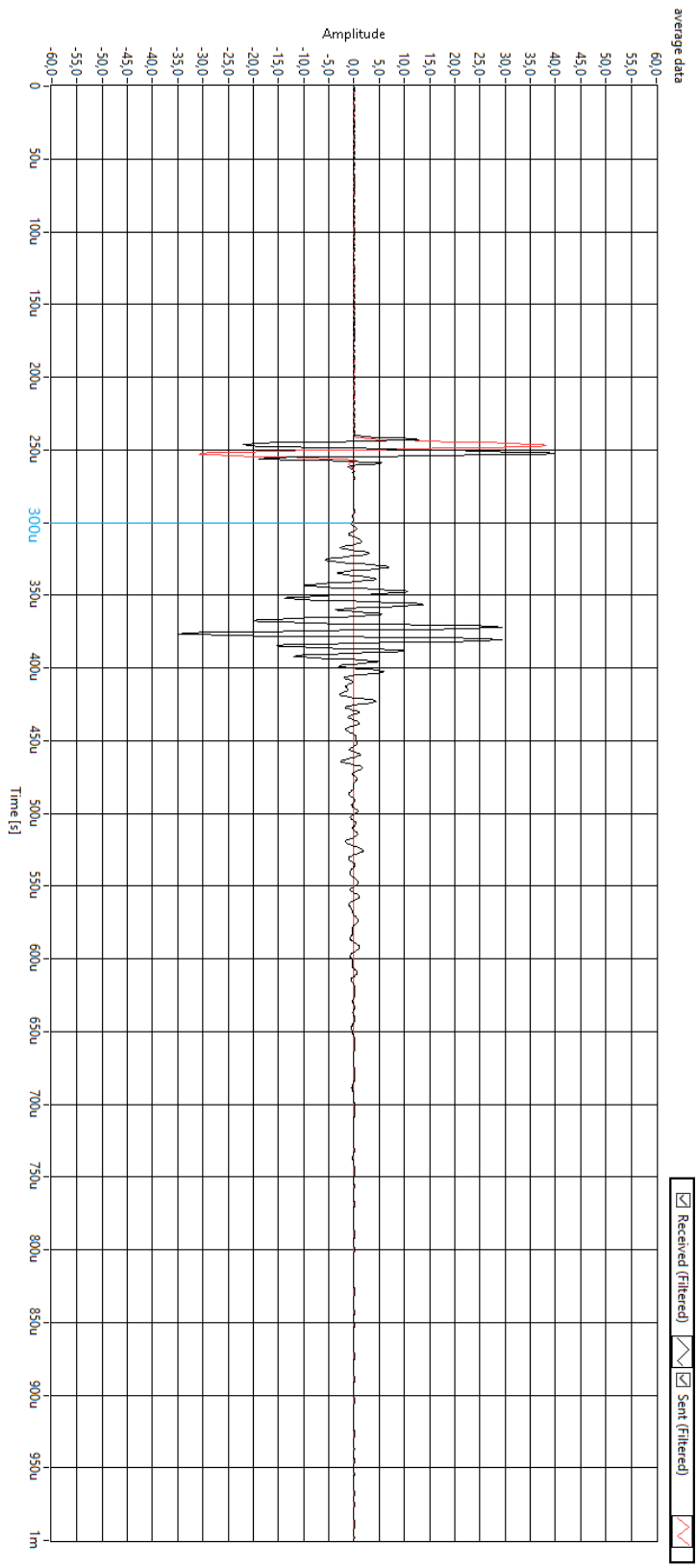

Figure B.17: The acoustic results of *Set A* at -13.4°*C*, with 200 times stacking.

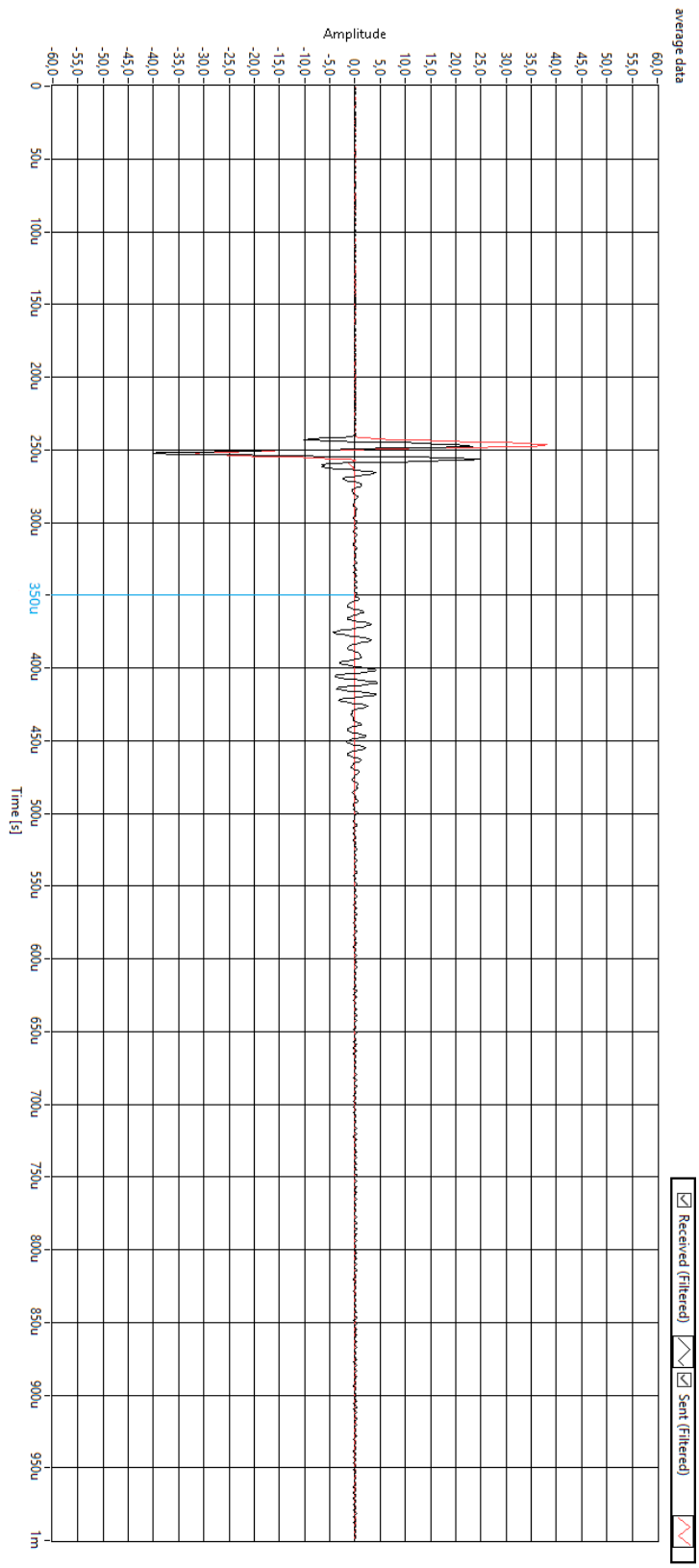

Figure B.18: The acoustic results of *Set B* at -3.3°*C*, with 200 times stacking.

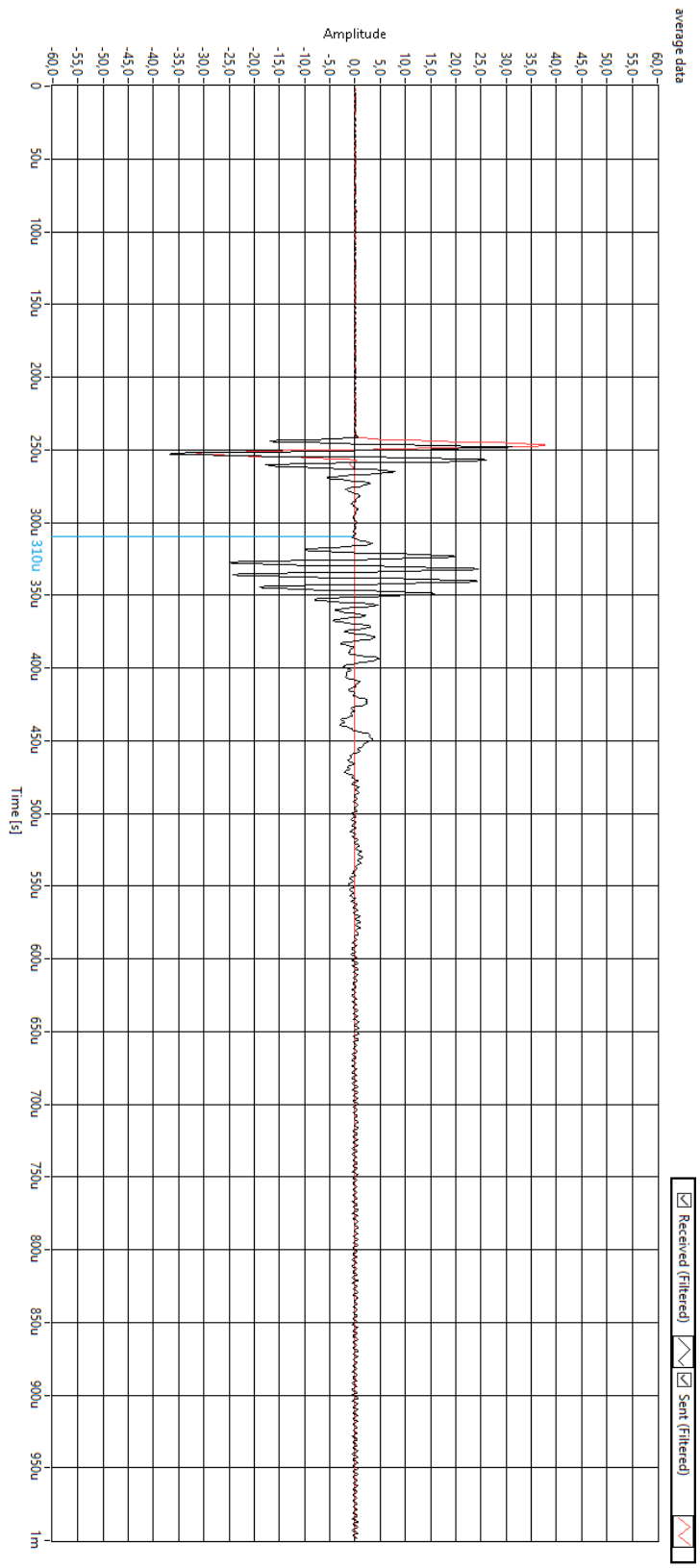

Figure B.19: The acoustic results of *Set B* at -6.5°*C*, with 200 times stacking.

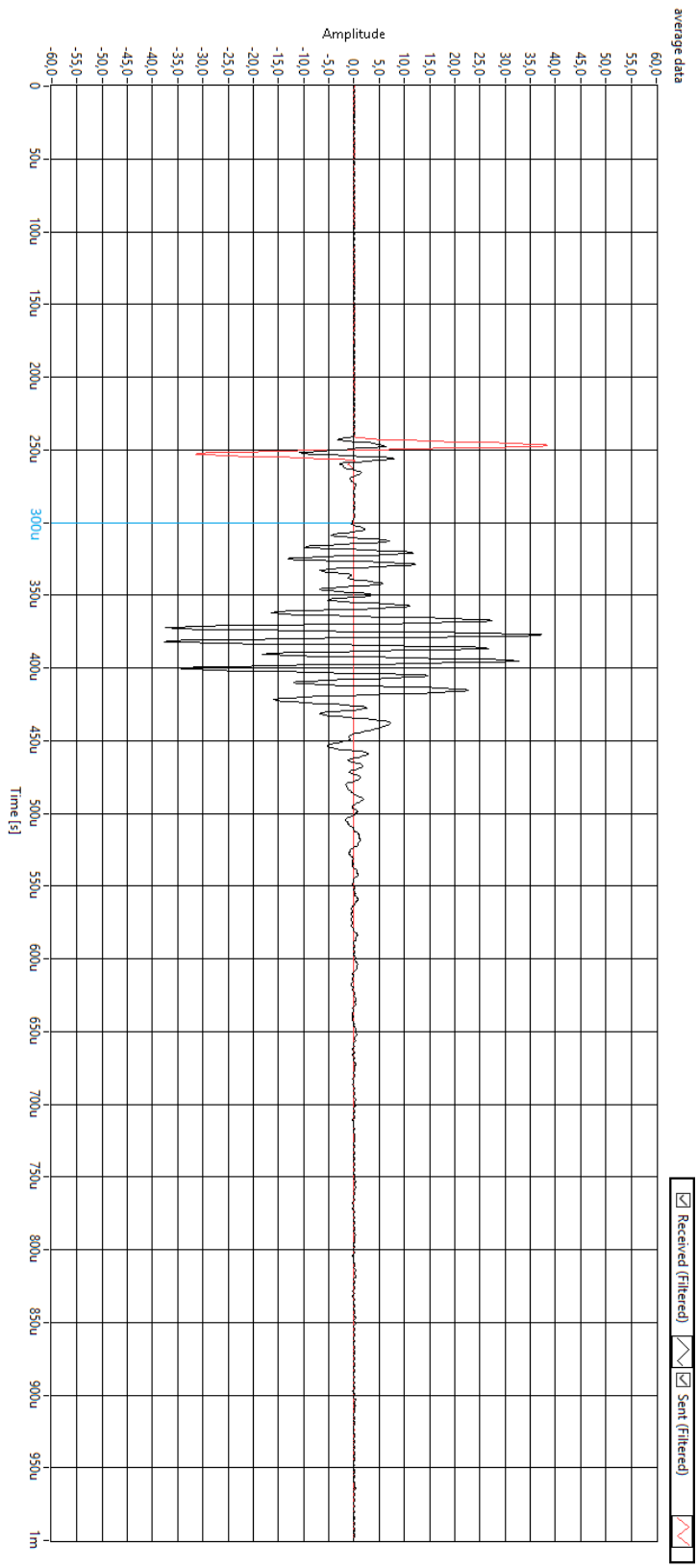

Figure B.20: The acoustic results of *Set B* at -11.9°*C*, with 200 times stacking.

Bibliography

Alipio, R. and Visacro, S. (2014). Modeling the frequency dependence of electrical parameters of soil. *IEEE Transactions on Electromagnetic Compatibility*, 56(5):1163–1171.

Andersland, O. B. and Ladanyi, B. (2004). *Frozen ground engineering*. John Wiley & Sons.

Anderson, D. M. and Hoekstra, P. (1965). Migration of interlamellar water during freezing and thawing of wyoming bentonite 1. *Soil Science Society of America Journal*, 29(5):498–504.

Anderson, D. M. and Tice, A. R. (1971). Low-temperature phases of interfacial water in clay-water systems 1. *Soil Science Society of America Journal*, 35(1):47–54.

Arps, J. et al. (1953). The effect of temperature on the density and electrical resistivity of sodium chloride solutions. *Journal of Petroleum Technology*, 5(10):17–20.

Bilaniuk, N. and Wong, G. S. (1993). Speed of sound in pure water as a function of temperature. *The Journal of the Acoustical Society of America*, 93(3):1609–1612.

Black, R. F. (1975). Permafrost terminology r. j. e. brown and w. o. kupsch. 1974. national research council of canada, technical memorandum no. 111, 62 pp., $3.00. *Quaternary Research*, 5(3):468–468.

Brown, S. R., Sorenson, J. R., and Brown, T. I. (2004). A laboratory study of the complex electrical resistivity response of soils. In *Symposium on the Application of Geophysics to Engineering and Environmental Problems 2004*, pages 528–539. Society of Exploration Geophysicists.

Carmichael, R. S. (2017). *Practical Handbook of Physical Properties of Rocks and Minerals (1988)*. CRC press.

Christ, M., Kim, Y.-C., and Park, J.-B. (2009). The influence of temperature and cycles on acoustic and mechanical properties of frozen soils. *KSCE Journal of Civil Engineering*, 13(3):153–159.

Daniels, J. J., Keller, G. V., and Jacobson, J. (1976). Computer-assisted interpretation of electromagnetic soundings over a permafrost section. *Geophysics*, 41(4):752–765.

Edlefsen, N. and Anderson, A. B. (1941). The four-electrode resistance method for measuring soil-moisture content under field conditions. *Soil Science*, 51(5):367–376.

Edwards, R., Wolfgram, P., and Judge, A. (1988). The ice-moses experiment: mapping permafrost zones electrically beneath the beaufort sea. *Marine geophysical researches*, 9(3):265–290.

Fofonoff, N. P. and Millard Jr, R. (1983). Algorithms for the computation of fundamental properties of seawater. .

Giao, P., Chung, S., Kim, D., and Tanaka, H. (2003). Electric imaging and laboratory resistivity testing for geotechnical investigation of pusan clay deposits. *Journal of Applied Geophysics*, 52(4):157–175.

Ginzel, E. and Turnbull, B. (2016). Determining approximate acoustic properties of materials. *NDT. net Dec*.

Hashin, Z. and Shtrikman, S. (1962). A variational approach to the theory of the effective magnetic permeability of multiphase materials. *Journal of applied Physics*, 33(10):3125–3131.

Hashin, Z. and Shtrikman, S. (1963). A variational approach to the theory of the elastic behaviour of multiphase materials. *Journal of the Mechanics and Physics of Solids*, 11(2):127–140.

Hoekstra, P., Sellmann, P. V., and Delaney, A. (1975). Ground and airborne resistivity surveys of permafrost near fairbanks, alaska. *Geophysics*, 40(4):641–656.

Hoyer, W., Simmons, S., Spann, M., Watson, A., et al. (1975). Evaluation of permafrost with logs. In *SPWLA 16th Annual Logging Symposium*. Society of Petrophysicists and Well-Log Analysts.

Jackson, P., Smith, D. T., and Stanford, P. (1978). Resistivity-porosity-particle shape relationships for marine sands. *Geophysics*, 43(6):1250–1268.

Keller, G. (1971). Electrical characteristics of the earth's crust. In *Electromagnetic probing in geophysics*, volume 79, page 13.

King, M. (1984). The influence of clay-sized particles on seismic velocity for canadian arctic permafrost. *Canadian Journal of Earth Sciences*, 21(1):19–24.

King, M., Pandit, B., Hunter, J., and Gajtani, M. (1982). Some seismic, electrical, and thermal properties of sub-seabottom permafrost from the beaufort sea. In *Proceedings of the Fourth Canadian Permafrost Conference*, pages 268–273. National Research Council of Canada.

King, M., Zimmerman, R., and Corwin, R. (1988). Seismic and electrical properties of unconsolidated permafrost 1. *Geophysical Prospecting*, 36(4):349–364.

Kirkham, D., Taylor, G., et al. (1950). Some tests of a four-electrode probe for soil moisture measurement. *Proceedings. Soil Science Society of America, 1949*, 14:42–46.

Kolaian, J. H. and Low, P. F. (1963). Calorimetric determination of unfrozen water in montmorillonite pastes. *Soil Science*, 95(6):376–384.

Ladanyi, B. (1989). Effect of salinity and temperature on the behaviour of frozen soils. In *Preprint, Workshop on impact of saline permafrost, Winnipeg, Department of Civil Engineering, University of Alberta, Manitoba, Canada, Oct. 26*, volume 29.

Lee, M., Hutchinson, D., Collett, T., and Dillon, W. P. (1996). Seismic velocities for hydrate-bearing sediments using weighted equation. *Journal of Geophysical Research: Solid Earth*, 101(B9):20347–20358.

Lowrie, W. (2007). *Fundamentals of geophysics*. Cambridge university press.

Lyu, C., Amiri, S. A. G., Gao, H., Ingeman-Nielsen, T., and Grimstad, G. (2019). Joint acoustic and electrical measurements for unfrozen water saturation estimate - a review. In *Zenodo*. Zenodo.

Mavko, G., Mukerji, T., and Dvorkin, J. (2009). *The rock physics handbook: Tools for seismic analysis of porous media*. Cambridge university press.

McCorkle, W. (1931). Determination of soil moisture by the method of multiple electrodes. *Bulletin/Texas Agricultural Experiment Station; no. 426*.

Meheni, Y., Guérin, R., Benderitter, Y., and Tabbagh, A. (1996). Subsurface dc resistivity mapping: approximate 1-d interpretation. *Journal of Applied Geophysics*, 34(4):255–269.

Michel, B. (2006). *Fundamentals of acoustics*. Wiley.

Nakano, Y., Martin, R. J., and Smith, M. (1972). Ultrasonic velocities of the dilatational and shear waves in frozen soils. *Water Resources Research*, 8(4):1024–1030.

Nelson, P., Hansen, W., and Sweeney, M. (1982). Induced-polarization response of zeolitic conglomerate and carbonaceous siltstone. *Geophysics*, 47(1):71–88.

Palacky, G. (1987). Clay mapping using electromagnetic methods. *First Break*, 5(8):295–306.

Pandit, B. and King, M. (1979). A study of the effects of pore-water salinity on some physical properties of sedimentary rocks at permafrost temperatures. *Canadian Journal of Earth Sciences*, 16(8):1566–1580.

Polder, R., Andrade, C., Elsener, B., Vennesland, Ø., Gulikers, J., Weidert, R., and Raupach, M. (2000). Test methods for on site measurement of resistivity of concrete. *Materials and Structures*, 33(10):603–611.

Pounder, E. R. (2013). *The physics of ice*. Elsevier.

Pusch, R. (1979). Unfrozen water as a function of clay microstructure. *Engineering Geology*, 13(1-4):157–162.

Reynolds, J. M. (2011). *An introduction to applied and environmental geophysics*. John Wiley & Sons.

Rust, C. et al. (1952). Electrical resistivity measurements on reservoir rock samples by the two-electrode and four-electrode methods. *Journal of Petroleum Technology*, 4(09):217–224.

Thomas, H. R., Cleall, P. J., Li, Y., Harris, C., and Kern-Luetschg, M. (2009). Modelling of cryogenic processes in permafrost and seasonally frozen soils. *Geotechnique*, 59(3):173–184.

Tice, A., Anderson, M., and Sterrett, K. (1982). Unfrozen water contents of submarine permafrost by nuclear magnetic resonance. selected papers of the 2nd int. symp. on ground freezing.

Toksöz, M. N., Cheng, C. H., and Timur, A. (1976). Velocities of seismic waves in porous rocks. *Geophysics*, 41(4):621–645.

Tsytovich, N. (1960). *Bases and foundations on frozen soil*. National Academy of Sciences, National Research Council.

Vanhala, H. and Soininen, H. (1995). Laboratory technique for measurement of spectral induced polarization response of soil sampies. *Geophysical prospecting*, 43(5):655–676.

Vinegar, H. and Waxman, M. (1984). Induced polarization of shaly sands. *Geophysics*, 49(8):1267–1287.

Visacro, S. and Alipio, R. (2012). Frequency dependence of soil parameters: Experimental results, predicting formula and influence on the lightning response of grounding electrodes. *IEEE Transactions on Power Delivery*, 27(2):927–935.

Vogt, C., Laihem, K., and Wiebusch, C. (2008). Speed of sound in bubble-free ice. *The Journal of the Acoustical Society of America*, 124(6):3613–3618.

Wang, D.-y., Zhu, Y.-l., Ma, W., and Niu, Y.-h. (2006). Application of ultrasonic technology for physical–mechanical properties of frozen soils. *Cold regions science and technology*, 44(1):12–19.

Watanabe, K. and Mizoguchi, M. (2002). Amount of unfrozen water in frozen porous media saturated with solution. *Cold Regions Science and Technology*, 34(2):103–110.

Wenner, F. (1915). A method for measuring earth resistivity. *Journal of the Washington Academy of Sciences*, 5(16):561–563.

Wettlaufer, J. and Worster, M. G. (2006). Premelting dynamics. *Annu. Rev. Fluid Mech.*, 38:427–452.

Wiwattanachang, N. and Giao, P. (2011). Monitoring crack development in fiber concrete beam by using electrical resistivity imaging. *Journal of Applied Geophysics*, 75(2):294–304.

Zhou, M. and Meschke, G. (2013). A three-phase thermo-hydro-mechanical finite element model for freezing soils. *International journal for numerical and analytical methods in geomechanics*, 37(18):3173–3193.

Zhou, M., Wang, J., Cai, L., Fan, Y., and Zheng, Z. (2015). Laboratory investigations on factors affecting soil electrical resistivity and the measurement. *IEEE Transactions on Industry Applications*, 51(6):5358–5365.

Øyvind Blaker, Roselyn Carroll, P. P. D. J. D. and L'Heureux, J.-S. (2019). Halden research site: geotechnical characterization of a post glacial silt. *AIMS Geosciences*.